UNIVERSITY OF CALIFORNIA
RIVERSIDE

Health Monitoring of Drive Connected Three-Phase Induction Motors
------ From Wired Towards Wireless Sensor Networks

A Dissertation submitted in partial satisfaction
of the requirements for the degree of

Doctor of Philosophy

in

Mechanical Engineering

by

Xin Xue

August 2009

Dissertation Committee:

Dr. Sundararajan Venkatadriagaram, Chairperson
Dr. Thomas Stahovich
Dr. Javier Garay

The Dissertation of Xin Xue is approved:

_____

_____

_____

Committee Chairperson

University of California, Riverside

ACKNOWLEDGEMENTS

I would like to express my most sincere gratitude to Dr. Sundararajan Venkatadriagaram, advisor of this work, not only for his technical guidance in the realization of this dissertation, but also for his genuine care and supervision of all the academic and professional activities involved with the attainment of the doctoral degree.

Most sincere thanks also go to Dr. Thomas Stahovich and Dr. Javier Garay for their suggestions and guidance, for being my dissertation committee members and for their support in completion of this work. I am also grateful to Dr. Bir Bhanu and Dr. Akula Venkatram for their knowledge and experience in my interactions with them, especially for their suggestions and guidance on my research work.

I would like to acknowledge the Brithinee Electric Inc. located in Colton, California, for providing the financial support to this work. I would like to especially thank Dr. Wallace P. Brithinee, Dr. Donald Brithinee and Mr. William T. Butek, Mr. Gary Bryngelson for their support with equipments and expertise.

I would also like to thank all of my fellow graduate students in our department for their friendship and company throughout my study. I wish to

especially thank Luis Gonzales-Argueta, Rafael Garcilazo, Miaogeng Zhang for their help with the experiments.

Most of all, I wish to express not only the deepest gratitude to the unconditional support of my family, but a deep and immense love. Special expression of these feelings is extended to my dear husband Siyi Deng, father Jinqiang Xue, and mother Lindi Fu.

ABSTRACT OF THE DISSERTATION

Health Monitoring of Drive Connected Three-Phase Induction Motors
------ From Wired Towards Wireless Sensor Networks

by

Xin Xue

Doctor of Philosophy, Graduate Program in Mechanical Engineering
University of California, Riverside, August 2009
Dr. Sundararajan Venkatadriagaram, Chairperson

Wireless sensor network (WSN), one of the featured technologies that the U.S. Department of Energy (DOE) has identified to help improve the overall energy efficiency of US industry, provides a potentially low-cost approach for the health monitoring and fault diagnosis of induction motors. The reduction of machine failures increases plant efficiency and productivity. Low-cost wireless sensor systems can help the health monitoring of manufacturing equipments by eliminating the cost of installation and increasing the flexibility of system diagnosis.

This research focuses on developing a nonintrusive, condition based health monitory system for drive connected induction motors using the wireless sensor network method. A hierarchical classification system is designed for motor fault diagnosis. To simulate and analyze a wide range of fault conditions that may arise in induction motors, an experimental test bed is also developed. Three major branches of induction motor faults are studied, both individually and in combination. Wired sensors are first used to find optimal features for motor fault classification. After performing feasibility studies of wireless sensors in electric machinery, two wireless sensor nodes are developed and implemented in the motor health monitoring and fault diagnosis system. The experimental results demonstrate the effectiveness and generalizability of the wireless sensor system for motor health monitoring and fault classification.

TABLE OF CONTENTS

LIST OF FIGURES

LIST OF TABLES

CHAPTER 1

INTRODUCTION

This chapter presents the motivation and objective of this work in the first section. An outline of this dissertation is given in the second section. Then the necessary background information: condition monitoring, condition monitoring for motors, and sensor technology for induction machine monitoring are introduced.

1.1 MOTIVATION AND OBJECTIVE

With the increasing manufacturing expenses, reducing the operating cost and saving energy have become the urgent needs. The utilization and effectiveness of manufacturing equipments have gained increasing importance for industries with intensive capital investment and high operating costs. Across many industries, 15-40% of manufacturing costs are typically attributable to maintenance activities [1]. In the current competitive marketplace, maintenance management plays an increasingly important role in maintaining competitiveness. Effective maintenance management can reduce equipment

downtime and increase capital utilization, thereby allowing firms to minimize waste, reduce inventory and ensure timely delivery of products [2].

There are three widely accepted methodologies of maintenance 1) Reactive (unplanned or breakdown) maintenance 2) Preventive Maintenance 3) Condition-based maintenance. Breakdown maintenance is carried out after a machine has broken down or damaged. This strategy might be appropriate when failure rates are minimal and failure does not result in serious cost setbacks or safety consequence [3]. The conventional maintenance philosophy (called scheduled maintenance or preventive maintenance) is to stop the machine at pre-determined intervals. The EPRI M&DC [4] cites a Forbes magazine study that concluded that a third of the money spent on preventative maintenance in the utility industry was wasted. Tavner et al [5] states that only 10 percent of components replaced during fixed-interval maintenance outages actually need to be replaced at that time. The obvious implication is that 90 percent of what is replaced need not be. In order to reduce the cost of maintenance, to avoid the unplanned downtime and to improve the efficiency, condition-based maintenance (predictive maintenance) stops the machine only before there is evidence of impending failure. Although the return on investment depends on the specific industry and the equipment involved, Rao [6] states that an

investment in monitoring of between $10,000 and $20,000 dollars results in savings of 500,000 dollars a year. It has been clearly demonstrated that the use of appropriate condition monitoring and maintenance management techniques can give industries significant improvements in efficiency and directly enhance profitability.

Imagine a scenario, for example, where an induction motor has a bearing damaged by some foreign particles and the damage starts to grow gradually. Without a condition monitoring and fault detection system, this fault could cause the variation of the shaft alignment and further cause a serious air-gap eccentricity that may cause the rotor to rub against the stator leading to a catastrophic failure. An effective condition monitoring system will allow a schedule for motor maintenance before the damage becomes serious enough to cause major disruptions.

As one of the featured technologies in the 21st century that the U.S. Department of Energy (DOE) has identified to improve the overall energy efficiency of U.S. industry, wireless sensor network (WSN) technology provides a potential approach for a low-cost wireless motor monitoring system [7]. This becomes the motivation of this research. Low-cost wireless sensor systems can provide an efficient approach for health monitoring of manufacturing

equipments because they can eliminate the cost of installation while increasing flexibility. Wireless sensors can be installed in restricted and difficult to reach areas. With the data automatically collected and transmitted to the database, less field worker will be needed.

The objective of this work is to develop nonintrusive motor health monitoring systems for drive connected induction motors and to implement the monitoring system in a WSN architecture for industrial applications using only low-cost wireless sensors. Although this research concentrates on induction motors, the health monitoring system and fault diagnosis techniques described in this dissertation are also applicable to similar engineering systems.

1.2 Outline of Dissertation

A brief background to condition monitoring, condition monitoring for motors, and sensor technology for induction machine monitoring is given later in this chapter. And the contributions are listed at the end of this chapter. The motor construction, operation and failure modes will be introduced in chapter 2. All the major branches of motor failure are reviewed with emphasis on the fault characteristic frequency components in vibration, current or flux spectra.

To facilitate the development of wireless sensor systems, a wired monitoring system is designed for feature selection purposes. Chapter 3

introduces the signal processing procedures and feature selection based on the experimental results of wired sensor system using multiple wired sensors. It presents the experimental studies and algorithms to detect three types of faults both individually and in combination in three phase induction motors. Separate experiments are conducted for developing the algorithms (training and testing) and for validation.

In order to identify the reliability of wireless sensors for induction motor monitoring, chapter 4 addresses a feasibility study of wireless sensors in small and large induction motors. Experimental studies on the packet delivery performance and data fidelity of wireless sensors used inside a 1 hp AC motor as well as a 200hp AC motor are presented.

A wireless sensor monitoring system is then constructed based on the experimental results of the wired sensor system. Chapter 5 describes a low-cost wireless sensor network designed for motor health monitoring and fault classification. The wireless sensor nodes with an accelerometer sensor, a microphone, and a hall-effect sensor are developed and implemented in the wireless health monitoring system for induction motors. The same set of experiments is conducted for initial training and testing. The validation results

demonstrate the effectiveness and generalizability of the wireless system for motor health monitoring and fault classification.

Chapter 6 presents conclusions and possible future directions in developing wireless condition monitoring systems.

1.3 Background Review

1.3.1 Condition Monitoring and Relevant Multidisciplinary Areas

A brief taxonomy tree of maintenance philosophies can be found in Kothamasu's (2006) paper [3] as shown in Figure 1.

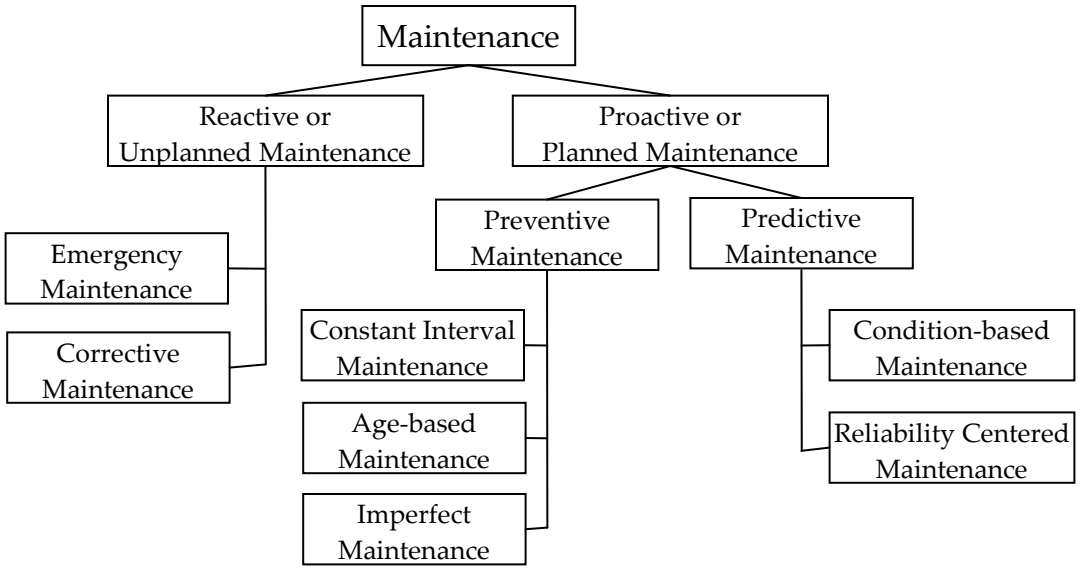

Fig. 1.1 Taxonomy of maintenance philosophies (Kothamasu et al 2006)

Condition monitoring (CM) or condition based maintenance (CBM) is the major component of proactive maintenance. As the name indicates, the condition of specific areas of plant and equipment are monitored. CM is the

process of monitoring operating and health parameters in machinery systems. Significant changes may be indicative of impending failures. Early detection allows actions to be taken to avoid the consequence of failure before the failure occurs. This can be done automatically with the use of instrumentation such as accelerometers and current probes. Condition monitoring is typically more cost effective than allowing the machinery to fail or performing scheduled maintenance [6].

Many case studies have proven that the investment of the condition monitoring system is invaluable. For example, at Iggesund Paperboard's plant in Workington, Cumbria, U.K., the company's No.2 board machine was reported to avoid an unscheduled downtime and production losses by SKF's bearing condition monitoring system which provided a timely forewarning that enabled a planned repair to be undertaken during a scheduled plant shutdown. Had the bearing failed completely, the resulting damage to the plant would have been catastrophic. It has been estimated that the machine may have had to be shut down for six months [8]. Another case study was presented in wind energy conference in Germany [9] about the gearbox condition monitoring system. GASTOPS's on-line oil debris monitoring system was reported to be able to detect the initial damage of one planetary stage bearing and one planetary stage

gear of a gearbox installed in a wind turbine in the United States nine months prior to removal and had given five months of reliable warning that the gearbox was damaged. The condition monitoring system provided ample lead-time to the operator to proactively deal with the gearbox repair, thus minimizing down time and avoiding secondary damage to the system. Similar results have been achieved by GE Wind as presented at the EWEA conferences in 2004 [10] and 2006 [11].

There are three relevant multidisciplinary areas mentioned in Worden's [12] review paper which also make the monitoring and assessing fault/damage the principal concerns: Structural Health Monitoring (SHM), Non-Destructive Evaluation (NDE) and Statistical Process Control (SPC). SHM is mainly relevant to structures such as aircrafts, buildings while SPC is process based rather than structure based. NDE is primarily used for characterization and as a severity check when there is *a priori* knowledge of the location of the damage. All of these areas including CM use sensors to provide signals. Modern systems of manufacturing in industries are highly coupled by both mechanical and electrical or electronic subsystems. The increasing complexity of the system brings more challenges to factory productivity and maintenance. Multiple sensors,

hierarchical strategy and hybrid methods have been used to some extent which also induced the research area of data fusion or data mining.

Data fusion uses data from multiple sources and gathers the desired information in order to achieve inferences. These inferences are generally more accurate than those achieved by means of a single source. Data mining is a technique of sorting through large amount of data and extract relevant useful information from enormous data sets generated from modern experimental measurements. It is also described as “the nontrivial extraction of implicit, previously unknown, and potentially useful information from data” [12] and "the science of extracting useful information from large data sets or databases" [13].

This work develops data-driven methods that use experimental measurements to build generalizable and extendable systems that can detect certain types of faults. Data-driven techniques rely on comparative assessments of the status of a system under testing with other known occurrences. As long as the behavior of the system under testing remains similar to that of a previously known, healthy configuration, the former is deemed to be healthy. When the measured behavior deviates from this reference, a fault is detected, and a comparison with the conditions previously observed in analogous faulted systems can take place. Under the appropriate conditions, this new comparison

has the potential to isolate and identify the fault efficiently. Thus, the ability of data-driven techniques to perform the task of diagnosis is obtained by training classification algorithms. Commonly used classifiers are introduced in chapter 3.

1.3.2 Condition Monitoring for Motors

Motor condition monitoring and diagnostics are important issues in motor-driven and power-electronics systems since they can greatly improve the reliability, availability and maintainability of the system. The common faults of induction motors include the stator winding faults, bearing defects, air-gap eccentricity and rotor faults. Chapter 2 will discuss these failure modes in detail. In industry, the losses associated with the unexpected downtime are usually much more than the cost of the motors themselves[14]. If these faults are predicted in a timely manner, the losses resulting from unexpected motor shutdowns and failures can be effectively avoided.

Currently, traditional quantities, such as line currents and voltages are measured and analyzed by very skilled technicians using expensive equipments for health monitoring of large induction motors[5]. As the ready availability of sophisticated electronic and microprocessor-based wireless systems is increasingly translated into monitoring hardware, the trend to make cost-effective investment of wireless monitoring equipments will be accelerated [15].

1.3.3 Sensor Technology for Induction Machine Monitoring

The development of a condition monitoring system involves the measurement of operating variables and parameters that provide sufficient details to detect impeding faults at an early stage. Temperature, vibration, force and torque, electrical and magnetic, as well as wear and debris sensors are commonly used for induction machines.

Temperature

Temperature is widely monitored in electrical drives and generators. It provides valuable monitoring information when the measurement is combined with information about the loading and ambient conditions of the machine [5]. Three types of temperature sensors are commonly used for measuring temperature electronically: (1) resistance temperature detection (RTD) (2) thermistors (3) thermocouples.

RTD sensors (also called the resistance thermometer) use the resistance change of a metal to indicate temperature change. They are used for insertion between winding conductors in machine slots and the measurement range can go up to 1000 °C. They have very good accuracy and precision but have a relatively low sensitivity [16]. Thermocouples are based on the well-known Seebeck effect - a current circulates in a closed loop formed of two dissimilar

metals joined in two places with a temperature difference between the junctions. Copper/constantan and chromel/alumel are most widely used junction materials for thermocouples used in coil temperature monitoring [5]. Depending on the quality of the signal conversion circuit, the performance of RTD temperature transduction can be very good but they are relatively expensive [16]. Thermisters are another type of temperature transducer manufactured from blends of metal oxides. They provide a coarse but very sensitive response. The measurement range is generally limited to 300 °C.

Other techniques such as quartz thermometers, fibre-optic temperature sensing and infrared thermography are generally more expensive and have not been widely used in condition monitoring of induction machines.

Vibrations

Vibration sensors take the measurement of three quantities that are related by numerical integration or differentiation: displacement, velocity, and acceleration. Displacement transducers are most effective for measurements at the lower frequencies. As the vibration frequency increases it is likely that displacement levels will fall but acceleration levels will rise. Velocity measurement has the frequency response range in between the measurement of displacement and acceleration.

For displacement measurement, capacitive and inductive devices such as linear variable differential transformers (LVDT) are commonly used. For motor condition monitoring, non-contacting displacement probes or proximeters are of most interest to achieve the measurements of shaft eccentricity and differential movements due to expansion [17].

For velocity measurement, the most widely used transducer is an electromagnetic velocity probe. It consists of a coil of wire and a magnet so arranged that if the housing is moved, the magnet tends to remain stationary due to its inertia. The relative motion between the magnetic field and the coil induces a current that is proportional to the velocity of motion. The device thus produces a signal directly proportional to vibration velocity. It requires little or no signal conditioning but is relatively heavy and complex and thus expensive [18].

Nowadays, velocity and displacement are commonly measured using accelerometers. The required parameters are derived by integration. Accelerometers are rigidly fastened to the body undergoing acceleration. The piezoelectric accelerometer has become almost universally accepted as the transducer to use for vibration measurements[5]. It is physically more robust than the velocity transducer and has a far superior frequency range [18].

Acoustic sensors can also be categorized as vibration sensing devices. Wei et al. [19] provides a general review of bearing condition monitoring via acoustic emission. Li and Mechefske [20] compared the stator current, vibration and acoustic methods for detection of faults in induction motors. Their experimental results indicate that the acoustic sensor has the potential to show both the current and vibration frequency components related to the motor faults.

Force and Torque

Strain gauges are the most commonly used devices for force measurement. The resistance change of the device reflects the stress change under the action of the force. Such a device can be used to measure torques applied to shafts. For rotating shafts, alternative contact-free torque transducers also exist such as magneto-eleastic or fibre-optic torque sensors. The use of specific techniques for particular applications can be found in literatures [21, 22].

Electrical and Magnetic Measurement

The basic electrical quantities associated with induction machines are current and voltage. They are usually obtained from current transformers and voltage transformers.

To measure the magnetic flux density in or around electrical machines, a simple search coil or a hall-effect device can be used. The search coil is a device

that passively generates electrical current when being placed in an alternating magnetic field. It, however, cannot detect DC fields. In addition, it has the risk of sparking [16].

Hall-effect devices provide a measurement of flux density over a very small area. Figure 1.2 shows the basic principle of the operation of hall-effect element. When a current I is passed through a thin sheet of semiconducting material, the present magnetic field with strength B causes the disturbance of the current due to Lorentz force, resulting in a potential difference (voltage V_{out}) across the output.

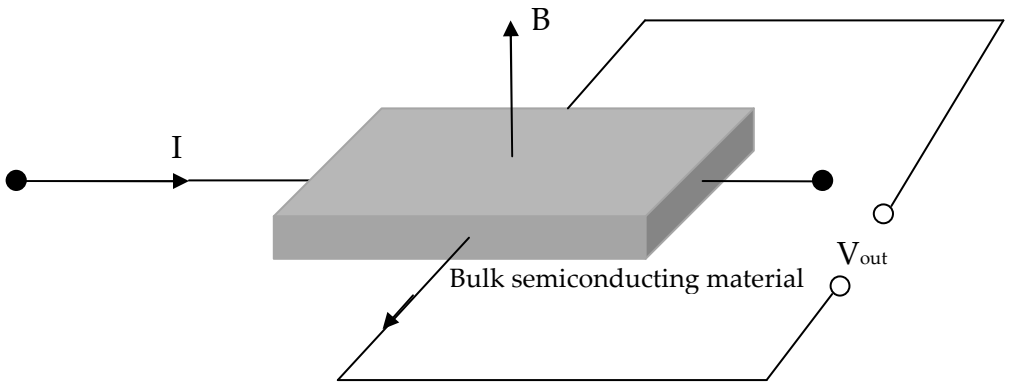

Fig. 1.2 Principle of hall effect

Hall-effect devices have the advantage of being able to measure down to DC, and can be made in extremely small sizes [23]. The current and voltage measurement can also be obtained by hall-effect transducers.

Wear and Debris Measurement

In many induction machines, the condition of lubricant and coolant may provide crucial information of the machines. For example, when the bearing wears, we would naturally expect to detect debris in the lubricant [24]. The most common method of debris measurement is to use a so-called debris sensitive detector. There are two types of detectors: optical and electrical detectors. The principle of the operation can be found in literature [16]. These two types of detectors are often used in combination in condition-monitoring applications [5].

1.4 Contributions

This work describes a complete methodology for the application of WSN technology in condition monitoring and fault classification for drive connected three-phase induction motors. The contributions of this methodology can be further divided into the following areas:

1) Based on the fault characteristic frequencies discovered in previous research, a new method to extract features using Hilbert-Huang Transform has been developed.

2) Feasibility studies of wireless sensors in a small induction motor and a large induction motor have been conducted. The packet delivery performance and data fidelity have been evaluated by experimental methods.

3) A general approach for motor health monitoring and fault classification in wireless sensor network architecture has been proposed based on the experimental results of a wired sensor system. A two stage hierarchical classification process has been design for the motor fault classification.

4) Following the approach, two wireless sensor nodes are developed for motor monitoring applications. Three major branches of motor faults are simulated in a test bench. Experiments of thirteen conditions and three different loads have been conducted for the initial training and testing of the classifiers. Three two-fault conditions have been investigated using the combination of two single faults simulated simultaneously. Validation tests are designed to demonstrate the effectiveness of the wireless motor monitoring and fault classification system.

CHAPTER 2

MOTOR CONSTRUCTION, OPERATION AND FAILURE MODES

This chapter introduces the basic construction of an induction motor and the principle of its operation. Previous studies of different motor failures and their diagnosis are briefly reviewed in the second section. All the faults related frequency components in current, vibration and sound waveform are presented. These fault characteristic frequencies are used as features for fault detection and classification.

2.1 Motor Construction and Operation

The basic construction of an induction motor is shown in Figure 2.1. The rotor is normally supported by two bearings, one at each end. The outer races of the bearings are mounted in the enclosure of the motor. The stator is the fixed outer portion and the rotor spins inside separated from the stator by a carefully engineered air-gap. Coils of insulated wires are inserted into the slots of stator core. Each group of coils, together with the core it surrounds, forms an electromagnet (a pair of poles). The drive end of the rotor shaft extends outside the enclosure of the motor and can be connected to various loads. The non-drive

end of the rotor shaft is usually connected to a fan for the cooling system shown in Figure 2.1. Some motors may have an accessory shaft on the non-driving end for mounting speed or position sensing devices. Through the air gap between the stator and the rotor, the energy is transferred from the stator to the rotor due to the induction.

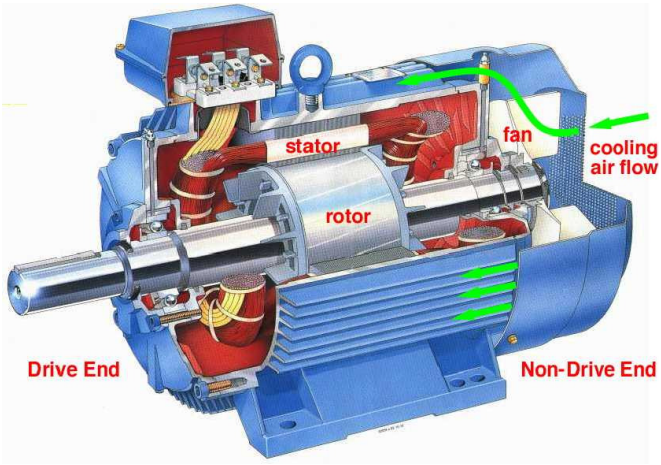

Fig. 2.1 Structure of a 4 kW induction motor showing stator core and windings, stator frame, rotor, and bearings. [Source: GE Power Systems, USA]

The magnetic field created in the stator rotates at a synchronous speed ω_s calculated by [25]:

$$\omega_s = 120 \times \frac{f_s}{P} \quad (2.1)$$

where f_s is the supply frequency in Hertz, and P is the number of poles on the stator. The unit of ω_s is revolution per minute (rpm).

When the motor is standing still and the magnetic field produced in the rotor rotates at the synchronous speed, the high relative speed induces a large back electromotive force (e.m.f.) in the rotor. The e.m.f. sets up currents in the rotor that create a rotor magnetic field that opposes the stator field. The interaction of the two fields works to reduce the relative speed of the rotor with respect to the stator. The rotor, thus, starts running in the same direction as that of the stator flux and tries to catch up with the rotating flux. However, in practice, the rotor never succeeds in "catching up" to the stator field but runs slower than the speed of the stator field. This speed is called rotor mechanical speed ω_r. The difference between ω_s and ω_r formulates the definition of slip [25]:

$$s = \frac{\omega_s - \omega_r}{\omega_s} \quad (2.2)$$

where *s* is the slip which varies with the load.

2.2 Failure Modes of Induction Motors

There are four major branches of failure modes for induction motors[26]. Figure 2.2 shows the fishbone diagram that chained the causes to the resulting effects. As shown in the diagram, final motor failure is caused by 1) rotor bar broken or cracked end ring, 2) stator winding open circuits or short circuits, 3) air-gap eccentricity and 4) bearing failure. Rotor failure is caused by thermal

overload, shaft torque, centrifugal forces and contamination. The stator failure is caused by insulation failure of the winding; the air gap eccentricity is caused by static eccentricity or dynamic eccentricity; the bearing failure is caused by fatigue, contamination, improper lubrication or improper installation. Further causes can be chained as the figure.

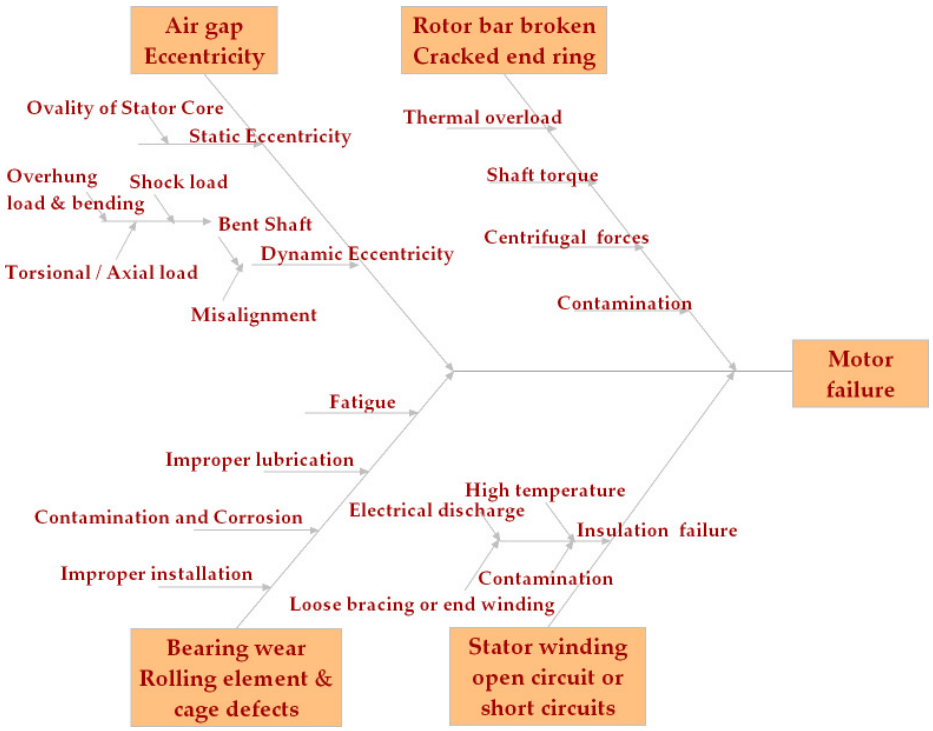

Fig. 2.2 Induction motor faults fishbone diagram. Reproduced from Xue et al (2008)

2.2.1 Rotor Bar Broken and End Ring Faults

Rotor failures account for 5-10% of total induction motor failures [27, 28]. The most common rotor is a squirrel-cage rotor. It is made up of bars of either solid copper (most common) or aluminum that span the length of the rotor, and

are connected through a ring at each end [5]. There are two types of cage rotors: cast rotors and fabricated rotors, according to their fabrication process. Fabricated rotors are generally found in larger or special application machines while cast rotors are only used in smaller machines [29]. Cast rotors are usually more rugged than the fabricated type. However, they can almost never be repaired once faults like broken rotor bars develop in them [30].

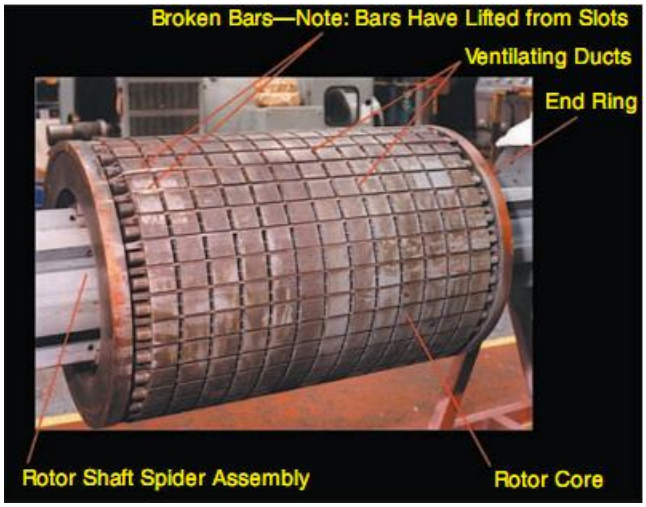

Fig. 2.3 Example of broken rotor bar faults. Source: reference [31]

Figure 2.3 gives an example of broken bar faults from literature [31]. Broken rotor bars have been paid much attention among the variety of probable faults in induction motors because the rotor itself is usually quite expensive. In motor theory, it is well known that broken rotor bar faults give rise to a sequence of sideband components of the supply frequency and its harmonics. Kliman [28],

Thomson [32], Fillippetti [33], and Elkasabgy [34] used machine line current spectrum analysis (MCSA) to detect the broken bar faults. They investigated the sideband components around the fundamental supply frequency at

$$f_{brk} = (1 \pm 2s)f_s$$

Where $f_{brk}$is the fault characteristic frequency (sideband components), f_s is the supply frequency, and s is the slip. Fillippetti [33] shows that broken bars actually give rise to a sequence of such sidebands which can be formulated as.

$$f_{brk} = (1 \pm 2ks)f_s, \qquad k = 1,2,3 \ldots \quad (2.3)$$

The left (lower) sideband is specifically due to broken bars, and the right (upper) sideband is due to consequent speed oscillation [35].

According to Faiz et al. [36], even in the tested healthy induction motor, the amplitude of the sideband components are large, and broken rotor bars can slightly increase the sideband components. Therefore, further research on other fault indicator is necessary.

2.2.2 Stator Winding Faults

The major cause of stator faults is insulation failure. Almost 30-40% of all reported faults of induction motor failures fall under this category [27, 37]. The insulation is exposed to high temperatures, high voltages, vibrations and other mechanical forces, as well as some adverse environmental conditions. These

stresses can act together or individually to degrade insulation materials or systems [5]. A very thorough review of root causes of failures and failure modes in insulation systems and conducting components is given in Stone et al. [38]. A clear evidence of shorted winding burns [31] is shown in Figure 2.4.

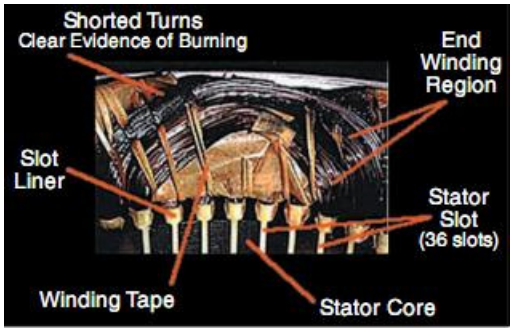

Fig. 2.4 Stator winding faults. Source: reference [31]

There has been a range of papers published on the analysis of air-gap and axial flux signals to detect shorted turns and the detailed mathematics can be found in the references [39, 40]. Air-gap flux monitoring is not attractive to the operators since it is highly invasive to existing motors in service. Any interference from the sensor itself may cause serious damage to the motor. There is also a leakage flux signal (axial along the shaft outside the motor's frame) that will normally contain the components indicating the turn to turn faults. Even the fault position could be detected by mounting four coils symmetrically in the four quadrants of the motor at a radius of about half the distance from the shaft to the

stator end winding [40]. The frequency components to detect winding faults in the flux waveform is given by

$$f_{st} = \left\{\frac{n}{p}(1-s) \pm k\right\} f_s \quad (2.4)$$

Where f_{st} represents the components that are a function of shorted turns, $n = 1, 2, 3 \ldots$, $k = 1, 3, 5, \ldots$, p is the number of pole pairs. Thomson [41] has reported the diagnosis of shorted turns via MCSA based on the same frequency components given by equation 2.4. These components also appear in current waveform because the rotating flux waves can induce corresponding current components in the stator winding.

2.2.3 Air-gap Eccentricity Related Faults

Air-gap eccentricity is the condition that the air-gap between the stator and the rotor becomes uneven. When eccentricity becomes large enough, the resulting unbalanced radial force (also called unbalanced magnetic pull) can cause stator and rotor to contact. This will result in the damage of the stator and rotor.

Figure 2.5 shows a typical air-gap eccentricity drawing from literature [42]. The eccentricity is called static air-gap eccentricity if the minimum air-gap length is fixed during the rotor rotation. The common cause is ovality of the stator core.

In the case of dynamic air-gap eccentricity, the minimum air-gap rotates with the rotor. It is caused by misalignment or bent shaft as chained in Figure 2.2.

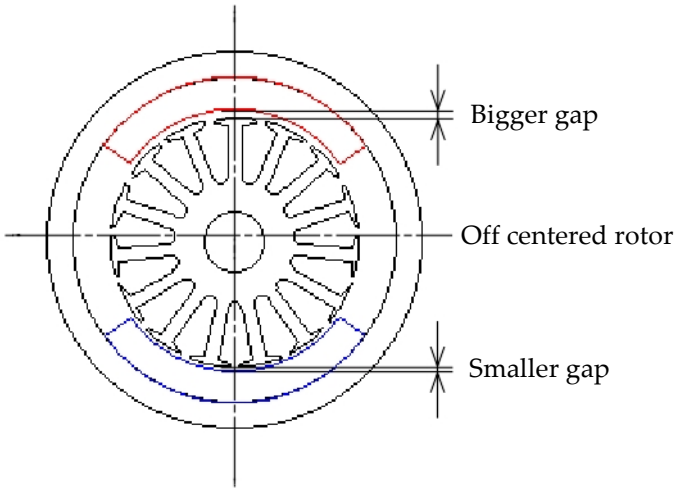

Fig. 2.5 Illustration of air-gap eccentricity. Source: reference [42]

The high-frequency components of interest are formulated by [43]

$$f_{ecc} = \left\{\frac{1-s}{p}(kR \pm n_d) \pm v\right\} f_s \quad (2.5)$$

Where f_{ecc} is the components that are a function of air-gap eccentricity, R is the number of rotor bars, p is the number of pole pairs, $n_d = 0$ when it is static eccentricity and $n_d = 1, 2, 3$ in case of dynamic eccentricity (n_d is known as eccentricity order); k is any integer, $v = 1,3,5 \ldots$ (v is known as the stator time harmonics that are present in the power supply driving the motor) [44]. Low-frequency components near the fundamental given by [29]

$$f_{ecc} = f_s \pm k f_r \quad (2.6)$$

are also related to air-gap eccentricity faults.

Theoretical modeling to find frequency components of air-gap eccentricity related faults in line current have been described in references [44, 45]. Principal slot harmonic (PSH) is defined by equation 2.5 with $k = 1, v = 1, n_d = 0$. Nandi introduced a nominal 38.46% static eccentricity by machining the bearing housing of the machine end bells. The experimental results suggest that a pragmatic approach to detect the eccentricity faults requires examination of both high-frequency and low-frequency components in equation 2.5 and 2.6. Toliyat [46] used a disc drilled with four small holes on one side of it which is loaded on the motor to emulate the case of rotor dynamic eccentricity. The results show that the 17^{th} and 19^{th} harmonic of current spectrum increases rapidly due to the dynamic air-gap eccentricity.

2.2.4 Bearing Faults

Bearing faults are of practical importance since approximately half of the motor faults accounts for bearing faults [47]. Fatigue failures can take place even under normal operating conditions with balanced load and good alignment. These faults may lead to increased vibration and noise levels [48]. Other than the normal internal operating stresses, bearings can be affected by external interference such as contamination, improper lubrication and improper

installation as chained in Figure 2.2. An example showing inner race defect of ball bearing [49] is given in Figure 2.6.

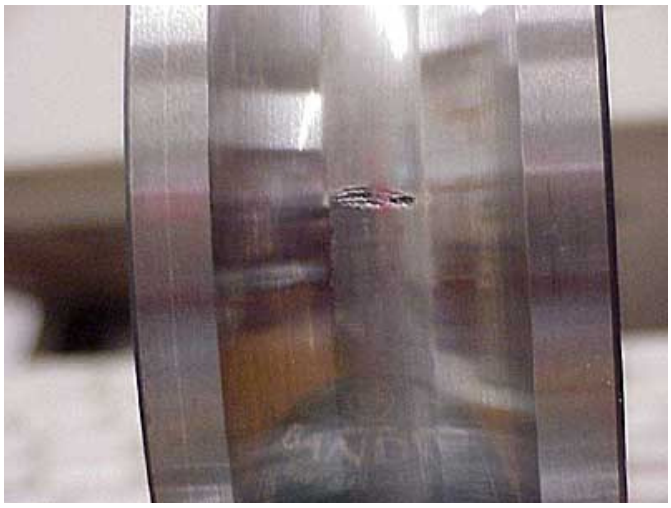

Fig. 2.6 Example of ball bearing inner race defect. Source: reference [49]

Wei [19] has given a general review on different bearing condition monitoring methods including vibration monitoring, temperature monitoring, chemical analysis, acoustic emission monitoring, sound pressure monitoring, laser monitoring and current monitoring. The most popular method is analyzing vibration spectrum [50-52]. Although current monitoring is non-invasive and may easily be implemented in the motor control center, the bearing-fault signatures are subtle in the stator current since the dominant components are supply frequency components [19].

For a rolling element bearing, the bearing outer/inner race fault characteristic frequencies are [29]:

$$f_o = \frac{n}{2}\left(1 - \frac{d}{D}\cos\beta\right) f_r \quad (2.7)$$

$$f_i = \frac{n}{2}\left(1 + \frac{d}{D}cos\beta\right) f_r \quad (2.8)$$

where n is the number of balls, d is the ball diameter, D is the pitch diameter, β is the contact angle, and f_r is the rotation speed of the rotor. The ball spin frequency is

$$f_{bs} = \frac{D}{d}\left\{1 - \left(\frac{d}{D}cos\beta\right)^2\right\} f_r \quad (2.9)$$

A ball defect will give rise to two times of the ball spin frequency. If a current sensor is used on the supply line or an audio sensor is used to collect the sound signals from the motor, the corresponding current and sound spectra show the fault characteristic frequency [29, 53]

$$f_{brg} = f_s \pm f_{bcf} \quad (3.0)$$

where f_s is the power supply frequency, f_{bcf} .is the bearing characteristic frequencies described above.

2.3 Summary

Although some important frequency components are discovered for detecting the motor faults, these faults are usually studied individually. Most of the motor faults data used in literature are simulated data. Experimental data for induction motor faults have to be thoroughly analyzed.

This work studies three major categories of the motor faults both individually and in combination: 1) stator winding faults, 2) air-gap eccentricity faults and 3) bearing faults. Due to the limited resources for experiments, rotor faults are not studied, but the system can easily be extended to include this type of faults by adding a category in the hierarchical classification tree.

Vibration, current, sound data are easy to collect. There are plenty of potential features to be used for faults classification. The feature selection of induction motor faults based on results of the wired sensor system is described in the following chapter.

CHAPTER 3

FEATURE SELECTION BASED ON RESULTS OF WIRED SENSOR SYSTEM

This chapter introduces the signal processing techniques and pattern classification methods used in this research. Experimental studies are reported for detecting three types of faults both individually and in combination in three phase induction motors. The faults studied are 1) eccentricity of the air-gap between the rotor and the stator, 2) damage to the inner/outer race of bearings, and 3) unbalanced resistance of the stator windings. The experiments are conducted under thirteen conditions: a normal no-fault control condition; three bearing fault conditions: bearing with a scratched inner race, bearing with a scratched outer race and bearing without grease; three air-gap eccentricity conditions: one-side tilted air-gap eccentricity, parallel type air-gap eccentricity, two-side reversed air-gap eccentricity; three unbalanced resistance conditions: phase A with additional resistance, phase B with additional resistance and phase C with additional resistance; three multi-fault conditions: inner race scratched bearing with unbalanced stator winding resistance, outer race scratched bearing with air-gap eccentricity, and unbalanced stator winding resistance with air-gap

eccentricity. Two microphones, one vibration sensor and one current sensor are used to collect sound, vibration and current data respectively. The data is analyzed using the Fast Fourier Transform (FFT), Hilbert-Huang transform (HHT), and the Discrete Wavelet Transform (DWT) described in the first section. Based on the classification results of each sensor, features extracted from the HHT and FFT are selected to classify all the motor faults in a hierarchical way.

3.1 Signal Processing

The technique most frequently used to detect frequencies is the Fast Fourier Transform (FFT). However, this method has a number of deficiencies when directly used over a faulty motor's vibration signature [54]. The FFT alone is not capable of analyzing the frequency content of a defective bearing signal because such a signal is amplitude-modulated and non-stationary i.e. the characteristics of the signal such as the mean change with time. The wavelet transform is one of the most suitable time-frequency approaches [55, 56]. It however has the disadvantage of a fixed scale frequency resolution [57]. It depends on a single fixed type of mother wavelet chosen arbitrarily. Hilbert-Huang transform (HHT), on the other hand, provides multi-resolution at various frequency scales and takes into consideration - the signal's frequency content and its variation [54, 58]. The implementation of the HHT for bearing fault diagnosis

has been reported by Hui and Haiqi [59] and Rai and Mohanty [57]. Hui and Haiqi analyzed the first intrinsic mode function (IMF) of vibration signal and used the spectrum of its envelope to detect the fault defect frequencies. Rai and Mohanty compared the original vibration spectrum of vibration signal and the FFT of the decomposed signals for an outer race fault bearing and an inner race fault bearing. All the characteristic defect frequencies are captured in multiple intrinsic mode functions (IMFs); by contrast some of the characteristic defect frequencies are missing in the original vibration spectrum. Their results suggest that the FFT can be ineffective in the analysis of non-stationary vibration signal from defective bearings and demonstrate that the HHT with FFT of IMFs is an advanced signal processing technique which is necessary for bearing fault diagnosis.

3.1.1 Fast Fourier Transform (FFT)

FFT is an efficient method to compute the Discrete Fourier Transform (DFT). Let $x_0, \ldots x_{N-1}$ be the time series. The DFT is defined by the formula

$$X_k = \sum_{n=0}^{N-1} x_n e^{-i2\pi k \frac{n}{N}}, \qquad k = 0, \cdots, N-1$$

For this study, the frequency axis is divided into bins that correspond to frequency zones of interest. The magnitudes of the FFT coefficients in the bins are used as features.

3.1.2 Hilbert-Huang Transform (HHT)

Hilbert-Huang Transform is a method to analyze nonstationary and nonlinear time series data in time-frequency-energy representation [60]. HHT is computed in two steps –- 1) empirical mode decomposition (EMD) and 2) Hilbert spectral analysis. The HHT uses the EMD to decompose a signal into intrinsic mode functions (IMFs), and then uses the Hilbert transform of the IMFs to obtain instantaneous frequency data.

3.1.2.1 Definition of Intrinsic Mode Functions (IMFs)

Huang et al [60, 61] have defined Intrinsic Mode Functions (IMFs) as a class of functions that satisfy two conditions:

(1) In the whole data set, the number of extrema and the number of zero-crossings must be either equal or differ at most by one. (In other words, every adjacent local maxima and minima of the wave must across the zero line.)

(2) At any point, the mean value of the envelope defined by the local maxima and the envelope defined by the local minima is zero. (In other words, the

upper envelope and the lower envelope estimated from the local maxima and local minima are approximately symmetric with regard to the zero line.)

The next section explains the process, called empirical mode decomposition (EMD) to obtain IMFs.

3.1.2.2 Empirical Mode Decomposition (EMD)

To extract IMFs from the signal $x(t)$, a sifting process comprising the following steps is used:

1) Find the positions and amplitudes of local maxima, and local minima of $x(t)$. Then construct an upper envelope by interpolation (typically a cubic spline interpolation) of the local maxima, and a lower envelope by a similar interpolation of the local minima. Calculate the mean $m_1(t)$ of the upper and lower envelopes. Subtracting the envelope mean signal from the original input signal, we have

$$h_1(t) = x(t) - m_1(t) \quad (3.1)$$

Check whether $h_1(t)$ meets the requirements to be an IMF as defined in the section above. If not, treat $h_1(t)$ as new data and repeat the previous process. Then set

$$h_{11}(t) = h_1(t) - m_{11}(t) \quad (3.2)$$

Repeat this sifting procedure k times until $h_{1k}(t)$ is an IMF as defined in the previous section; this is designated as the first IMF.

$$c_1(t) = h_{1k}(t) \quad (3.3)$$

2) Subtract $c_1(t)$ from the input signal and define the remainder, $r_1(t)$, as the first residue. Since the residue, $r_1(t)$, still contains information related to longer period components, it is taken as a new data stream. Repeat the above-described sifting process to find more IMFs until the following stopping criteria are met. The sifting process is stopped when either of the following criteria are met: 1) the component $c_n(t)$, or the residue $r_n(t)$, becomes so small in magnitude as to be considered inconsequential, or 2) the residue, $r_n(t)$, becomes a monotonic function from which an IMF cannot be extracted. Finally, the signal can be represented as the sum of IMFs and a residue.

$$x(t) = \sum_{j=1}^{n} c_j(t) + r_n(t) \quad (3.4)$$

An example of EMD is shown in Figure 3.1. The original signal (Figure 3.1 (a)) is simulated by adding a chirp signal to a pure tone. The decomposed IMFs and the residue are shown in Figure 3.1 (b). The first IMF represents the signal in a higher frequency band which is very similar to the chirp signal. The second

IMF perfectly matches the pure tone. All the other IMFs are lower bands signals which can be ignored.

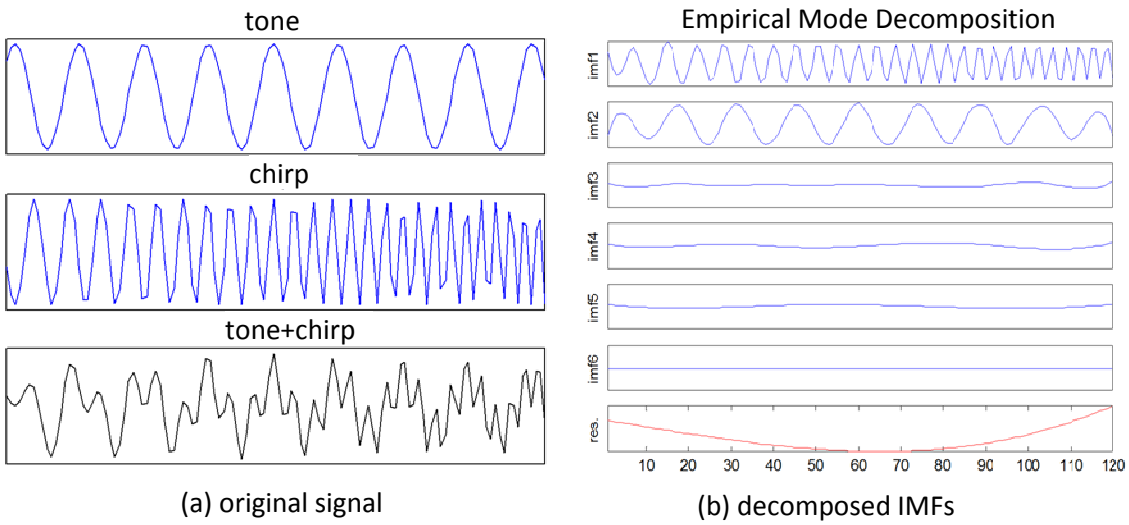

Fig. 3.1 Example of EMD (a) original signal (b) decomposed IMFs

3.1.2.3 Envelope of IMFs and Instantaneous Frequency

Apply the Hilbert transform [62] to all the IMFs, $c_j(t)$, we have

$$H[c_j(t)] = \frac{1}{\pi}\int_{-\infty}^{+\infty}\frac{c_j(t)}{t-\tau}d\tau \quad (3.5)$$

A complex signal is formed using the IMF and its Hilbert transform as

$$z_j(t) = c_j(t) + i\,H[c_j(t)]$$

Expressing $z_j(t)$ in complex exponential form

$$z_j(t) = a_j(t)e^{i\theta_j(t)} \quad (3.6)$$

where the amplitude of the envelope,

$$a_j(t) = \sqrt{c_j(t)^2 + H[c_j(t)]^2} \quad (3.7)$$

and the phase angle

$$\theta_j(t) = \arctan\left(\frac{H\left[c_j(t)\right]}{c_j(t)}\right) \quad (3.8)$$

Then the instantaneous frequency is

$$\omega_j(t) = \frac{d\theta_j(t)}{dt} \quad (3.9)$$

Thus the original signal can be expressed as

$$x(t) = \sum_{j=1}^{n} a_j(t) e^{i \int \omega_j(t) dt}$$

where the residue has been left out, and the expression represents a generalized Fourier expansion. The average amplitude of the envelope, mean of $a_j(t)$, for certain IMFs will be used as the HHT features. This average amplitude of the envelope is the representation of the energy level of the IMF.

3.1.3 Discrete Wavelet Transform (DWT)

Wavelets provide time-scale information of a signal, enabling the information extraction of the signal. The continuous wavelet transform (CWT) of $x(t)$ is a time-scale method of signal processing that is defined by:

$$CWT(a,b) = \frac{1}{\sqrt{|a|}} \int_{-\infty}^{+\infty} x(t) \Psi^* \left(\frac{t-b}{a}\right) dt$$

where $\Psi(t)$ denotes the mother wavelet. The parameter a represents the scale index which is a reciprocal of frequency. The parameter b indicates the time shifting (or translation). The discrete wavelet transform (DWT) is derived from the discretization of CWT (a, b) and the most common discretization is dyadic, given by

$$DWT(l,m) = \frac{1}{\sqrt{2^l}} \int_{-\infty}^{+\infty} x(t)\Psi^*\left(\frac{t-2^l m}{2^l}\right) dt$$

where a and b are replaced by 2^l and $2^l m$. An efficient way to implement this scheme is using high pass and low pass filters developed by Mallat [63]. The original signal, $x(t)$, passes through two complementary filters and emerges as low frequency [approximations (A's)] and high frequency [details (D's)] signals. The decomposition process can be iterated, with successive approximations being decomposed in turn, so that a signal can be broken down into many lower-resolution components.

In this study, the vibration signal is decomposed to the first level approximation A1 and detail D1. The current and sound signals are all decomposed to the fifth level approximation A5 and detail D5. Higher level detail signals D3 and D4 are also used since their bandwidths also carry frequencies of interest.

3.2 Pattern Classification Methods

There are a number of pattern classification methods available for fault detection and classification. Three widely used classifiers are implemented in this study.

3.2.1 Naïve Bayesian Classifier (NB)

A Naïve Bayesian Classifier is a simple probabilistic classifier based on applying Bayesian theorem with strong (naïve) independence assumptions. It assumes that the presence of a particular feature of a class is unrelated to the presence of any other feature.

Let f be a feature vector of size $n \times 1$, C is the class that belongs to m classes. Given the feature vector f and the likelihood $P(f_i|C)$, the most probable class of a sample is decided by [64]

$$P(C|f) = argmax_c\, P(C) \prod_{i=1}^{n} P(f_i|C)$$

3.2.2 K-Nearest Neighbor Rule (KNN)

The nearest neighbor rule classifier is trying to find the nearest neighbor of an unknown pattern by calculate the distance from the unknown class pattern to all the training patterns. Then classify this pattern to the class that its nearest neighbor is. The k-nearest neighbor rule is an obvious extension of the nearest

neighbor rule. A decision is made by examining the labels on the k nearest neighbors and taking a vote. To calculate the distance in d dimensions, we can use Euclidean formula as follows

$$D(\boldsymbol{a}, \boldsymbol{b}) = \left(\sum_{i=1}^{d} (a_i - b_i)^2 \right)^{\frac{1}{2}}$$

The computational complexity of the nearest neighbor rule depends on the number of training samples and the feature dimension. It is a good choice to use a nearest neighbor classifier if the feature dimension is not too large [65]. Other metrics also exist such as Manhattan or city block distance (L1 norm), Cosine (one minus the cosine of the included angle between two vectors).

3.2.3 Artificial Neural-Network Classifier (ANN)

An artificial neural network (ANN) is a mathematical model that tries to simulate the structure and functional aspects of biological neural networks. It consists of an interconnected group of artificial neurons and processes information using a connectionist approach to computation. In most cases an ANN is an adaptive system that changes its structure based on external or internal information that flows through the network during the learning or training phase. It can be used to model complex relationships between inputs and outputs or to find patterns in data.

In the training stage, given a set of example pairs (f, c) , ($f \in F$ $feature\ domain$, $c \in C$ $class\ domain$), the aim is to find a function $g: F \rightarrow C$ that maps the input features to the output class in a mean squared error sense. Back propagation algorithm is the most well-known training algorithm for ANN classifiers. The detail of the algorithm can be find in literature [65, 66]. In this study, the back propagation ANN classifier with one hidden layer and ten neurons are used.

3.3 Feature Selection and Results of Wired Sensor System

3.3.1 Materials

Motor

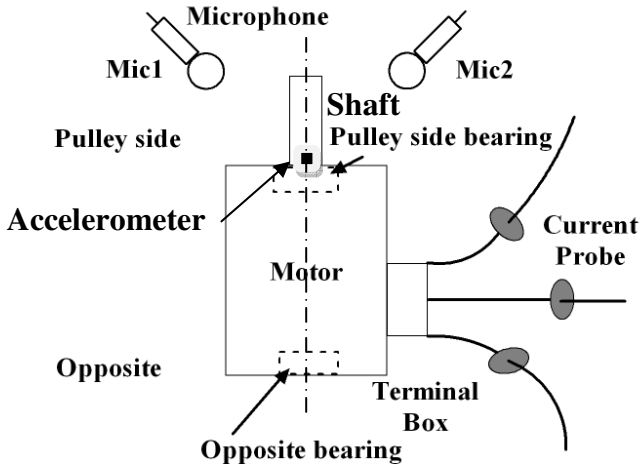

Fig. 3.2 Diagram of experiment setup

The experiment setup is shown in Figure 3.2. The motor used here is a 1.5hp 6-pole three phase induction motor rated at 230V line voltage and 4.8A line current. It is connected to an adjustable speed drive to control the speed. The running speed of the motor with no load is 1200rpm which corresponds to 20 revolutions per second (20 Hz).

Sensors

Current, vibration and sound signals are collected by a current probe, an accelerometer and two microphones respectively. The current probe is an ac current transformer which gives output of 1mA/A AC. The current signal is collected by the data acquisition board using Labview software. The sampling rate for the current probe is set at 8.192 kHz. The accelerometer is commercially available from Crossbow Tech, Inc. The output is a voltage and the sensitivity is 0.506V/g, where g, the earth's gravitational acceleration, is approximately 9.8 m/s^2. The sampling rate of the accelerometer using the company's hardware and software is 160 Hz. The microphones are connected to the audio analog input on the computer. Sound recording software is used to collect the data. The sampling rate is set to 44.1 kHz. The resulting signal is then down sampled to 8192 Hz.

Conditions

This paper studies the current, vibration and sound signal collected from a 1.5 hp 3-phase induction motor with five categories of conditions (Figure 3.3) : 1) two-fault condition; 2) unbalanced stator winding resistance; 3) air-gap eccentricity; 4) damaged bearings; 5) normal condition. Except the normal condition, each category contains three sub-classes. The various categories are shown in Figure 3.3. The single faults can interact with each other which challenges the detection of two-fault conditions. The two-fault conditions studied are a) damaged bearing with unbalanced stator winding resistance; b) damaged bearing with air-gap eccentricity; c) unbalanced stator winding resistance with air-gap eccentricity. Category 2), 3) and 4) are single fault conditions. Three phases of stator winding with bigger resistance (approximately 8% larger than the original resistance) are studied as sub-classes. Any two-fault condition which involves unbalanced stator winding resistance fault uses an additional resistor for stator phase A winding. The three sub-conditions of air-gap eccentricity are a) one-side tilted type; b) two-side parallel type; c) two-side reversed type. The damaged bearing conditions are inner race scratched, outer race scratched and no grease condition. These will be described in detail.

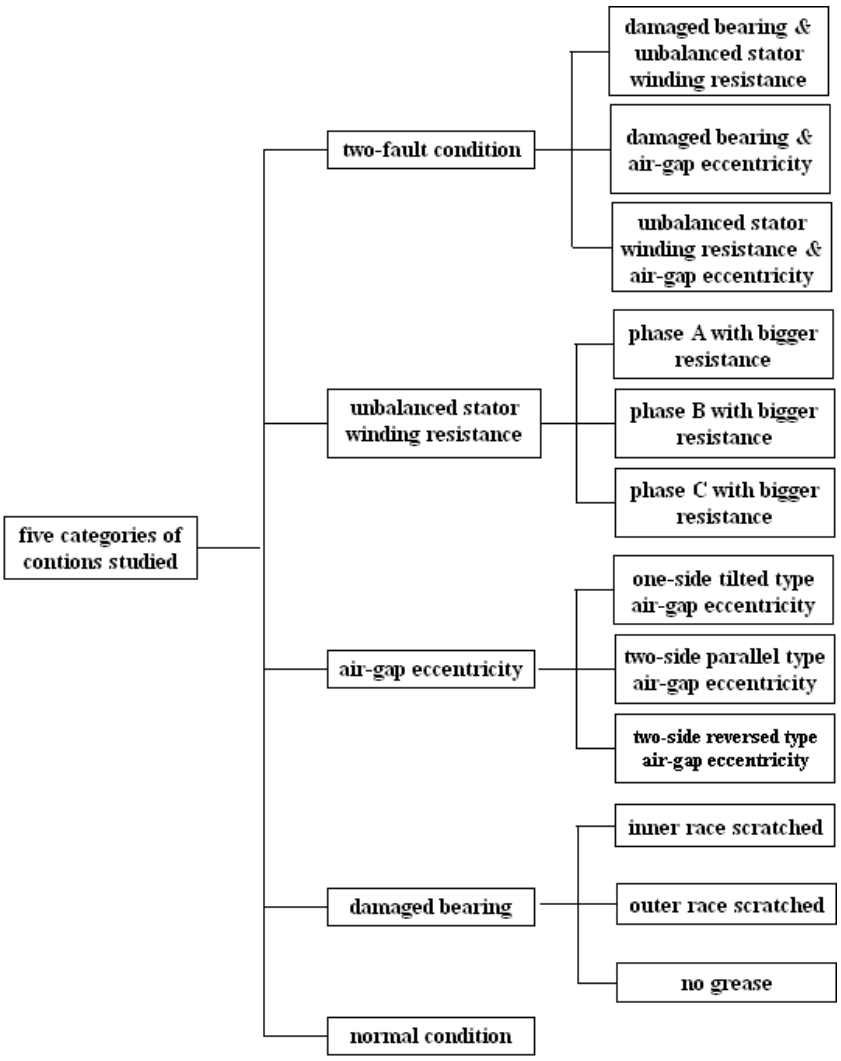

Fig.3.3 Diagram of induction motor conditions; totally 13 conditions grouped as five categories.

The effects of air-gap eccentricity are studied by replacing the bearings in the motor housing by a smaller outside diameter bearing located in an off-centered bushing (Figure 3.4). The circled mark indicates the thickest point of the bushing. The offset causes a deviation of the rotor center line as shown in Figure 3.4. Three types of air-gap eccentricity are studied. The first one called the one-side tilted air-gap eccentricity replaces only the pulley side bearing

(Figure 3.5(a)). The offset causes an uneven air-gap length between the rotor and the stator core thus resulting in eccentricity of the air-gap fault. The side view shows the air gap changing linearly between the rotor and stator core along the shaft axis. The second one called the two-side parallel type replaces both the pulley side bearing and the opposite bearing (Figure 3.5(b)). The center line of the rotor is parallel with the ideal original center line. Both the marked sides (circled in Figure 3.4) of the bushings are placed on bottom. The third one called the two-side reversed type also replaces both the pulley side bearing and the opposite bearing (Figure 3.5(c)). The difference is to put the marked sides (circled in Figure 3.4) on opposite sides of the center line. This causes the center line of the rotor to intersect with the original center line only at the mid-point. In Figure 3.4, L1 is the minimum air gap which is approximately 0.2 mm, and L2 is the maximum air gap which is approximately 0.6 mm. All the two-fault conditions use the one-side tilted type air-gap eccentricity (Figure 3.4 (a)) which installs the pulley side bearing with its marked side on bottom.

Opposite bearing Pulley side bearing

Fig. 3.4 Original bearings and their replacement; the mark indicates the thickest part of the bushing.

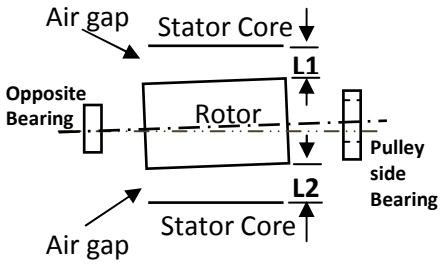

(a) one-side tilted type

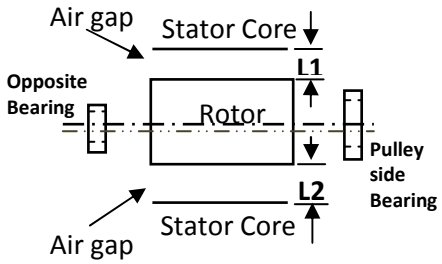

(b) two-side parallel type

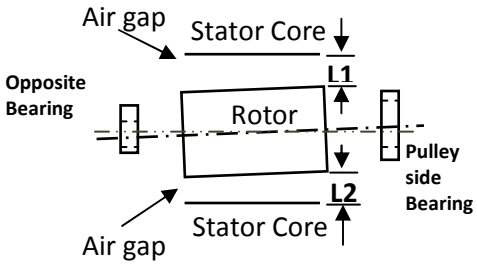

(c) two-side reversed type

Fig.3.5 Static air-gap eccentricity (a) one-side tilted type (b) two-side parallel type (c) two-side reversed type

Bearing faults are studied by replacing the opposite bearing of the motor with an open bearing. The open bearing allows access to the race way of a bearing. This bearing is scratched using a diamond mounted tool on the surface of inner/outer race way. The other bearing fault is studied by running the bearing without grease. This will cause damage to both inner and outer race way after some time of running. The two-fault condition of damaged bearing and unbalanced stator winding resistance uses an inner race damaged bearing. The two-fault condition of damaged bearing and air-gap eccentricity uses an outer race damaged bearing.

3.3.2 Experimental Design

Experiments are conducted under thirteen different conditions which are grouped as five categories: only bearing fault condition, only air-gap eccentricity condition, only unbalanced stator resistance condition, two faults simultaneously and a normal control condition. For each condition, the motor is set up three times randomly switched from one condition to another. The data are collected in 1 minute time spans and cut to 4 seconds for the vibration signal and 2 seconds for the current and sound signals. The sensor data sets are summarized in Table 1. The sound data are collected at a sampling rate of 44.1 kHz and downsampled to 8192 Hz. The current data is passed through a low pass filter with the cut-off frequency of 1500Hz in order to get rid of the high order harmonics generated by the adjustable speed drive due to pulse width modulation [67]. Current and microphone data frame are set for 2 second durations whereas the accelerometer data is gathered for 4 second durations. For each sensor, 120 sets of data are obtained for each condition except for the normal condition. In order to fit in the 5-category classifier, 360 sets of data are obtained for normal condition. Thus each category has equal number of data sets. For validation purposes, additional experiments are conducted under two conditions randomly selected from these thirteen conditions.

Table 3.1 Data sets summary (wired sensor)

Sensor type	Sampling rate (Hz)	Frame length (second)	No. of frames
accelerometer	160	4	120
Current probe	8192	2	120
Microphone 1	8192	2	120
Microphone 2	8192	2	120

3.3.3 Analysis

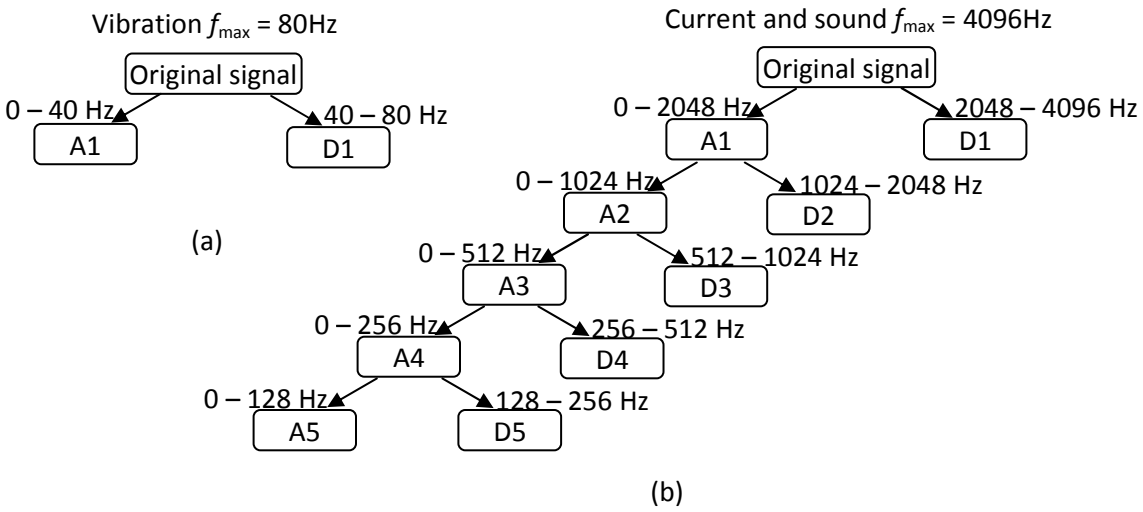

Fig.3.6 Frequency bandwidth of wavelet decomposition (a) vibration signal decomposition (b) current and sound signal decomposition

The Intrinsic Mode Functions (IMFs) are extracted using the procedure outlined in Section 3.1.2. Since the sampling rate of the accelerometer is lower, there are fewer features from the vibration sensors. Only two IMFs are used in vibration data, seven IMFs are used in sound, and eight IMFs are used in current

data analysis. The frequency components selected from each IMF are based on the fault characteristic frequencies mentioned in chapter 2.

Table 3.2 Features list

Vibration data		
HHT features	FFT	DWT
f_r (IMF2) $2f_r$ (IMF1) $3f_r$ (IMF1) f_{bs} (IMF1) f_o (IMF1) IMF1 average envelope **Total: 6**	f_r $2f_r$ $3f_r$ f_{bs} f_o **Total:** **5**	f_r (A1) $2f_r$ (A1) $3f_r$ (D1) f_{bs} (A1) f_o (D1) **Total:** **5**

Current data			Sound data		
HHT features	FFT	DWT	HHT features	FFT	DWT
f_s+f_i (IMF1) PSH (IMF2) $40f_r$ (IMF2) f_s+7f_r (IMF3) f_s+6f_r (IMF3) f_s+6f_r (IMF4) f_s+3f_r (IMF4) f_s-f_i (IMF4) f_s+f_o (IMF4) f_s (IMF5) f_s+3f_r (IMF5) f_s-f_o (IMF8) IMF2 average envelope **Total: 13**	PSH f_1 f_s+3f_r f_s+6f_r f_s+7f_r f_s+f_i f_s-f_i f_s+f_o f_s-f_o **Total:** **9**	PSH (D3) f_s (A5) f_s+3f_r (A5) f_s+6f_r (D5) f_s+7f_r (D5) f_s+f_i (D5) f_s-f_i (A5) f_s+f_o (D5) f_s-f_o (A5) **Total:** **9**	PSH (IMF1) f_s+14f_r (IMF1) f_s+13f_r (IMF2) f_s+12f_r (IMF2) f_s+10f_r (IMF2) f_s+2f_r (IMF3) f_s+3f_r (IMF3) f_s+4f_r (IMF3) f_s+5f_r (IMF3) f_s+6f_r (IMF3) f_s+7f_r (IMF3) f_s+5f_r (IMF4) f_s+f_o (IMF4) f_s+f_i (IMF4) f_s (IMF5) f_s-f_i (IMF5) f_i (IMF5) f_o (IMF5) f_r (IMF6) f_s-f_o (IMF7) IMF4 average envelope **Total: 21**	PSH f_s+14f_r f_s+13f_r f_s+12f_r f_s+10f_r f_s+2f_r f_s+3f_r f_s+4f_r f_s+5f_r f_s+6f_r f_s+7f_r f_s+f_o f_s-f_o f_s+f_i f_s-f_i f_s f_i f_o f_r **Total:** **19**	PSH (D3) f_s+14f_r (D4) f_s+13f_r (D4) f_s+12f_r (D4) f_s+10f_r (D4) f_s+2f_r (A5) f_s+3f_r (A5) f_s+4f_r (D5) f_s+5f_r (D5) f_s+6f_r (D5) f_s+7f_r (D5) f_s+f_o (D5) f_s-f_o (A5) f_s+f_i (D5) f_s-f_i (A5) f_s (A5) f_i (A5) f_o (A5) f_r (A5) **Total:** **19**

The frequency bandwidths of approximations and details of wavelet decompositions are shown in Figure 3.6. According to the fault related

frequencies, the final approximation and several detail signals are used. The mother wavelet used here is Daubechies 4 (db4) [56, 68]. Daubechies wavelet is the most commonly used set of wavelet [68].

The HHT features, FFT features and DWT features selected for different sensors are listed in Table 3.2. The features are all selected based on the discovered frequency components that indicate certain faults mentioned in chapter 2. The features are then used as input to various two stage classifiers as shown in Figure 3.7. Half of the data sets are randomly picked from the data sets of each condition as training data. The training data sets are used twice, one for the 5-category classifier, and again for one of the subclass classifiers. The performance is evaluated based on 10 cross validation tests. The details are discussed in the next section.

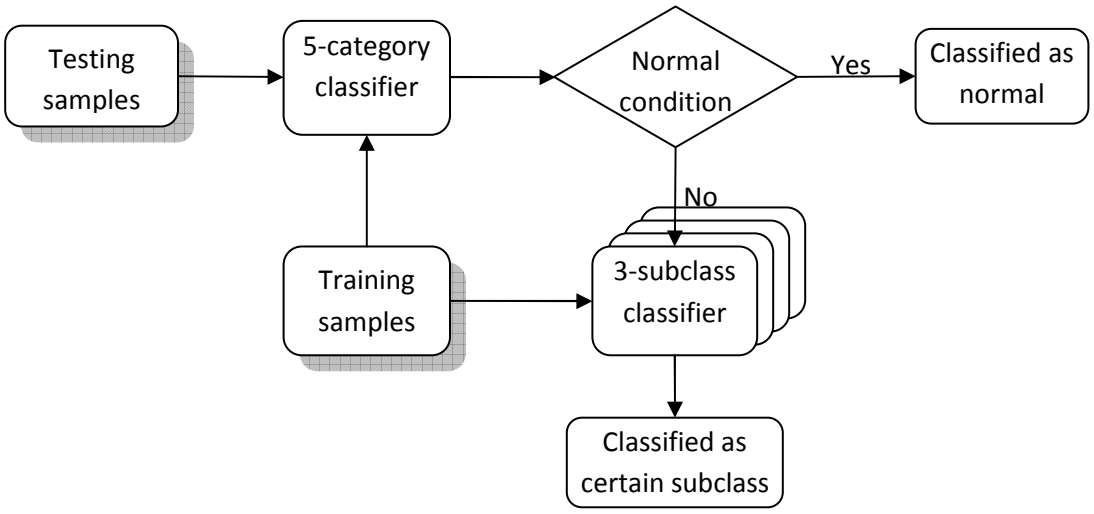

Fig. 3.6 Two-stage classifier processing structure

3.3.4 Results

The Principal Slot Harmonic (PSH) can be calculated from equation 2.5. Since the rotor of the induction motor in this set of experiments has 46 bars, the PSH frequency is approximately 978.4 Hz. The opposite bearing is SKF bearing of series 6206, a deep grove ball bearing. There are 9 balls in the bearing. The contact angle is 0°. The ball diameter is 9.525mm and the pitch diameter is 46mm. The inner/outer race fault characteristic frequencies are 108.63Hz (equation 2.7) and 71.36 Hz (equation 2.8) respectively. The ball spin frequency is 46.22 Hz (equation 2.9). These features are used in various classifiers. The results are shown below.

Figure 3.8 shows the IMFs and their corresponding spectrum of a typical vibration signal for normal condition and a two-fault condition: bearing outer race with scratch and air-gap eccentricity. It is obvious the EMD process works like an adaptive filter that decomposes the signal into a set of IMFs with different frequency bands. The current and sound signals are decomposed similarly. The normal condition in Figure 3.8 (a) captures the ball spin frequency of 46.25 Hz in its first IMF C(1)'s spectrum and the rotating frequency 20 Hz in its second IMF C(2)'s spectrum. The two-fault condition in Figure 3.8 (b) captures the outer race fault characteristic frequency 71.5 Hz which is absent in normal condition C(1)'s

spectrum. There is an obvious difference between the magnitude of the third harmonic of rotating frequency 60 Hz in both spectrums of C(1). This contrast also exists between the magnitude of average envelope (equation 3.7) in both of the first IMF C(1).

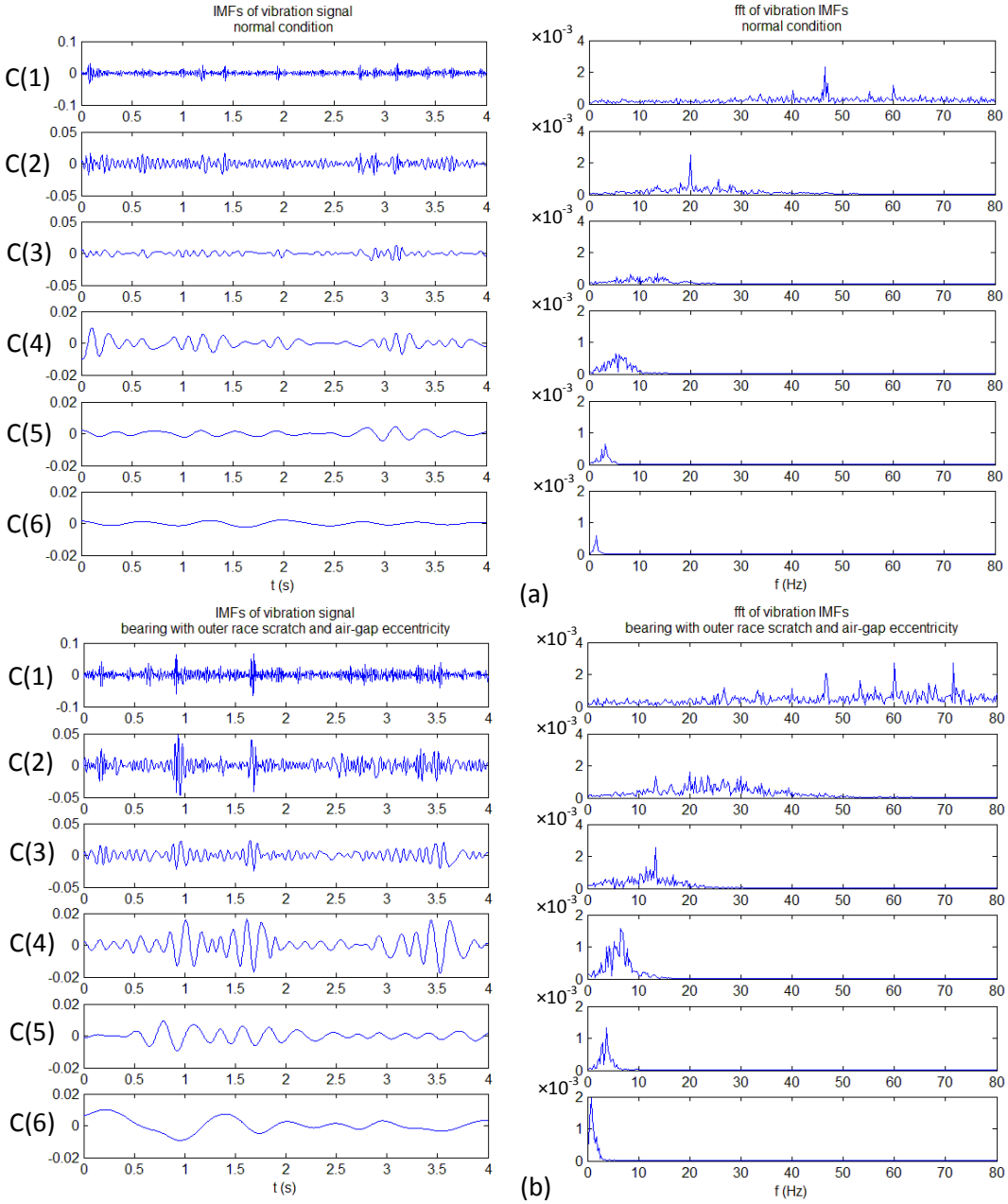

Fig.3.8 IMFs of vibration signal and the corresponding spectrum (a) normal condition (b) two-fault condition: bearing outer race with scratch and air-gap eccentricity

The features described in Table 3.2 are used as input to simple classifiers. The three classifiers used are Naïve Bayesian (NB) classifier, k-Nearest Neighbor

(KNN) classifier and feed-forward back propagation Artificial Neural Network (ANN) described in previous section. For 5-category classification, 180 trials of each category are randomly selected as training data, and the remaining 180 trials are used as testing data. For 3-subclass classification, 60 trials of each class are used as training data, and the remaining 60 trials are used as testing data. FFT features, IMF features and DWT features are all extracted and used as input to these classifiers respectively. The comparison is carried out in all 5-category classification tests.

3.3.4.1 Results of First Stage: 5-category Classification

Table 3.3 lists the 5-category classifier results using only one of these sensors in the experiment. The microphone sensor itself can achieve 88.6% correct classification rate. Vibration sensor can only achieve 72.7% correct classification rate. This could be caused by the low sampling rate of vibration sensor and fewer features. The current sensor shows better performance than the vibration sensor in all three classifiers. Two microphones give similar classification rate results, but it should be considered that the experiments were conducted in a quiet lab environment. In industry applications, the microphone sensor performance will be reduced. The validation test in a noisy environment is described in section 3.3.4.3. From this table of results, none of the sensors

individually can achieve a performance that is higher than 90% correct classification rate in the lab environment.

Because of the low classification accuracy, multiple sensors are necessary. From the vibration sensor results, the performance using HHT features is much better than using FFT and DWT features. Given the large number of trials (180 trials for each category) in the testing process, the difference (about 10%) is unlikely due to the chance error. From the current and microphone sensor results, the performance using HHT features is slightly worse than using FFT features. The performance using DWT features doesn't show any advantage. In order to achieve higher performance by using multiple sensor features, the HHT features from the vibration sensor and FFT features from current and microphone sensors are used in the feature level sensor fusion.

Table 3.3. Correct classification rate of the testing data using one sensor

Classifier \ Sensor		Accelero-meter	Current probe	Micro-phone 1	Micro-phone 2
NB (%)	HHT	60.7	59.5	72.9	68.5
	FFT	52.1	62.0	76.3	73.9
	DWT	48.9	57.2	69.1	68.7
KNN (%)	HHT	**72.7**	68.5	81.7	87.1
	FFT	**57.6**	**73.5**	**86.6**	88.5
	DWT	51.5	58.3	**73.7**	71.9
ANN (%)	HHT	70.5	**71.1**	**85.2**	**87.5**
	FFT	55.3	71.8	87.2	**88.6**
	DWT	**53.8**	**62.0**	73.5	**73.5**

Table 3.4 Classification results using two sensors

Sensors*	Correct Classification Rate (%)		
	NB	KNN	ANN
ACC + CP	76.9	89.2	90.3
ACC +Mic1	84.5	88.9	90.7
ACC+ Mic2	85.3	90.2	93.5
CP + Mic1	83.7	90.8	92.6
CP + Mic2	81.9	92.7	94.3
Mic1 + Mic2	83.7	91.7	96.3

***ACC: accelerometer; CP: Current Probe; Mic: Microphone**

Table 3.4 shows the results tested using features from two sensors. The features from different sensors are simply accumulated in a feature vector (this is called feature level sensor fusion). The performance is greatly improved by using two sensor features. All the classification performance exceeds 90%. Although all the performances that involve microphone 2 are superior in Table 3.4 and the highest performance of single sensor in Table 3.3 is microphone 2, it does not mean that the performance is related to the position of the microphone tested here. To test the hypothesis that the position of the microphone 2 is responsible for its superior performance, the two microphones were interchanged so that microphone 1 now occupied the position of microphone 2 and vice versa. The results showed that it was the specific microphone hardware that contributed to its better performance, and not its location. Table 3.4 shows the results of best combination of two sensor features which the combination of

two microphone sensors. The performance can be increased to 96.3% correct classification rate using ANN classifier. The other two classifiers also have high classification performance.

Table 3.5 lists the classification results using all combinations of three sensors' features and all sensors' features. The performance of all combinations are higher than most of two sensor results. Almost all the classification performances exceed 95%. Among the combinations of three sensors' features, Microphone 2, vibration and current sensor give the highest performance. With all sensors used, the performance can achieve 97.9% correct classification rate using ANN classifier and all the classifiers give the performance above 95% correct classification rate. The higher performance of the first stage result, the higher the final classification rate of the system. Therefore, we should use all the sensors' features for the first stage classification.

Table 3.5 Classification results using three or more sensors

Sensors	Correct Classification Rate (%)		
	NB	KNN	ANN
ACC + CP + Mic1	88.7	94	94.6
ACC+CP+Mic2	91.9	96.8	**97.1**
ACC+Mic1+Mic2	88.5	92.3	96.0
CP+Mic1+Mic2	87.6	94.3	96.4
ACC+CP+Mic1+Mic2	95.7	97.0	**97.9**

3.3.4.2 Results of Second Stage: Subclass Classification

In the 2nd stage classification, every category contains 3 subclasses except the normal condition. All the classification results above are an average of 10 cross validation tests since the training data sets are randomly selected from each condition of the training and testing data sets. Based on one simulation test results of the 1st stage classification using ANN classifier (Figure 3.9), all the correctly classified trials are used for the 2nd stage classification test. The final performance is simply the multiplication of these two stages' correct classification rate.

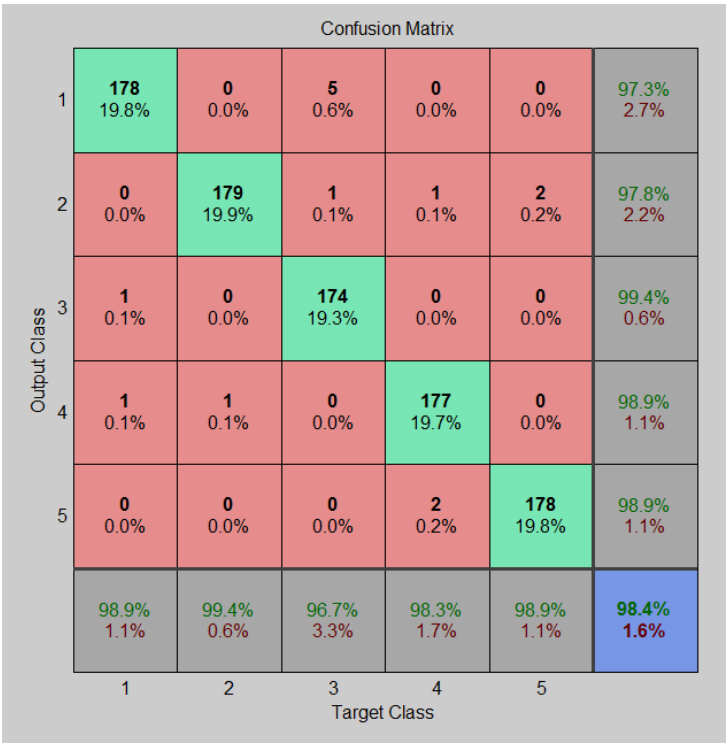

Fig. 3.9 Confusion matrix of ANN for 5-category classification using all sensors' features

Figure 3.9 shows the confusion matrix of the 1st stage 5-category classification results. A confusion matrix contains information about targeted and predicted classifications done by a classification system. In this case, each class has 180 testing trials. Class 1 to 5 represents two-fault condition, unbalanced stator winding resistance, air-gap eccentricity, damaged bearings and normal condition respectively. To read it vertically, for instance, there are 178 trials are correctly classified as class 1, one trial of class 1 is wrongly classified as class 3 and one trial of class 1 is wrongly classified as class 4. To read it horizontally, 5 trials of class 3 are wrongly classified as class 1. The last row shows the correct classification rate of each category in the 1st stage. The total of 900 testing trials in the 1st stage classification has the final performance of 98.4% correct classification rate.

In the 2nd stage, all the training trials are used again in the subclass classifiers. Only the correct classified testing trials are evaluated in the subclass classifiers because there is no chance of correct classification at the second stage when the first stage classification is incorrect. Table 3.6 lists the results of the test finished for both 1st stage and 2nd stage classification. All the features from different sensors are used in the 2nd stage subclass classifiers. For simplicity the classifiers chose here are NB classifiers. Almost all the 2nd stage classification

performance of this test has 100% correct classification rate. The final performance is about the same as the 1st stage performance.

Table 3.6. Final performance of all conditions

	two-fault condition			unbalanced stator winding resistance			air-gap eccentricity			damaged bearing			normal
1st stage CRC	98.9			99.4			96.7			98.3			98.9
2nd stage CRC	98.3	98.3	100	100	100	100	100	100	100	100	100	100	
final perfor-mance	97.2	97.2	98.9	99.4	99.4	99.4	96.7	96.7	96.7	98.3	98.3	98.3	98.9

*CRC: Correct Classification Rate

3.3.4.3 Validation Tests

In order to verify the system reliability, four validation tests are conducted in: (1) quiet lab environment; (2) noisy fan and DC motor running; (3) loud music playing environment; (4) noisy fan, DC motor running and loud music playing environment. Two conditions, which were not used for training, are randomly chosen from the various possible conditions and four sets of data are collected for each condition to validate the classification system. The experiments conducted for validation are (1) unbalanced resistance in phase C, (2) inner race scratched bearing and one-side tilted type air-gap eccentricity.

In the experiments for training and testing above, the resistance of phase C winding is 8% larger than the original resistance but in validation test

condition (1) the resistance of phase C winding is 5% larger than the original resistance; an outer race damaged bearing is used for two-fault condition of damaged bearing and air-gap eccentricity but in validation test condition (2) an inner race damaged bearing is used as the damaged bearing. The data are collected for 2 minutes using the same sensors and data acquisition method for each set. All the data are used as testing samples, no training involved. 30 frames are gathered to perform the testing using the classifier trained above.

The validation test results are shown in table 3.7 and 3.8. The first stage classifier is ANN classifier and the second stage is still NB classifier. Table 3.7 lists the testing results in lab quiet environment. Only 1 trial is failed to be correctly classified in the first stage for the unbalanced stator winding condition and 3 trials are failed to be classified in the first stage for the two-fault condition of damaged bearing and air-gap eccentricity. The total performance is 96.7% and 90.0% correct classification rate respectively. Table 3.8 lists the testing results in noisy environments. The performance of the first stage classification is reduced by more than 10%. The second stage classification of unbalanced resistance condition is perfect probably because the significant features are not the sound features. The final performances of all validation tests are above 70% correct classification rate.

Table 3.7 Validation test performance (quiet environment)

condition	First stage classification	Second stage classification	Total performance
Phase C with additional resistance	96.7% (29/30)	100% (29/29)	96.7%
Damaged bearing and air-gap eccentricity	90.0% (27/30)	100% (29/29)	90.0%

Table 3.8 Validation test performance (noisy environment)

Condition	Phase C with additional resistance			Inner race scratched bearing and air-gap eccentricity		
Environment	Fan and DC motor noise	Music	Fan, DC motor and music	Fan and DC motor noise	Music	Fan, DC motor and music
First stage classification	83.3%(25/30)	80.0%(24/30)	86.7%(26/30)	83.3%(26/30)	90.0%(27/30)	80.0%(24/30)
Second stage classification	100%(25/25)	100%(24/24)	100%(26/26)	96.2%(25/26)	96.4%(27/28)	95.8%(22/24)
Final testing performance	83.3%	80.0%	86.7%	80.1%	86.8%	73.4%

3.4 Summary

This chapter described the feature selection process based on the classification results of various motor faults using wired sensors. The experiments are conducted under no-fault, single fault and multiple faults condition. The results demonstrate the effectiveness of using intrinsic mode functions in Hilbert-Huang transform to construct vibration sensor features for classification. However, no single sensor was able to achieve a high enough classification accuracy. Multiple sensors were required to enable reliable classification.

Due to the large number of classes, a two stage classification system is designed to solve the problem. Both HHT features of vibration sensor and FFT features of current and microphone sensors are selected as final features for classification. The first stage contains five categories and the second stage contains 3 subclasses for each faulty category. High classification accuracy is achieved by using multiple sensors and both HHT and FFT features. Two validation conditions using separate experiment data prove the effectiveness of the system even in a noisy environment. These features thus will be used in the study of fault diagnosis using wireless sensors.

CHAPTER 4

FEASIBILITY OF WIRELESS SENSORS FOR HEALTH MONITORING

This chapter investigates the characteristics and performance of wireless sensors for application in both small and large induction motors. The parameters that are studied are: 1. The fidelity of the data acquisition as determined by comparison with wired sensors; 2. The reliability of the communications as a function of distance, spatial position and battery life of the sensor. This reliability is measured as the percentage of successfully delivered data packets. The experiments employ vibration sensors placed inside the motor enclosure on the stator and on the motor shaft. Each sensor is interfaced to a wireless node that possesses communication and computational capability. The transmitted data is collected by a base station located outside the motor.

4.1 The Need for Feasibility Study

Electric motors are used in a wide range of industrial applications and consume a significant portion of energy of the industrial sector [14, 69]. Their inefficiencies and failure cause substantial losses in the form of increased energy costs and maintenance costs. Online condition monitoring can improve the

reliability, availability and maintainability of electric motors by providing early warning of impending failures [69].

At present, most of the sensors are physically wired. The wires provide both power and communications paths. However, in many applications, wired sensors are impractical or inconvenient. For example, they are difficult to mount on rotating machinery or high temperature applications. In these situations, wireless sensor networks provide a possible solution. These networks can be used in remote locations and also offer inexpensive and flexible installation.

In contrast to conventional condition monitoring of electrical machinery that measure current or vibration signals outside the motor, wireless sensors provide access to useful signals inside the motor where the phenomena responsible for failure occur. These sensors are capable of not only sensing, but also of processing, storage and eventually communication. This chapter studies the feasibility of wireless sensor nodes inside the motors using current technology and evaluates the data acquisition and transmission performance of these nodes.

Wireless sensors bring up several issues that need careful study and experimentation. The quality of wireless communication depends on the environment, the part of the frequency spectrum under use, the particular

modulation schemes under use, and possibly the communicating devices themselves [70]. Wireless receptions change with slight spatial displacements and also may vary over time. Multi-path interference cause signal nulling, signal amplitude increasing or decreasing, and data corruption. Many of the current sensor platforms use low-power radios which do not have enough frequency diversity to reject multi-path cancellation. In addition, when signals are sending from the transmitter inside the motor, the motor enclosure may block the signal but the extent is unknown. Although the induction motors are designed to have minimum field leakage, there are still some fringing fields around the windings. These fields may affect the operation of the sensor and the wireless communication.

Finally, wireless sensors are conventionally operated on batteries that have a finite life. Thus the quality of data acquisition and communication can deteriorate as the battery becomes weaker. Some sensitive patterns of faults need frequency analysis with data acquired at a higher sampling rate which in turn implies higher transmission rates. Packet delivery performance is important since it translates to data completeness. With such a high sampling rate and transmission rate, the battery life is reduced. We also inspect the packet delivery performance during the whole battery lifetime.

In this work, we study packet delivery performance at the communication stack and the data fidelity of the wireless accelerometer sensor that is used in industrial applications for vibration analysis. The packet delivery performance is related to the reliability in the wireless communication [71]. The data fidelity of wireless sensors measures the quality of wireless communication used in induction motors.

Compared with wired accelerometers, wireless sensor has limited sampling rate and data precision. A comparison between wireless and wired accelerometer measurements answers the question whether the data collected from the wireless sensor is reliable and useful.

4.2 Related Research

There is not much work that has evaluated packet delivery performance on ad hoc or infrastructure based wireless sensor networks (WSN) in industrial environments. Zhao et al. [70] describe results from three different environments on a medium scale (up to 60 motes) ad hoc WSN. The environments they studied are office building hallway, a spacious parking lot and a local state park. Ganesan et al. [72] studied a large-scale (approximately 180 motes) testbed grid on an unobstructed parking lot. Their research focuses

on the loss and asymmetry of packet delivery at both the physical layer and the medium access control (MAC) layer.

Tsai et al. [73] study the feasibility of an In-car WSN and test the wireless communication channel between the base station and a sensor placed under the engine compartment. Their statistical study shows that the In-the-Engine-Compartment channels can satisfy the requirement of up to 98% packet reception rate. Paselli et al. [74] designed a modular wireless sensor node for machine control applications. It demonstrates the feasibility of wireless communication between fixed and moving parts of industrial machines in the distance of 1.5m. However, the power consumption (3W) is very high. Rahimi et al. [75] study the feasibility of extending the lifetime of a wireless web-cam network in building by exploiting mobility. In their system, a small percentage of network nodes equipped with solar cells are autonomously mobile, allowing them to move in search of energy, recharge, and deliver energy to immobile, energy-depleted nodes assuming the static nodes are rechargeable.

There are already some existed industrial applications reported using wireless sensors. Jemielmiak [76] reported a wireless acoustic emission sensor commercially available from some companies such as ARTIS [77], Nordmann [78], Prometec [79]. It is implemented in a machine tool condition monitoring

application. The wireless AE sensor consists of a rotating sensor and a fixed receiver with an airgap of only 0.6mm. Discenzo [80] described a pump condition monitoring application using self-powered wireless sensors. Shen et al. [81] and Bonivento et al. [82] have described their design flow of industrial applications of WSN using commercial nodes. Shen targets the application in industrial process monitoring and controlling. Bonivento presents a case study of a control application for manufacturing plants. This chapter presents an application of industrial WSN by investigating the feasibility of wireless sensor nodes inside induction motors.

4.3 Studies in Small Induction Motors

4.3.1 Equipment and Instrumentation

(a) Motor: A three-phase induction motor from Newman Electric Motors, Inc. stands on a strong-hold steel workbench table. The 1 hp induction motor is connected to an adjustable speed drive from Toshiba International Corporation. The running speed ranges from 0 to 900 rpm and can be adjusted by the speed drive. Figure 4.1 shows the placement of a wireless sensor node inside the induction motor. The diagram shows the leakage magnetic field around the windings outside the stator core. The sensor node inside is exposed inevitably to

the fringing field. The dynamic field when motor running is up to 70 gauss in the peak close to the core edge measured by the hall-effect sensor [83] (in comparison, the maximum field strength of the earth is about 0.6 gauss [84]).

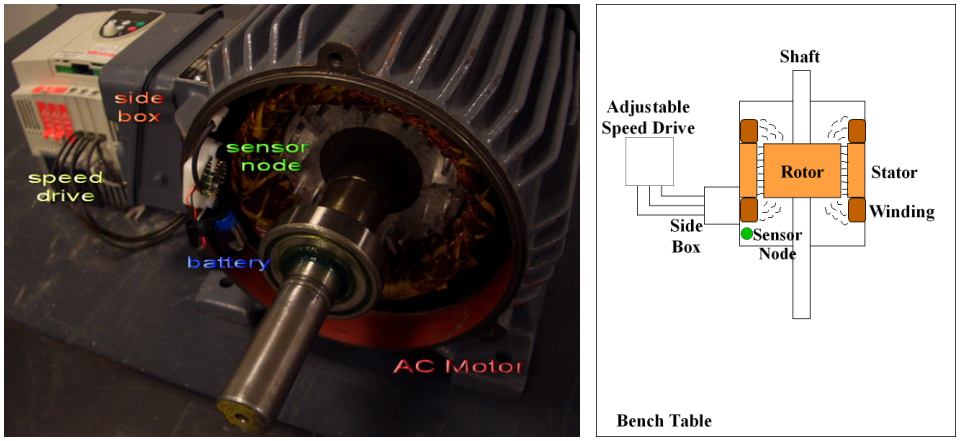

Fig. 4.1 Experiment set up (a) Photo (b) Diagram

(b) Sensor: Three vibration sensors are mounted on the side-box by the double-sided tapes. Vibration specifications are usually expressed in terms of acceleration peak for sine and acceleration RMS for random vibration. Spectral content such as power spectral density curve is used to describe random vibration specifications. The vibration spectral content is compared between these three sensors.

Fig. 4.2 Wireless Sensor Components

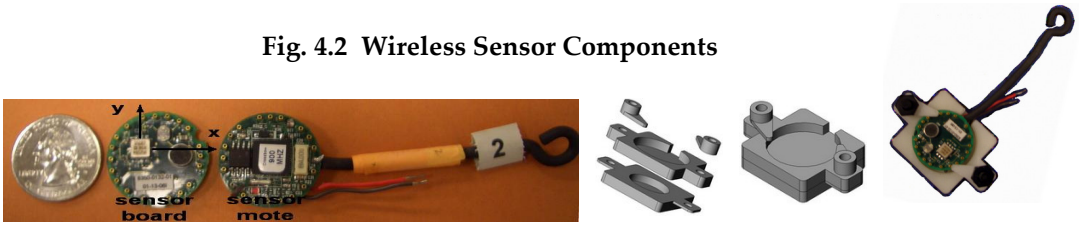

(a) Quarter Size Mica2Dot Sensor Node and Casing

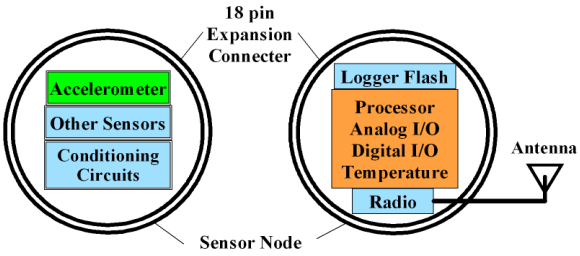

(b) Mica2Dot Sensor Node Block

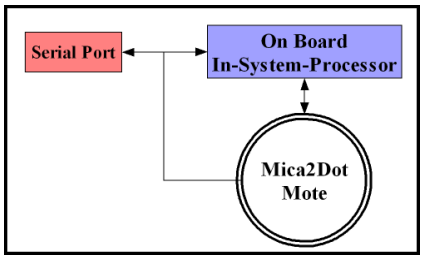

(c) Base Station Block Diagram

(c) Wireless Sensor System: A wireless sensor system consists of at least one sensor node and a base station. A sensor node is comprised of a sensor mote and a sensor board. Figure 4.2 (a) shows the sensor node and its casing. Figure 4.2 (b) gives the corresponding block diagram. The sensor mote (MICA2DOT) hosts an Atmel128L CPU that runs the Tiny Operating System (TinyOS). The operating system executes programs independently written in the programming language nesC [85]. This microcontroller has its maximum clock frequency of 8 MHz and provides the following features: 128K bytes of In-System Programmable Flash with Read-While-Write capabilities, 4K bytes EEPROM, 4K bytes SRAM, An 8 channel 10-bit analog to digital converters (ADC), Real Time Counter (RTC), etc. An external flash memory of 512K bytes is used to store measurements. The

radio center frequency is 916MHz. The data transmission rate is characterized at 38.4 kbits/s. Typically, the power for computing is 24mW, the transmitting power is 81mW and the receiving power is 30mW.

A sensor board is a Peripheral Component Interconnect (PCI) board that can be connected to the mote. The design of the sensor board depends on the type and the number of sensors needed. The sensor node and the programming boards used in the experiment here are commercially available from Crossbow Technology Inc. Figure 4.2 (a) depicts the sensor node in a plastic casing. A magnet is integrated to the bottom layer of the sensor node case. The sensor board and mote is about 25 mm in diameter. The measured data is transmitted from the sensor node and is received by the base station. The base station consists of one sensor node and a programming board. The programming board is connected to a computer by a serial cable. Figure 4.2 (c) shows the block diagram.

(d) Wired Sensor Systems: Wired sensors and data acquisition systems are used to study the fidelity of wireless sensor data. One of the wired accelerometers (from Crossbow, Inc), is a one directional sensor with ±4g measurement range and 500±15mV/g sensitivity. Another accelerometer chip from Analog Devices, Inc. that has better accuracy than the one used in wireless sensor board is used

for cross validation. The measurement range is ±5g and its sensitivity is 174±17 mV/g. The accelerometer chip on the wireless sensor board has its measurement range of ±2g and sensitivity of 167±27 mV/g.

(e) Operation of the Wireless Sensor Node: The sensor node collects data at a sampling frequency of 100 Hz. The data is collected for 2 seconds continuously and stored in a buffer. Then the data is transmitted from the sensor node to the receiver in the form of packets. When all the packets are sent out, the sensor node starts to collect data again. Each measurement data uses 2 bytes of memory; hence the data rate is 200 bytes/s. In the data area for each packet, 20 bytes is used for collected data, 2 additional bytes are used for time stamp, and the last byte is used to mark the Cyclic Redundancy Check (CRC) code. The packet ID number and the time stamp are used to compute the percentage of packets received.

To send a packet, the application layer (in our case, this will be the data acquisition and processing application that runs on the sensor nodes) invokes the communication stack with the packet to be sent and the address of the destination node of the packet. After performing medium access control (MAC) to ensure that there is no other communication in progress on the wireless channel, the MAC layer begins sending the packet one byte at a time. Each byte

is coded and sent over the channel. Simultaneously, a cyclic redundancy check (CRC) code is computed over the entire packet and is appended to the transmission. The receiver receives the coded bytes and decodes them, correcting any single bit errors and flagging double bit errors. When the entire packet has been received, a CRC code is computed by the receiver on this packet and is compared to the CRC that was computed and transmitted by the sender. If the CRC from the sender and the receiver do not match, the packet is rejected as spurious. If the packet is incomplete it is considered a damaged packet. CRCs are popular because they are simple to implement in binary hardware, are easy to analyze mathematically, and are particularly good at detecting common errors caused by noise in transmission channels.

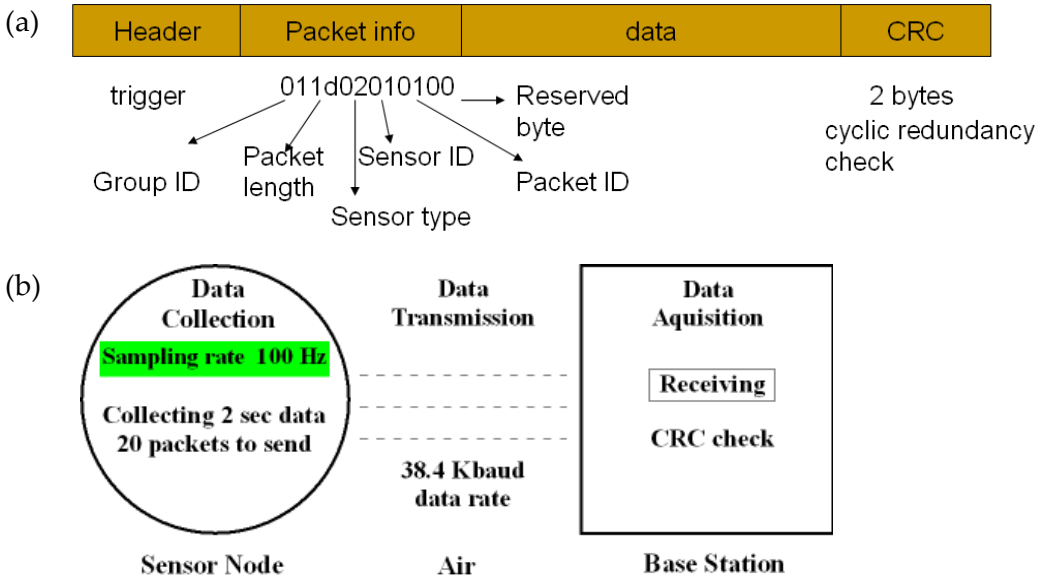

Fig. 4.3 (a) Packet Construction (b) Packet Transmission Flow

Figure 4.3 shows the packet construction and packet transmission flow. Each packet has 29 data bytes. In the data column for each packet 20 bytes are used for collected data, two bytes for the time stamp, and two to mark the CRC checking results.

The Berkeley media access control (B-MAC) [86] protocol is used in this study. B-Mac is a reconfigurable carrier sense multiple access (CSMA) protocol that achieves low power processing, collision avoidance, and high channel utilization. The B-MAC contains a clear channel assessment (CCA), to determine if the channel is clear for collision avoidance, and packet back off, link-layer acknowledgement, and low power listening (LPL) [87].

4.3.2 Experiments

4.3.2.1 Packet Delivery Performance

The most basic aspect of wireless communication is the packet delivery performance. In order to characterize the packet delivery performance, we investigate the packet loss rate (the fraction of packets that were transmitted within a time window, but not received) or its complement - packet reception rate. The number of packets that fail the CRC checks is also recorded. Therefore

we measure two metrics: 1) percentage of packets received; 2) percentage of packets without error.

In Figure 4.4, a side-box is on the left side where the winding terminals usually come out and connect with the power source. There is always some part (at least a hole) not sealed with metals. In fact, industrial totally enclosed small motors are not really completely enclosed/sealed. A radio frequency signal encounters objects that reflect, refract, diffract or interfere with the signal and can be then received outside. In order to study the spatial characterizations, we use three base stations (see Figure 4.4) to receive the signal from three different directions and vary with the distances. The sensor node is located at the stator of the motor or on the shaft. We also check the packet delivery performance along the battery lifetime in the base station 2 direction with the sensor node on stator.

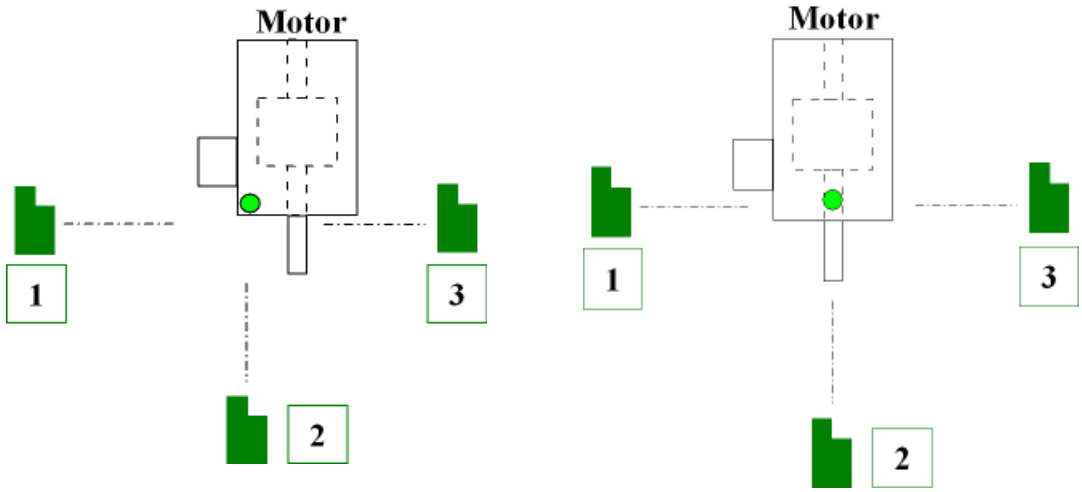

(a) Sensor node on stator **(b) Sensor node on shaft**

Fig. 4.4 Three base station set-up

Experiments show that there are points where there is zero or faint signal reception. This is due a phenomenon called fading effect. Fading is caused by interference between two or more versions of the transmitted signal which arrive at the receiver at slightly different times. These waves, called multi-path waves, combine at receiver antenna to give a resultant signal which can vary widely in amplitude and phase, depending on the distribution of the intensity and relative propagation time of the waves and the bandwidth of the transmitted signal. Signal nulling occurs when the reflected waves arrive exactly out of phase with the main signal and cancel the main signal completely. To investigate the fading phenomenon, we move the base station in steps of 1cm on either side of one null signal point. The base station position is showed in Figure 4.5. We also check the same locations for the sensor node on shaft.

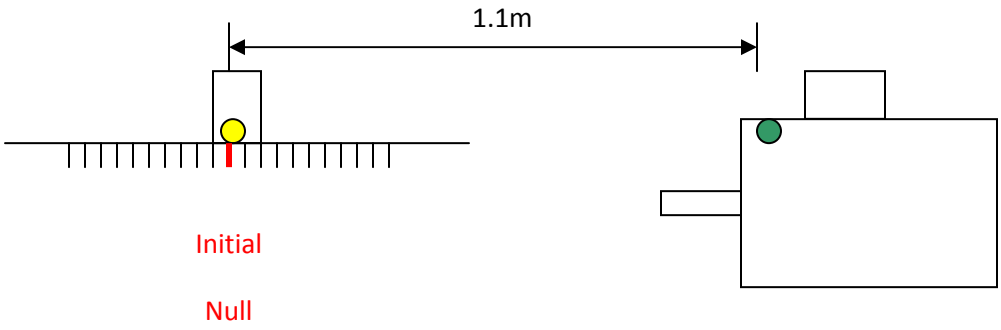

Fig. 4.5 Fading effect observation

4.3.2.2 Data Fidelity

In order to monitor the motor health, the vibration frequency spectrum needs to be monitored. The wireless sensor and two wired sensors are installed on top of the side box in the same direction. All of them are mounted by a double sided tape. With the motor running, these sensors should detect the same frequency contents. This setup cannot be done inside the motor because the curvature of the motor housing makes it very hard to install three sensors at the same position. Instead, we use each of the wired sensor set up with the wireless sensor at the same position but one inside and one outside (Figure 4.6).

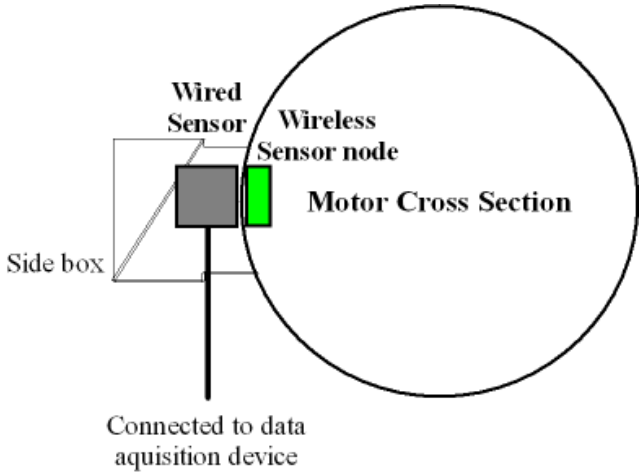

Fig. 4.6 Inside/outside wireless/wired sensor set-up

4.3.3 Experimental Results and Discussion

The first experiment is to study the spatial characterization of packet delivery performance. The reception rate of three base stations (see Figure 4.4) is

shown in Figure 4.7. The total height of the bars is the percentage of packets received. The green bar represents the percentage of the packets that have CRC ok. When the sensor node is installed on the stator, the reception rate of base station 1 is above 98% until as far as 3 meters away from the sensor node. It seems that there is no null point when the sensor node is on the shaft.

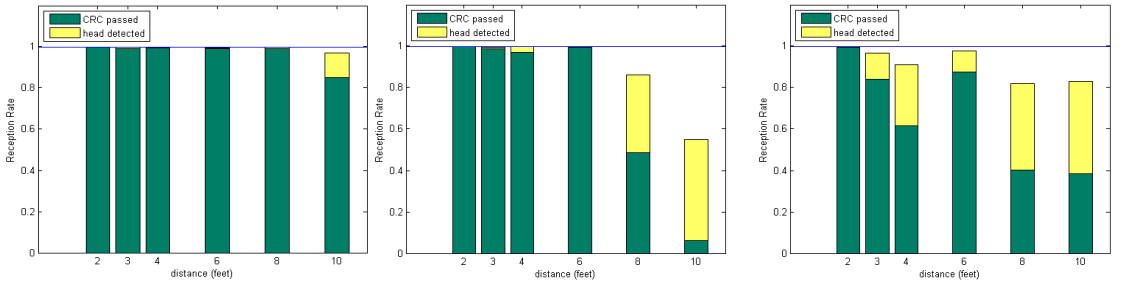

Base station 1 Base station 2 Base station 3

(a) Wireless sensor node on stator

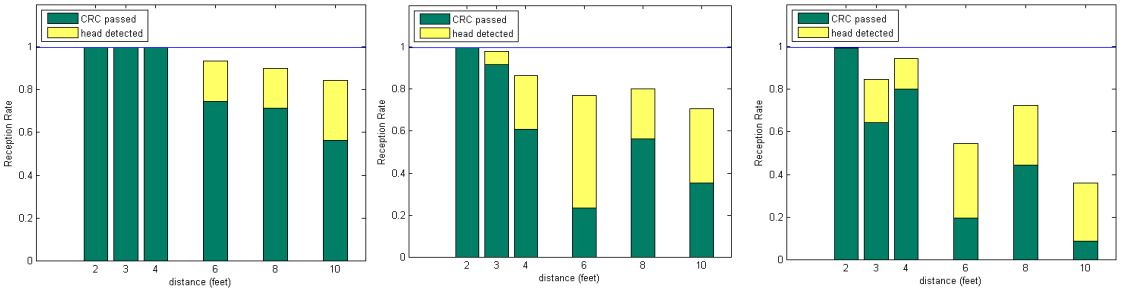

Base station 1 Base station 2 Base station 3

(b) Wireless sensor node on shaft

Fig. 4.7 Spatial characterization

The second experiment was conducted for a continuous period of 42 hours to investigate the time based difference of packet delivery performance. Figure 4.8 shows two base stations' packet delivery performance in the direction of base station 2 in Figure 4.4. The packets are collected every 30 minutes before

1500 minutes and every hour after that. The closer base station (approximately 0.5m) shows very good data reception rate in the time span of continuously running for 39 hours. The farther base station (approximately 1.35m) shows a clear degradation of the CRC passed rate in the first 10 hours. The reception rate keeps above 80% until the last 3 hours of operation. The CRC passed rate in Figure 4.8(a) got better performance before the battery died. It is probably because of the variance of the environment.

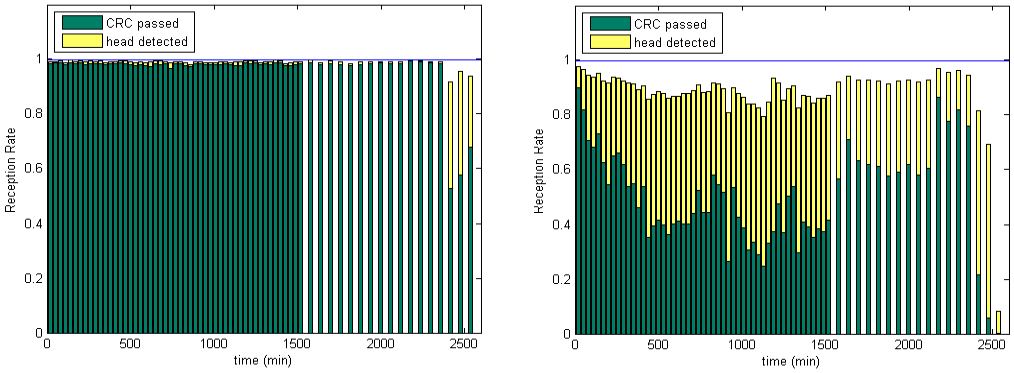

(a) Base station at 0.5m **(b) Base station at 1.35m**

Fig. 4.8 Time based difference

During the experiments above, we found there are always some null points that no signal can be received at particular position. These null points are due to fading in wireless communication and will affect the packet delivery performance and eventually the data quality. To explore further, the base station was placed at a point of low reception. This point was approximately 1.1m from

the sensor node as seen in Figure 4.5. The base station was then moved in steps of 1 cm in each direction. Figure 4.9 shows the results of packet delivery performance besides this null point. As can be seen there are some other null points found in the position closer to the sensor node because of the multi-path effect in the indoor environment. The sensor platform uses low-power radios which do not have enough frequency diversity to reject multi-path propagation. Thus the position of receiving node outside the motor should be carefully chosen when the sensor network is set up. At the same location, Figure 4.9 (b) shows if the sensor node is installed on the shaft and rotates when the motor is running, the losses are relatively uniform because the mobility of the sensor node provides more transmission path than the fixed one.

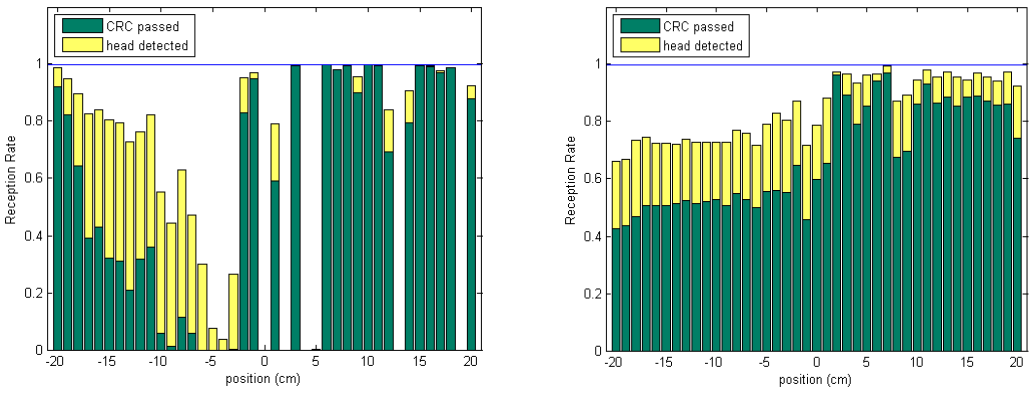

(a) Sensor node on stator **(b) Sensor node on shaft**

Fig. 4.9 Fading effect observation

In order to investigate the data fidelity of wireless accelerometer, two wired sensors are used to compare with the wireless sensor. One wired sensor and its data acquisition board is from Crossbow, Inc. This acceleration has a sampling rate about 180Hz. The other wired sensor is an evaluation board with the accelerometer chip from Analog Device, Inc. A 3V DC power supply and a data acquisition device are used for this evaluation board. This accelerometer has a sampling rate of 100Hz. Figure 4.10 (a) shows the spectral analysis of three accelerometer sensors on the side box. Figure 4.10 (b) and (c) shows the spectrum of each wired sensor outside compared with wireless sensor inside the motor.

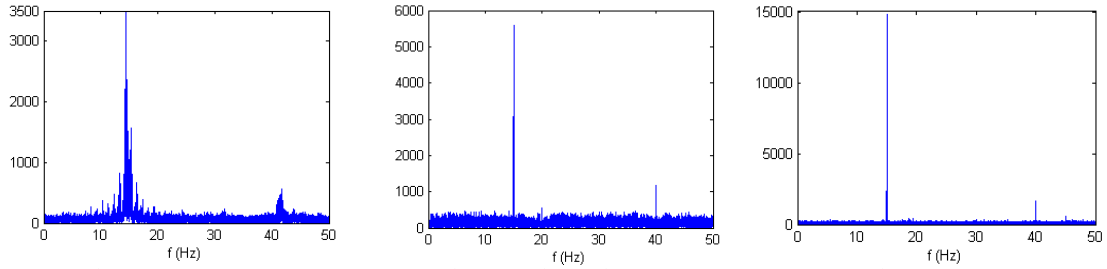

Wireless sensor spectrum | Evaluation board spectrum | Wired sensor spectrum

(a) Three sensors on side box

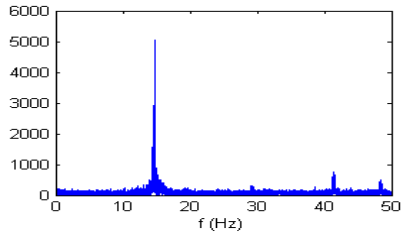

Wireless sensor inside

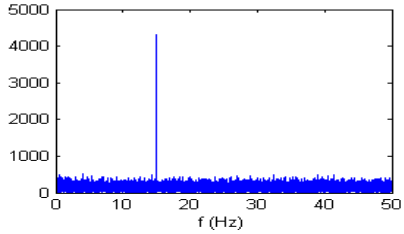

Wired sensor outside

(b) Compared with wired accelerometer

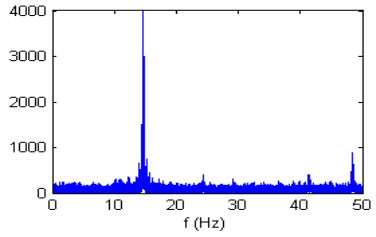

Wireless sensor inside

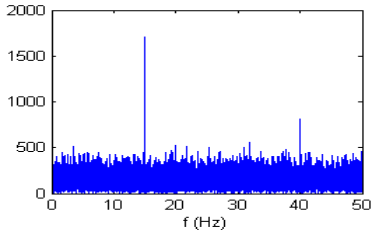

Evaluation board outside

(c) Compared with evaluation board

Fig. 4.10 Vibration sensor frequency analysis

The motor is running at 900 rpm (15Hz). The spectrum clearly shows the main frequency peak and other unknown contents. The wired accelerometer has lowest noise level because of its higher sampling rate. As can be seen their frequency spectra match very well. The wireless sensor spectrum has a slight frequency shift due to small sampling rate and short data collection period. It

can be improved by changing the sampling rate and by taking longer recording time period.

4.4 Studies in Large Induction Motors

4.4.1 Experiment Setup

The motor used in this study is a three-phase 200 horse power (hp) alternating current (AC) motor running at 1800 rpm and a voltage of 460 volts. The motor is mounted on a flat metal table. Three sensors are used – one wired and two wireless. The sensors and data acquisition devices used are as same as the ones in small induction motor studies. The wired sensor (▣) monitors the same point on the outside of the stator frame as the wireless sensor (●) inside the stator frame.

Figure 4.11 (a) shows the wireless sensor on a metal plate (9mm x 5.5mm x 0.5mm), wrapped around with resin tape attached to the motor inside the stator frame. The accelerometers on the sensors attached to the stator frame are directed downwards. Another wireless sensor is attached on to a metal collar (Figure 4.11 (b)). The collar is bolted on the shaft of the motor also wrapped around with resin tape; the accelerometer is mounted so that it measures accelerations in the radial direction.

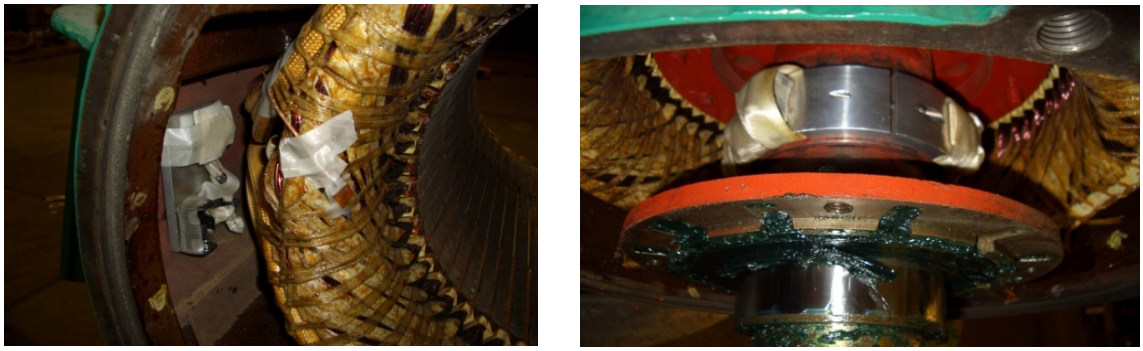

a)Wireless sensor on Stator Frame b) Wireless sensor on Shaft

Fig. 4.11 Wireless Sensors attached to the a) Shaft and b) Stator Frame

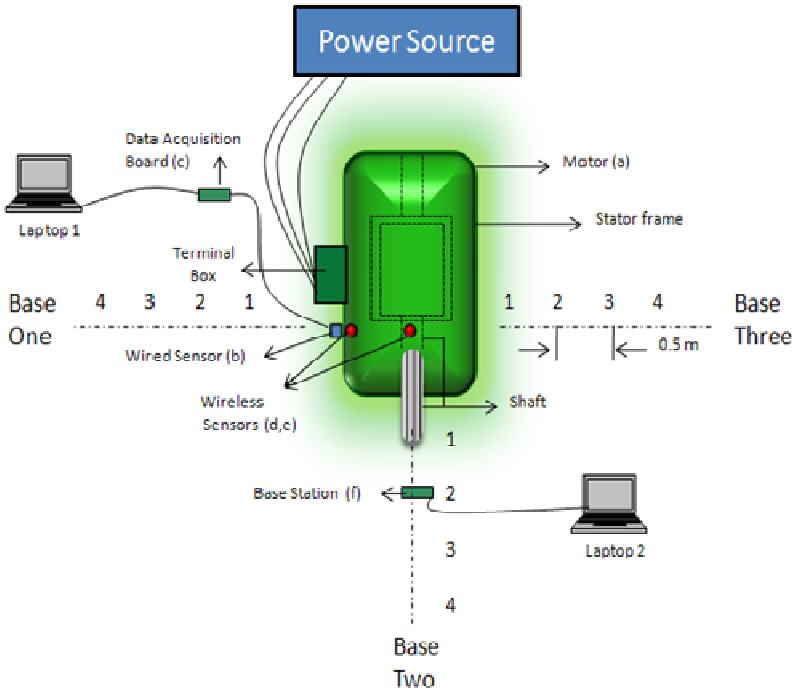

Fig. 4.12 Top view of the experiment setup for large induction motor feasibility study

Figure 4.12, shows a top view of the experiment set up. On the top left side of Figure 4.12, the wired sensor is connected to a data acquisition (DAQ)

board. The DAQ board is connected to a laptop computer. The two wireless sensors communicate with the base station on the bottom right of Figure 4.12.

4.4.2 Methodology

The spatial dependence of the wireless communication in this study is studied by using three base stations to receive the signal from different directions and distances. Figure 4.12 above shows the three different base stations. Each base station is studied at four different points, 0.5 meters apart from each other. The farthest distance between the motor and base station was 2 meters. The base station, MIB510CA was placed at each point for three trials to collect data. Each trial had a time period of three minutes. A total of 36 trials where performed. The packet deliver performance is studied by analyzing the successful reception of packets.

4.4.3 Experimental Results and Discussion

The following results show the packet delivery performance of the wireless communication between the wireless sensors inside the motor and the base station. The packet reception rate of the wireless sensors on all four points (P1-P4) from Base One, Two, and Three (B1-B3) for the stator and shaft are shown in Figure 4.13 and Figure 4.14, respectively. Note the symbols B1P1 represents B1= Base One and P1= Point One. The height of the green (dark) bars

represents the percentage of the packets that were received completely passing the CRC check, percentage of normal packets (NNP). The yellow (light) bars represent the damaged packets (i.e., were corrupted), did not pass the CRC check.

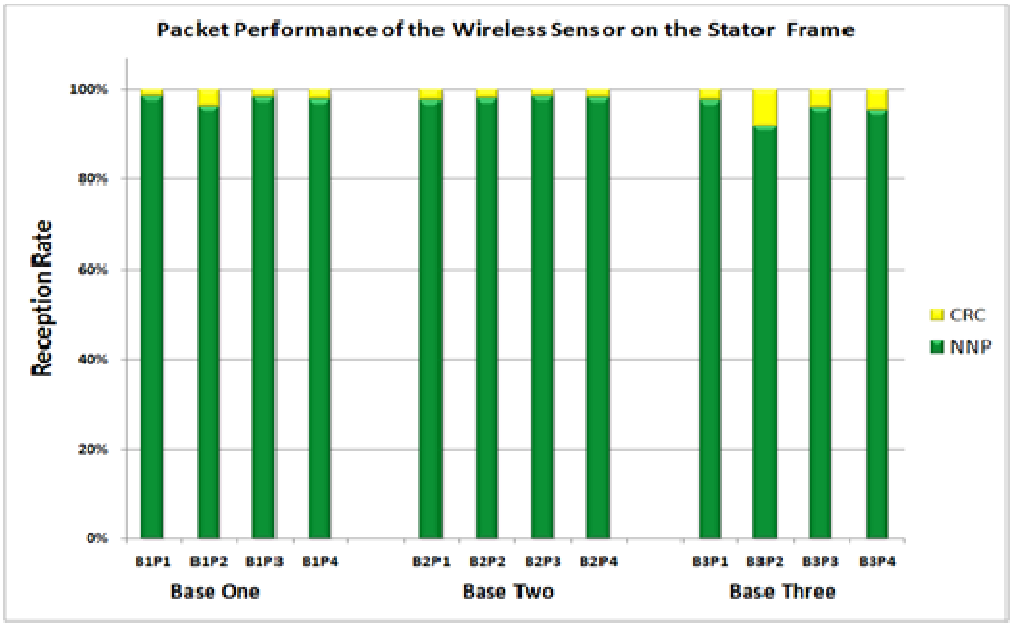

Fig. 4.13 Spatial Characterization of the Wireless Sensor on the Stator
(Note: B1P1= B1-Base One P1-Point One)

Figure 4.13 shows the packet reception rate from the sensor node on the stator frame. The performance of the wireless senor node attached to the stator frame did not vary much with distance. The packet performance based on the location had a slight variation; Base Three had the most damaged packets of 4.6% CRC. Overall the sensor node attached to the stator frame received an average reception rate of 97.10% of normal packets.

Table 4.1 is a summary of the packet delivery performance of the wireless sensor on the stator frame; shows the average of all four points.

Table 4.1: Average Packet Delivery Performance (Stator Frame)

	Base One	Base Two	Base Three	Mean
NNP	97.73%	98.17%	95.40%	97.10%
CRC	2.27%	1.83%	4.60%	2.90%

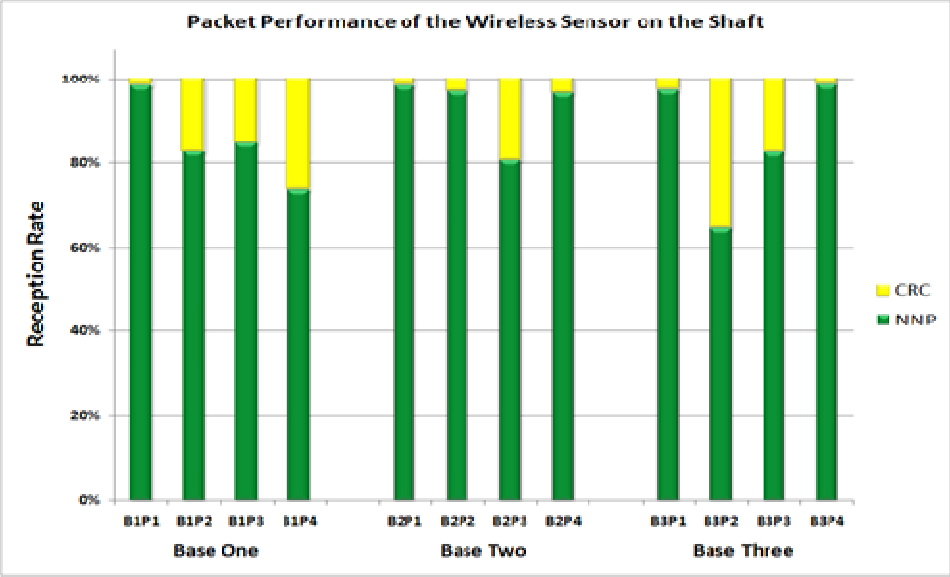

Fig. 4.14 Spatial Characterization of the Wireless Sensor on the Shaft

Figure 4.14 shows the packet performance of the wireless sensor on the shaft of the motor. The performance of the sensor attached to the shaft did vary based on the location of the base station. Base One and Three had bad reception rate compare to Base Two. The packet delivery performance of the wireless sensor node on the shaft had nearly four times more damaged packets CRC then the wireless sensor on the stator frame.

Table 4.2 is a summary of the packet delivery performance of the wireless sensor on the shaft; shows the average of all four points.

Table 4.2: Average Packet Delivery Performance (Shaft)

	Base One	Base Two	Base Three	Mean
NNP	84.90%	93.14%	85.73%	87.93%
CRC	15.10%	6.86%	14.27%	12.07%

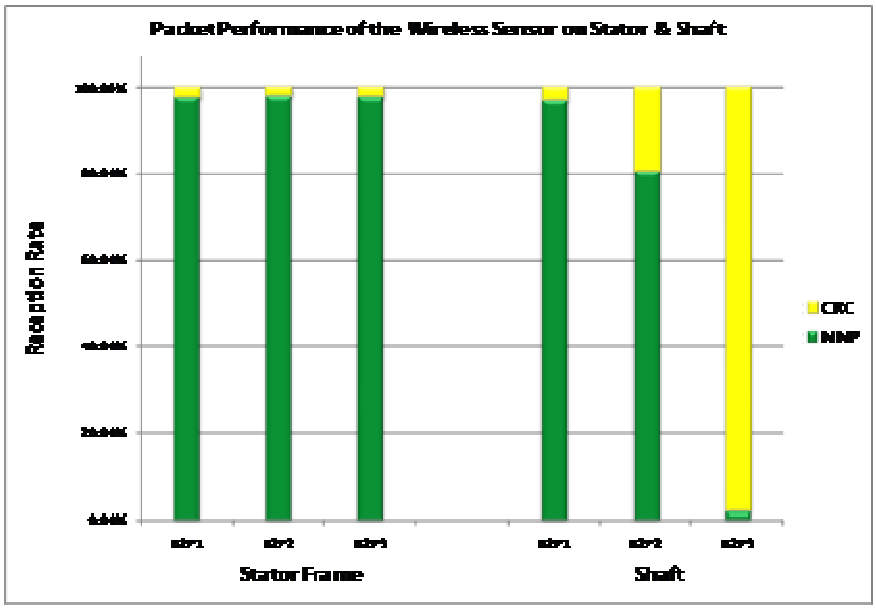

Fig. 4.15 Packet Delivery Performance at 5 meters

Figure 4.15 shows the packet delivery performance of the wireless sensor on the stator frame and shaft at three distances (P1=0.5m, P2=1m, and P3=5m) on Base Two. This was performed to study the signal transmission at farther distances. The results show that the reception rate of the wireless sensor on the stator frame does not vary much at farther distances. The reception rate from the wireless sensor on the shaft however shows a big decline.

Table 4.1 and 4.2, shows the average packet delivery performance of the wireless sensor on the stator frame and shaft respectively, both show Base One and Three having bad reception rate compare to Base Two. Recall that the wireless sensor on the stator frame had a slight variation based on location whereas the wireless sensor on the shaft had more than twice the damaged packets on Base One and Three. The wireless sensor on the shaft was positioned to measure the acceleration in the radial direction, Base One and Three are parallel in this direction whereas Base Two is perpendicular. The wireless sensor on the shaft was exposed to a dynamic field, rotating at nearly 1800rpms, and electromagnetic field.

Figure 4.16 shows the packet delivery performance of the wireless sensor on the shaft, when the motor is OFF and ON. This was performed to study the signal transmission being exposed to an electromagnetic field while running at 1800rpms in radial direction. The data was taken on Base One (B1), points one through four (P1-P4). Each point was 0.5 meters apart.

When the motor was OFF the reception rate had an average of 98%. Figure 4.16 shows the signal transmission performing poorly at farther distances when the motor was ON compared to when it was OFF. The packet delivery performance when the motor was ON had a low reception rate of 73.8% at the

farthest point and an average of 84.9% from all four points. On Figure 4.15, the wireless sensor on the shaft did have a big decline on the reception rate at farthest distance compared to the wireless senor on the stator frame. The wireless sensor on the shaft had more damaged packets at farther distances being exposed to a different environment (dynamic and electromagnetic field) than the wireless sensor on the stator frame.

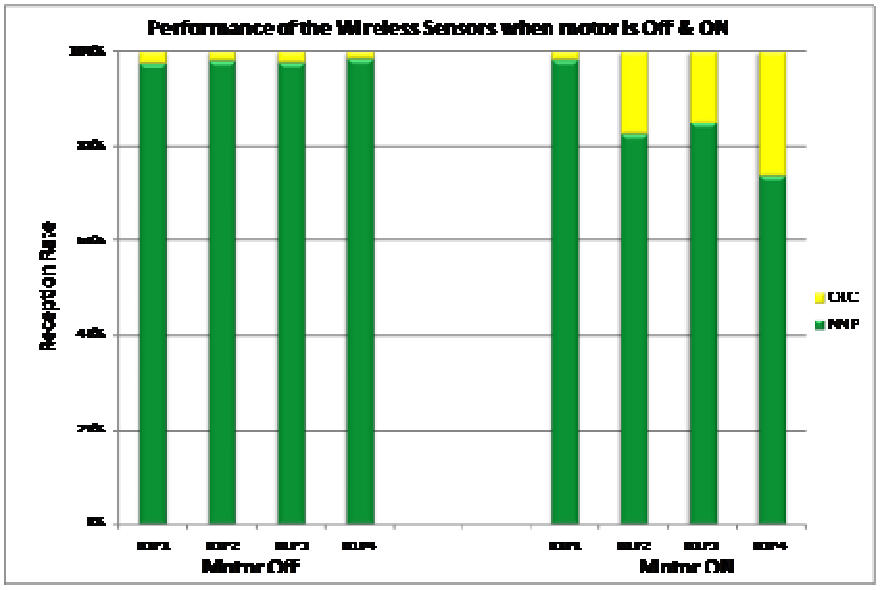

Fig. 4.16 Packet Delivery Performance when motor is OFF and ON

Variations of the received power are usually caused by the change in the transmission medium or paths of the wireless signals [73]. Fading effects can be caused by the interference between multiple versions of the transmitted signal which arrive at the receiver at slightly different times [73]. There are three different propagation effects that can occur in the motor environment i)

Reflection when an electromagnetic signal encounters a surface that is large relative to the wavelength of the signal. ii) Diffraction when a radio wave encounters an edge, wave propagates in different directions, iii) Scattering occurs when the size of the obstacle is on the order of the wavelength of the signal or less, and an incoming signal is scattered into several weaker outgoing signals [73, 88]. Considering the geometric structure inside an AC motor, electromagnetic waves encounter a lot of fading effects. These effects just mentioned could cause the wireless signal to propagate through different paths arriving at the antenna of the receiver with different amplitude, phase, and time [73].

For data fidelity study, the same wired sensor and data acquisition system are used to analyze the fidelity of the wireless sensor attached on the stator frame. Figure 4.17 shows the vibration frequency analysis of the a) wireless and b) wired sensor on the stator frame.

The accelerometer on the wired and wireless sensor has a sampling rate of 100 Hz. The motor is running at 1800 rpm, hence 30 Hz is the main frequency peak. The frequency spectra of the wired and wireless sensor have prominent frequency peaks at 30 Hz. The frequency spectrum of the wireless sensor has other frequency peaks at 12 Hz, 13 Hz, and 47 Hz. The frequency spectrum of the wired sensor has additional frequency peaks at 10 Hz, 11 Hz, and 20 Hz.

Further investigation is required to see the cause of these frequencies and difference between the wireless and wired sensor results. One factor to help distinguish the results is to consider the method the wireless and wired sensor were attached. The wired sensor was attached using double-sided tape whereas the wireless sensor was attached on a metal plate.

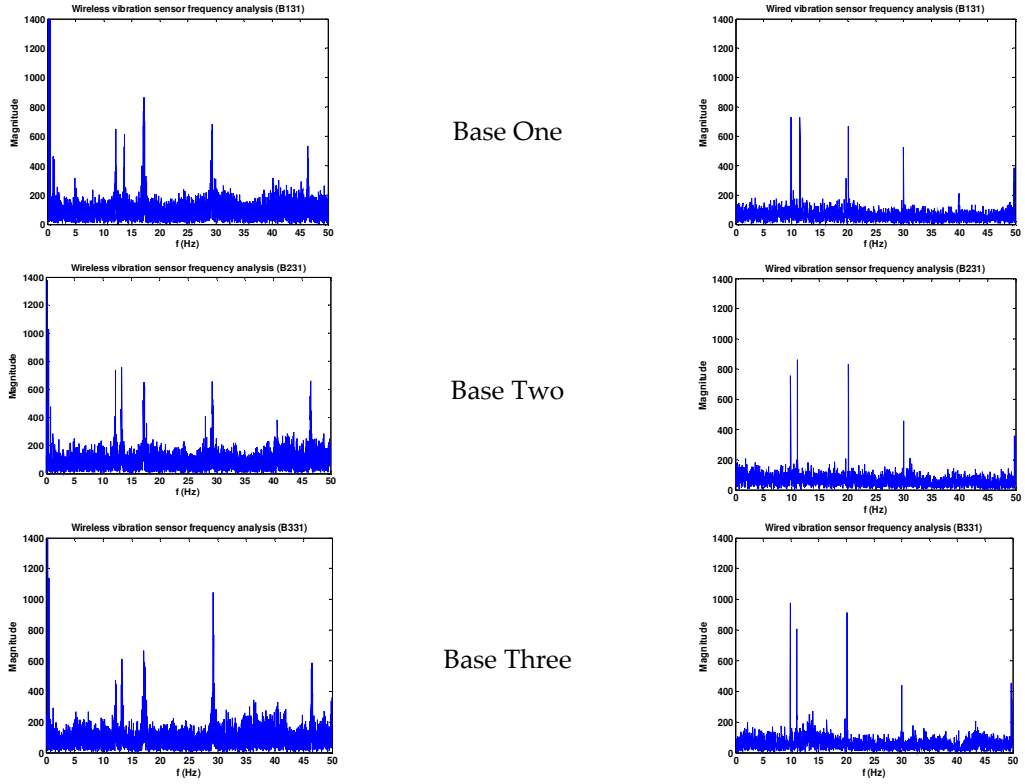

a) Wireless b) Wired

Fig. 4.17 Vibration analysis on stator frame for a) Wireless b) Wired sensor
(Wireless data collected from Base One, Two, Three)

Data was taken with the wireless sensor attached with double sided tape. Comparing the wireless sensor and wired sensor with double-sided tape, peaks

at 10 Hz, 20 Hz, and 30 Hz did match. The remaining frequency peaks not matching could be due to other factors or due to the micro-sensors themselves.

4.5 Summary

In this chapter, we have described results from a collection of vibration measurement experiments designed to demonstrate the feasibility of wireless sensors for health monitoring in both small and large induction motors. The wireless sensor node inside the motor can always send out signals to the base station outside in a 0.6m circular region. For totally enclosed motors, the side box side has always some parts without metal. At some points even as far as 2.5m, the packet delivery performance is also satisfactory. The battery under very high transmitting load can last as long as 40 hours. The packet delivery performance does not show clear difference along most of the battery lifetime. Due to multi-path propagation phenomenon, there are some null points where the signal gets canceled. The position has to be adjusted to find the position of high reception. Vibration data from the wireless sensor shows a promising accuracy of frequency spectrum comparable to the more reliable wired sensors. Battery life is a limiting factor in the application of wireless sensor technology. As the battery degrades, performance deteriorates. The most power-intensive aspect of the operation of these nodes is the communication. If communication is reduced by on-board

processing of the measured data, then the battery life can be lengthened considerably.

One attractive aspect of the wireless nodes is that they can accept measurements from several sensors. They can also perform local computations and signal processing. This feature further reduces the transmission load and extends the life of the battery. Finally, wireless sensors are low power devices and can be powered by energy scavenging methods from available environmental sources such as vibrations and magnetic fields.

CHAPTER 5

MULTI-FAULT ANALYSIS IN INDUCTION MOTORS USING WIRELESS SENSORS

This chapter describes a wireless health monitoring and fault classification system for drive connected three-phase induction motors. The wireless sensor nodes are developed based on commercially available programming modules and sensor boards. A two stage hierarchical classification system is designed for the fault diagnosis. Based on the wired sensor experiments, the HHT features of vibration sensor and the FFT features of flux (current) and acoustic sensors are selected as features for the classification. The first stage contains five categories and the second stage contains 3 subclasses for each fault category. The results demonstrate the effectiveness of the system.

5.1 Overview of Wireless Sensor Network for Motor Condition Monitoring

Wireless Sensor Networks (WSN) provide an effective platform to gather and analyze data without human intervention[15]. The unique characteristics of the IEEE 802.15.4 [89] standard such as the flexibility, inherent intelligence, fault tolerance, low cost, and rapid deployment make WSN the ideal structure for

low-cost motor monitoring system for industrial plants. Typically, a sensor network consists of autonomous wireless sensing nodes that are organized to form an adhoc network that relays the sensor data to a specified destination for processing. Each node is equipped with sensors, embedded processing unit, short-range radio communication module, and power supply.

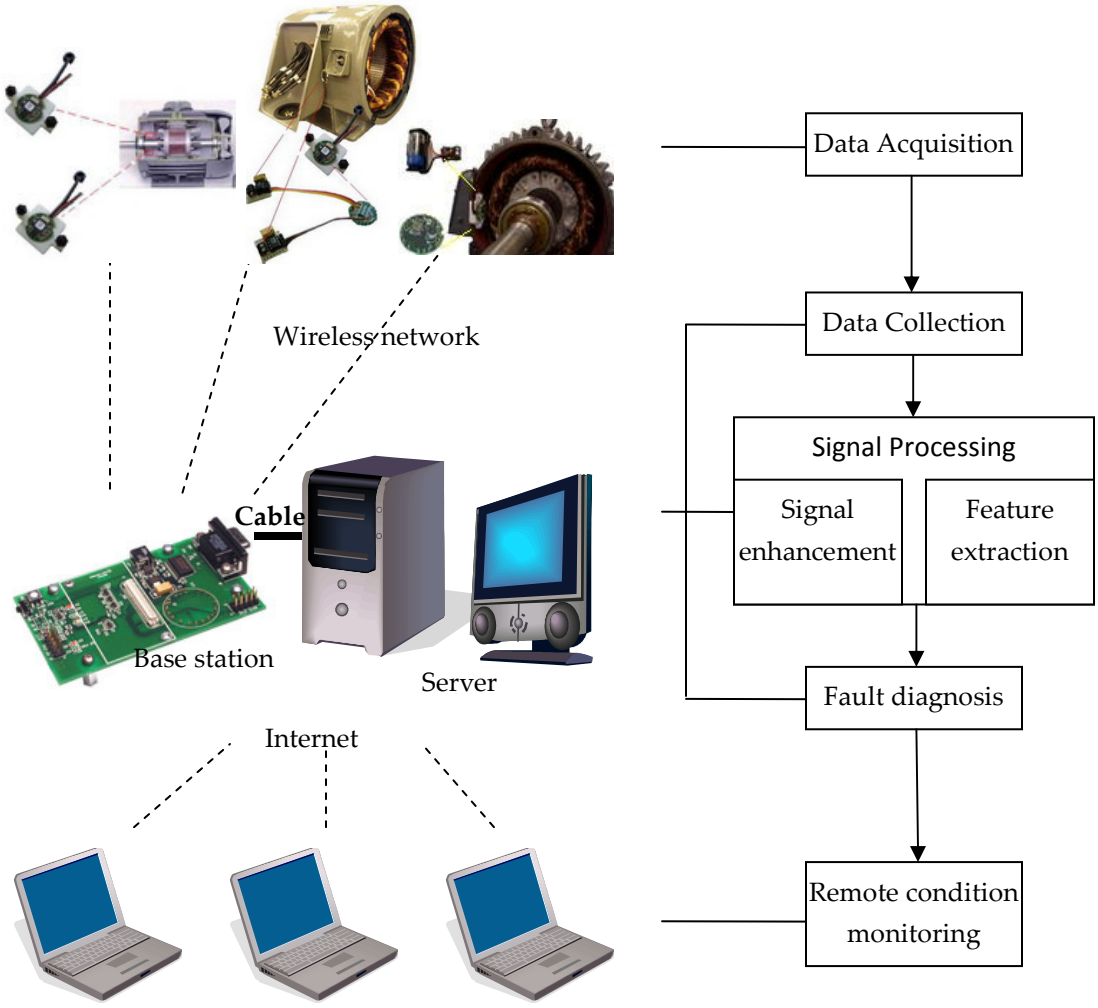

Fig. 5.1 Three-layer Wireless Condition Monitoring System Framework. Reproduced from Xue et al (2007)

A typical three layer motor monitoring system [90] is illustrated in Figure 5.1. The first layer is the data acquisition layer which is composed of integrated sensor nodes. In the second layer, a base station board collects the data from different wireless sensor nodes. The base station is connected to a server computer through a serial port cable. A laptop can be used as a server computer as well. All the data collected is saved in the database and the signals can be processed by using various signal processing techniques. The decision for maintenance thus can be made based on the wider view of the information. Different sensors can provide compensating information using sensor fusion techniques for helping the decision making. The third layer provides a connection for human user interfaces to the system. The user can catch the global view of the machine and the condition monitoring can be carried out remotely.

5.2 Wireless Sensor Node

In this study, an Imote2 [91] sensor node is used instead of MICA2DOT described in the previous chapter. Imote2 is the newest version of wireless sensor module which is designed for demanding applications requiring high CPU and wireless link performance and reliability.

5.2.1 Hardware

The Imote2 sensor node designed by Intel is comprised of a sensor module (also called sensor mote) and a sensor board. Figure 5.2 clearly depicts the top and bottom view of the sensor mote. This platform is built around a low power XScale processor, PXA271. It integrates an 802.15.4 radio (ChipCon 2420) and a built-in 2.4 GHz antenna. The processor can operate in a low voltage (0.85V) and a low frequency (13 MHz) mode, hence enabling low power operation. The frequency can be scaled to 104 MHz at the lowest voltage level, and can be increased up to 416 MHz with dynamic voltage scaling. The radio chip (CC2420) supports a 250 kb/s data rate with 16 channels in the 2.4 GHz band. The integrated antenna enables the sensor mote to provide a nominal range of about 30 meters. This sensor mote supports a variety of operation system options. The open source Tiny Operating System (TinyOS) is installed for this study. This operating system executes programs independently written in the programming language nesC [85]. Other operating system such as Linux, .Net Micro Framework can also be installed for different applications.

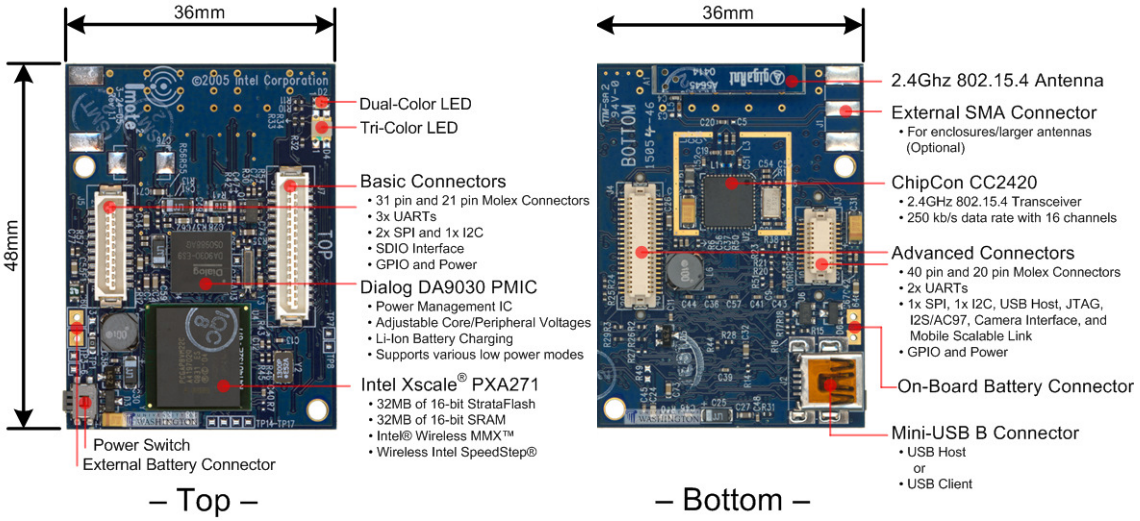

Fig. 5.2 Top view and bottom view of Imote2 sensor mote.
Source: University of Washington, research wiki

To supply the processor with all the required voltage domains, the sensor mote includes a power management chip (PMIC). This PMIC supplies nine voltage domains to the processor in addition to the dynamic voltage scaling capability. It also includes a battery charging option and battery voltage monitoring. Two of the PMIC voltage regulators (1.8 V & 3.0 V) are used to supply the sensor boards with the desired regulated supplies at a maximum current of 200 mA. The platform was designed to support primary and rechargeable battery options in addition to being powered via USB.

Imote2 is a modular stackable platform and can be stacked with sensor boards to customize the system to a specific application, along with a "power board" to supply power to the system. Figure 5.3 shows the compatible sensor

board commercially available from Crossbow Technology, Inc. It contains a three-axis accelerometer (squared in Figure 5.3 (a)) and a 4 channel 12-bit Analog to Digital Converter (ADC). Additional sensors with analog input can be directly connected to this sensor board through the analog sensor interface connector shown in the left part of Figure 5.3 (a).

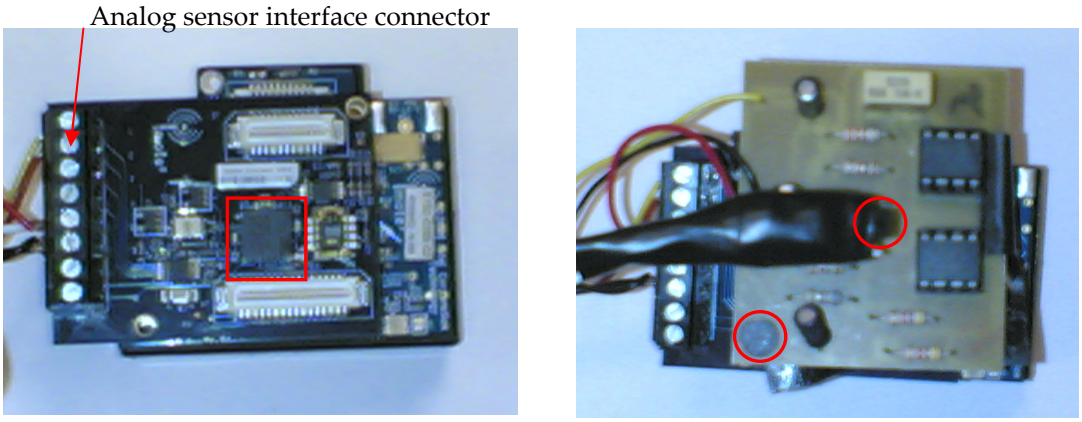

(a) sensor board with accelerometer sensor

(b) additional sound board and hall-effect sensor

Fig. 5.3 Wireless sensor board (a) sensor board with accelerometer (b) additional sound board and hall-effect sensor

An additional sound board is designed for this sensor board since there is no microphone sensor included in this sensor board. The sound board circuit diagram is shown in Figure 5.4. The microphone signal is first pass a high pass filter to get rid of DC components. The dynamic signal is then amplified. To avoid aliasing, a low pass filter is used before the signal goes to the ADC.

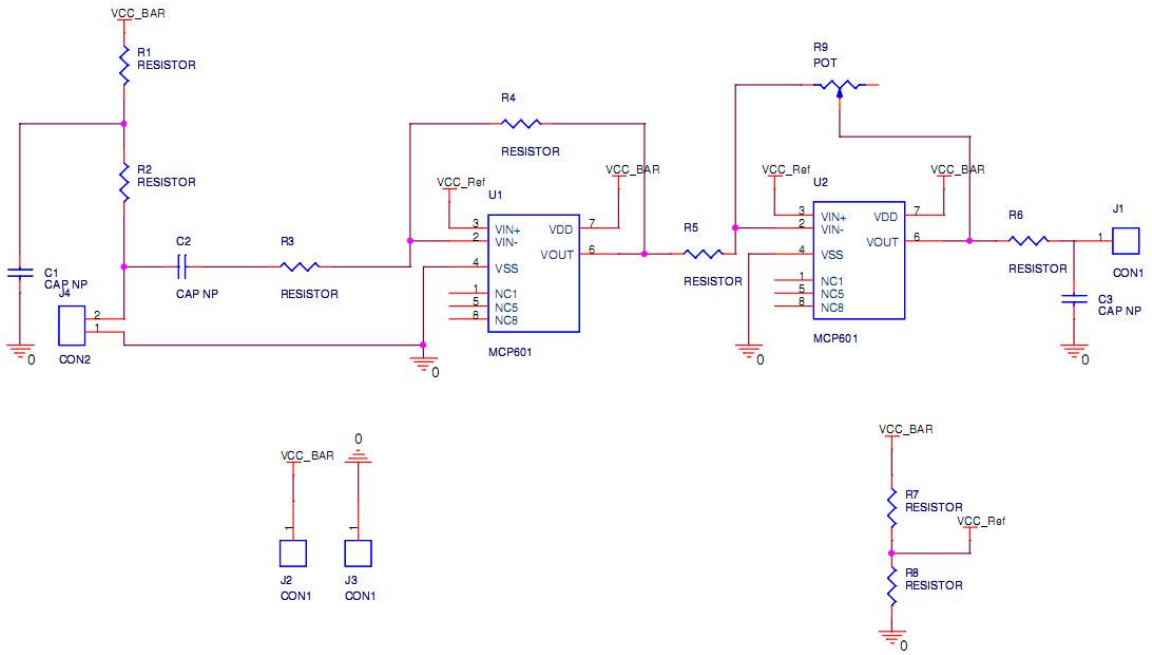

Fig. 5.4 Sound sensor board circuit diagram

The hall-effect sensor from Allegro MicroSystem, Inc. is directly connected to the analog sensor interface connector. No additional signal conditioning circuit is required. The sound and the hall-effect sensor output are tuned to be a voltage range from 0 to 3V. The resolution depends on the 12-bit ADC. The sampling rate of the sound and hall-effect sensors can achieve 5.186 kHz which depends on the scanning speed of the ADC channel.

5.2.2 Operation

The sensor nodes collect data at a sampling frequency as programmed. The vibration data is collected for 4 seconds continuously; the flux and sound are collected for 2 seconds continuously. The data is stored in a buffer is transmitted

from the sensor node to the receiver in the form of packets when the buffer is full. When all the packets are sent out, the sensor node starts to collect data again. Each measurement data uses 2 bytes of memory. For each packet, the sensor node ID and the packet ID number are used for data process. In the data area, 114 bytes is used for collected data, 1 additional byte is used to mark the Cyclic Redundancy Check (CRC) code. The detail of packets and CRC checking process are introduced in chapter 4.

5.3 Method

5.3.1 Overview of Wireless Motor Health Monitoring System

In this study, a wireless motor health monitoring system is built based on the same set of experiments described in the wired sensor system in chapter 2. Figure 5.5 shows the process of wireless motor health monitoring and fault classification. Wireless sensor nodes acquire vibration, sound and flux data from the motor and send the data to the receiver—the base station. The base station collects the data and saves it to the server database. The server computer then processes the signal and classifies the features.

The two-stage classification scheme is implemented as same as the wired sensor system shown in Figure 3.6. The feature vector is first used in the 5-

category classifier. If the 5-category classifier classifies it as the normal condition, then no action will be made until the next feature vector is acquired. If it is not classified as the normal condition, the feature vector will be used again in the corresponding subclass classifier based on the result of the 5-category classifier. After the subclass classifier finishes the computing, a certain faulty condition will then be sent to the operator. A new set of monitoring and fault classification process will start again based on the pre-determined monitoring interval.

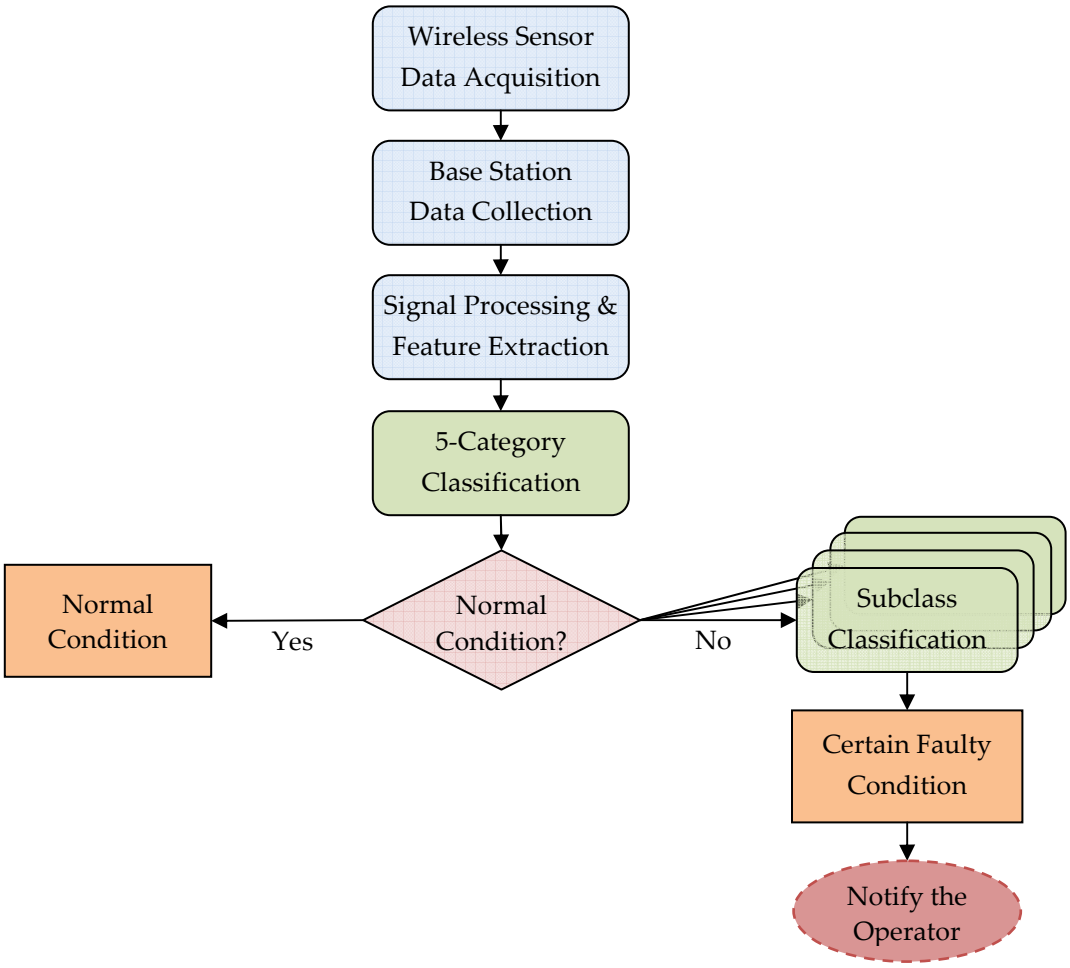

Fig. 5.5 Wireless motor health monitoring and fault classification process

5.3.2 Experiment Setup

(a) Equipment and Instrumentation

Figure 5.6 shows the experiment setup for this study. A three-phase induction motor drives a DC generator through a pulley mechanism. The motor used here is a 1hp 8-pole AC motor rated at 230V line voltage and 5.2A line current. It is connected to an adjustable speed drive to control the speed. The

running speed of the motor with no load is 900 rpm which corresponds to 15 revolutions per second (15 Hz). The running speed of the motor with load will vary but will typically be less than 900 rpm. A laser tachometer is used to measure the running speed. The DC generator is a 1hp DC motor rated at 180 V output DC voltage and 5A output DC current. The rated running speed of the DC generator is 1800 rpm thus the pitch diameter of the pulley on the motor shaft is two times of the pulley installed on the generator shaft. Four power resistors are connected in serial to load the DC generator. The resistance of the resistors used for load is 100 Ω , 150 Ω and 200 Ω, which corresponds to approximately 333 W, 209 W, and 154 W respectively. Under these load conditions, the motor running speed will change to approximately 887.8 rpm, 889.8 rpm, and 891.6 rpm with the slip of 0.0136, 0.0113, and 0.0093 (equation 2.2) respectively corresponding to 333 W, 209 W, and 154 W.

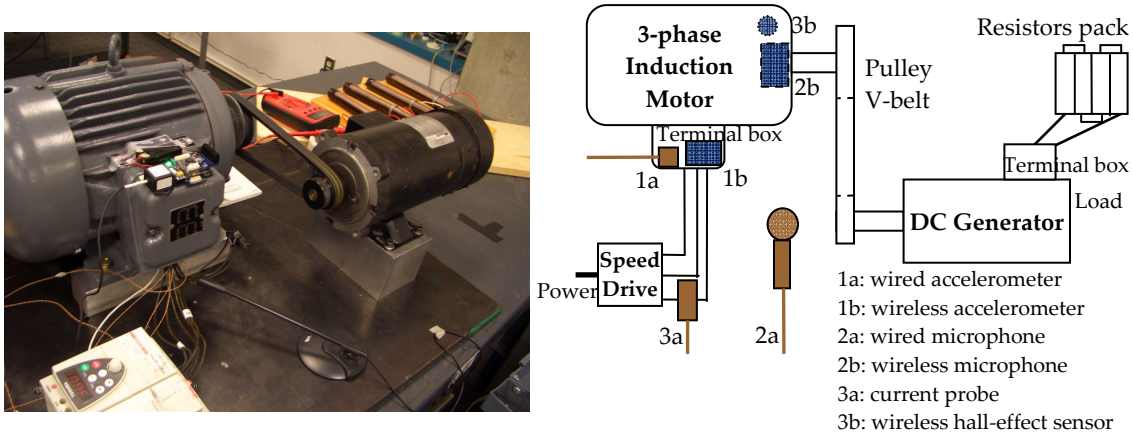

Fig. 5.6 Experiment setup : photo and block diagram

As shown in the diagram (Figure 5.6), three pairs of wired and wireless sensors are installed in this setup. The wired accelerometer is commercially available from Crossbow Tech, Inc. The output is a voltage and the sensitivity is 0.506V/g, where g, the earth's gravitational acceleration, is approximately 9.8 m/s^2. The sampling rate of the wired accelerometer using the company's hardware and software is 160 Hz. The wireless accelerometer is programmed with the sampling rate of 250 Hz. The battery case is separated from the sensor node as shown in Figure 5.7(a). A double sided tape is used to install the flat sensor node on the terminal box. The wired accelerometer is installed beside the wireless one using also the double sided tape.

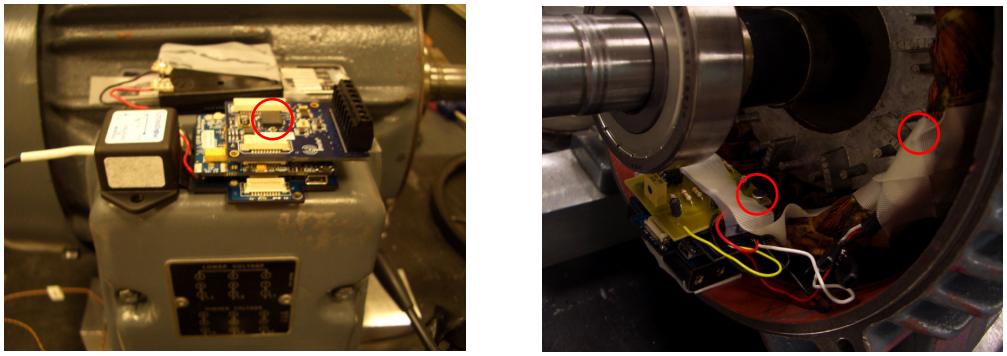

(a) wireless accelerometer (b) wireless microphone and hall-effect sensor

Fig. 5.7 Wireless sensor installation photo (a) accelerometer (b) microphone and hall-effect sensor

Table 5.1 lists the sampling rate of all wired and wireless sensors. The wired microphone is connected to the audio input on the computer. Sound

recording software is used to collect the data. The sampling rate is set to 44.1 kHz. The resulting signal is then down sampled to 8192 Hz. The wireless microphone shown in the left circle in Figure 5.7(b) is connected to the wireless sensor node installed inside the motor frame. The sampling rate is set to 5186 Hz.

Table 5.1 Sampling rate of wired and wireless sensors

sensor type		sampling rate (Hz)
vibration sensor	wired accelerometer	160
	wireless accelerometer	250
current/flux sensor	wired current probe	8192
	wireless hall-effect sensor	5186
acoustic sensor	wired microphone	8192
	wireless microphone	5186

The current probe is an ac current transformer which gives output of 1mA/A AC. The current signal is collected by the data acquisition board from National Instruments Corporation using Labview software. The sampling rate for the current probe is set at 8.192 kHz. The wireless hall-effect sensor is attached to the stator winding shown in the right circle in Figure 5.7(b). It is covered by the high temperature resistance tape. The sampling rate is set to 5186 Hz.

(b) Experimental Design

The same set of experiments is conducted as described in chapter 3. The experiments for initial training and testing are conducted under thirteen different conditions. These conditions are grouped as five categories as shown in Figure 3.2 : 1) two-fault condition; 2) unbalanced stator winding resistance; 3) air-gap eccentricity; 4) damaged bearings; 5) normal condition. Except the normal condition, each category contains three sub-classes. The two-fault conditions studied are a) damaged bearing with unbalanced stator winding resistance; b) damaged bearing with air-gap eccentricity; c) unbalanced stator winding resistance with air-gap eccentricity. Category 2), 3) and 4) are single fault conditions. Three phases of stator winding with bigger resistance (approximately 10% larger than the original resistance) are studied as sub-classes. The three sub-conditions of air-gap eccentricity are a) one-side tilted type; b) two-side parallel type; c) two-side reversed type (see Figure 3.4). The damaged bearing conditions are inner race scratched, outer race scratched and no grease condition.

Any two-fault condition involves unbalanced stator winding resistance fault uses an additional resistor for stator phase A winding. Any two-fault condition involves air-gap eccentricity fault uses the one-side tilted type. The

damaged bearing in two-fault condition a) uses an inner race scratched bearing. The damaged bearing in two-fault condition b) uses an outer race scratched bearing.

For each condition, the motor is set up three times randomly switched from one condition to another with the load resistance of 100 Ω, 150 Ω, and 200 Ω. All the data are collected in 2 seconds time spans and send to the base station periodically. The flux and sound signals are cut to 1 second time span. The sensor data sets are summarized in Table 5.1. The vibration data are collected at a sampling rate of 250 Hz. The flux and sound data are collected at a sampling rate of 5.186 kHz. The flux and sound data frame are set for 1 second durations whereas the accelerometer data is gathered for 2 second durations. For each sensor, 60 sets of data are obtained for each condition except for the normal condition. In order to fit in the 5-category classifier, 180 sets of data are obtained for normal condition. Thus each category has equal number of data sets.

Table 5.2 Data sets summary (wireless sensor)

Sensor type	Sampling rate (Hz)	Frame length (second)	No. of frames
Accelerometer	250	2	60
Flux sensor	5186	1	60
Microphone	5186	1	60

For validation purposes, additional experiments are conducted under two conditions randomly selected from these thirteen conditions. One is a two-fault condition of damaged bearing and air-gap eccentricity. The other is an unbalance stator winding resistance of phase C condition. Different setup will be described in the results section.

5.3.3 Data Analysis

Based on the results of wired sensor experiments, the same signal processing and feature extraction procedures are used here. Due to different load conditions, the HHT features for vibration signals and the FFT features for flux (corresponding to current) and sound signals are slightly different. Vibration data includes an inner race characteristic frequency component (equation 2.8) in IMF1. A pair of stator winding fault characteristic frequency components (equation 2.4, $k = 1, n = 1$) is added to the flux and sound feature lists. The calculation of HHT features is described in chapter 3.1. The HHT and FFT features used here are listed in table 5.2. Half of the data sets are randomly picked from the data sets of each condition as training data. The training data sets are used twice, one for the 5-category classifier, and again for one of the subclass classifiers. The performance is evaluated based on 10 cross validation tests.

Table 5.3 Features list for wireless sensor system

Sensor type	Processing	Feature components
vibration	HHT	f_r (IMF2) , $2f_r$ (IMF1) , $3f_r$ (IMF1) , f_{bs} (IMF1) , f_o (IMF1) , f_i (IMF1) , IMF1 average envelope **Total: 7 features**
flux	FFT	PSH , f_{st} pair, f_1 , f_s+3f_r , f_s+6f_r , f_s+7f_r , f_s+f_i , f_s-f_i , f_s+f_o , f_s-f_o **Total: 11 features**
sound	FFT	PSH , f_{st} pair , f_s+14f_r , f_s+13f_r , f_s+12f_r , f_s+10f_r , f_s+2f_r , f_s+3f_r , f_s+4f_r , f_s+5f_r , f_s+6f_r , f_s+7f_r , f_s+f_o , f_s-f_o , f_s+f_i , f_s-f_i , f_s , f_i , f_o , f_r **Total: 21 features**

5.4 Results

Table 5.4 lists the frequency components calculated from the parameters of the motor and load conditions. The Principal Slot Harmonic (PSH) can be calculated from equation 2.5. Since the rotor of the induction motor in this set of experiments has 48 bars, the PSH frequency is approximately 710.2 Hz, 711.9 Hz, and 713.3 Hz, corresponding to the load conditions of 333 W, 209 W and 154 W. The pulley bearing is SKF bearing of series 6306, a deep grove ball bearing. There are 8 balls in the bearing. The contact angle is 0°. The ball diameter is 12.304mm and the pitch diameter is 51.994mm. The inner/outer race fault characteristic frequencies are 73.19Hz, 73.36 Hz, 73.51 Hz (equation 2.7) and 45.18 Hz, 45.28 Hz, 45.37 Hz (equation 2.8) respectively, corresponding to the

load conditions of 333 W, 209 W, and 154 W. The ball spin frequency is 29.52 Hz, 29.58 Hz, 29.64 Hz (equation 2.9), corresponding to the load conditions of 333 W, 209 W, and 154 W. The frequency components of stator winding faults are 60 ± 14.80 Hz, 60 ± 14.83 Hz, and 60 ± 14.86 Hz (equation 2.4, $n = 1, k = 1$), corresponding to the load conditions of 333 W, 209 W, and 154 W. These frequency components are used in the feature extraction process and all the features are used in various classifiers. The results are shown below.

Table 5.4 Fault characteristic frequencies of the motor.

	Fault Characteristic Frequency (Hz)			Calculated From Equation
	Load 333 W	Load 209 W	154 W	
Principle Slot Harmonic	710.2	711.9	713.3	2.5
Inner Race Fault Frequency	73.19	73.36	73.51	2.7
Outer Race Fault Frequency	45.18	45.28	45.37	2.8
Ball Pass Frequency	29.52	29.58	29.64	2.9
Stator Winding Fault Frequency	60 ± 14.80	60 ± 14.83	60 ± 14.86	2.4

5.4.1 Empirical Mode Decomposition

Figure 5.8 shows the IMFs and their corresponding spectrum of a typical wireless acceleration signal for normal condition and a two-fault condition: bearing inner race with scratch and one-side tilted type air-gap eccentricity. The

EMD process works like an adaptive filter that decomposes the signal into a set of IMFs with different frequency bands. The normal condition in Figure 5.8(a) captures the ball spin frequency of 29.75 Hz in its first IMF C(1)'s spectrum and the rotating frequency 14.75 Hz in its second IMF C(2)'s spectrum. The two-fault condition captures the inner race fault characteristic frequency 73.5 Hz which is absent in normal condition C(1)'s spectrum (see the detailed Figure on the right side in Figure 5.8). There is an obvious difference between the magnitude of average envelope (equation 3.7) in both of the first IMF C(1).

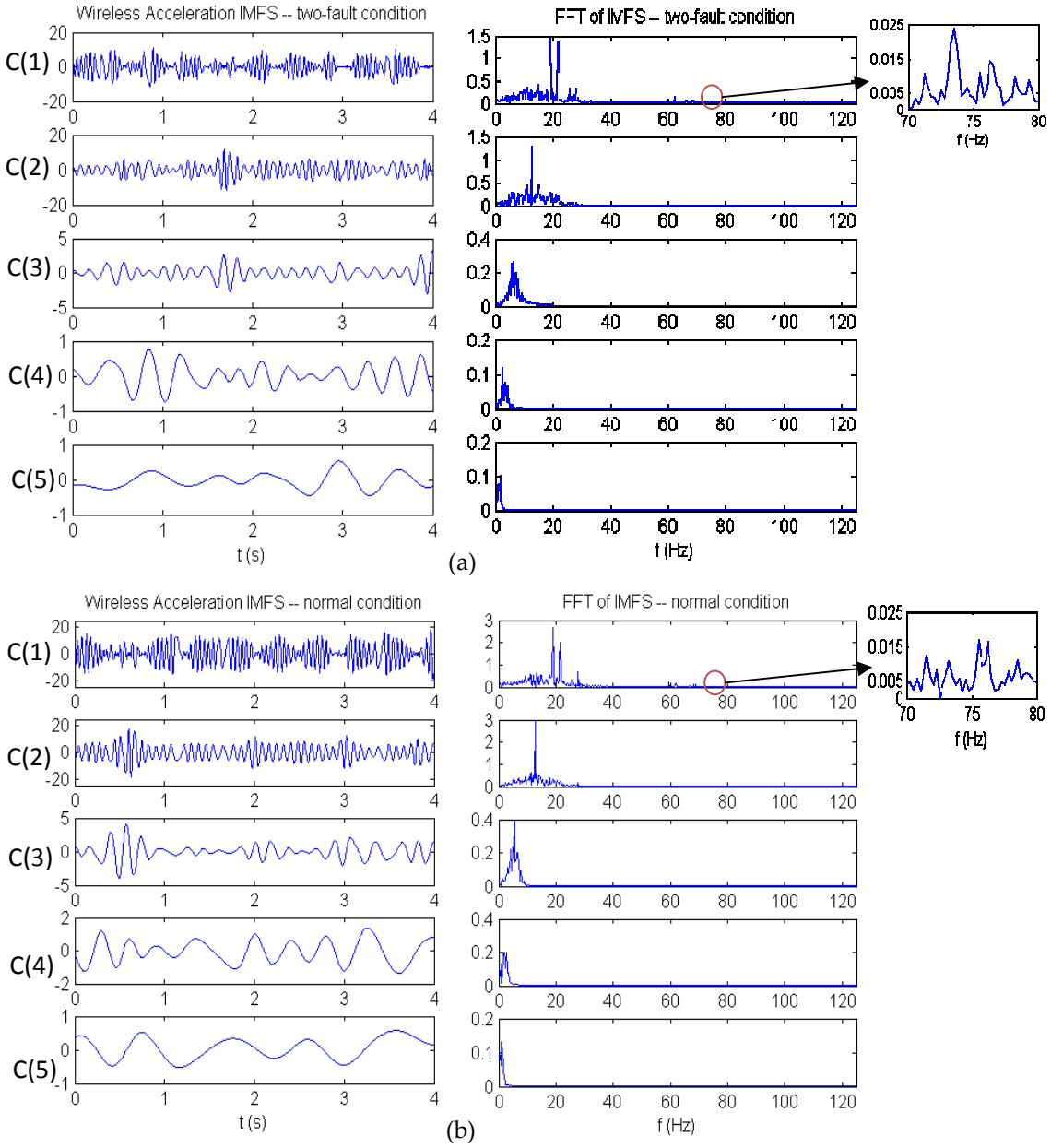

Fig.5.8 IMFs of wireless acceleration and the corresponding spectrum (a) normal condition under load of 154 W (b) two-fault condition: bearing inner race with scratch and one-side tilted type air-gap eccentricity under load of 154 W

5.4.2 Comparison of Wired and Wireless Signals

Figure 5.9 shows the comparison of wired and wireless acceleration data. The original waveform of wired and wireless data looks similar. The maximum values of the acceleration are different due to different resolution and accuracy. The spectra of wireless and wired acceleration signals show the same frequency components in the lower frequency band. Wireless acceleration signal has lower frequency response in the higher frequency band compared to the wired acceleration spectrum.

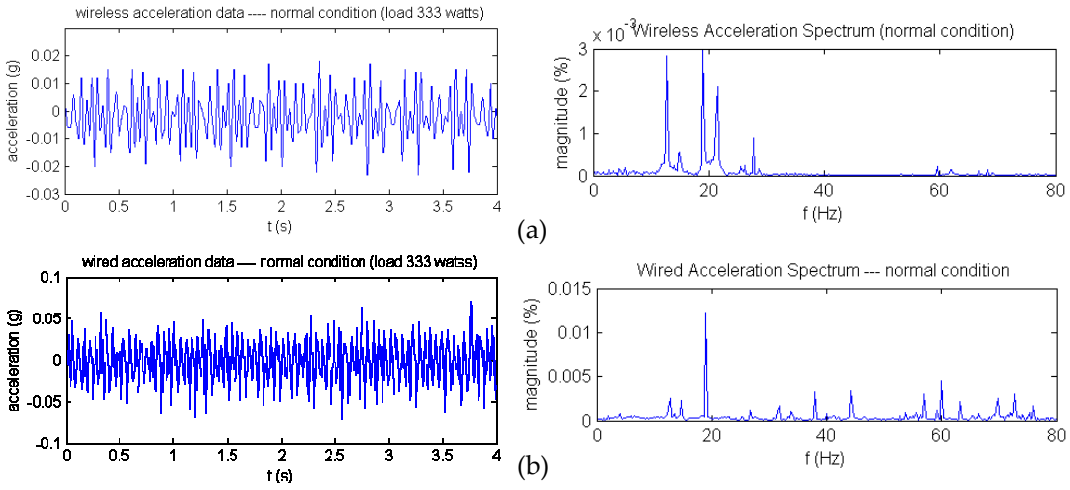

Fig. 5.9 Vibration signals and spectra (a) wireless acceleration and its spectrum (b) wired acceleration and its spectrum (load condition: 333 W)

Figure 5.10 shows the hall-effect sensor data and the current probe data and their spectra. The original waveform of the current probe looks noisiy due to the effect of pulse width modulation controlled by the speed drive. The flux

sensor looks like a sinusoidal wave with the primary frequency of power supply frequency. Both of the spectra show the primary frequency peak at the power supply frequency.

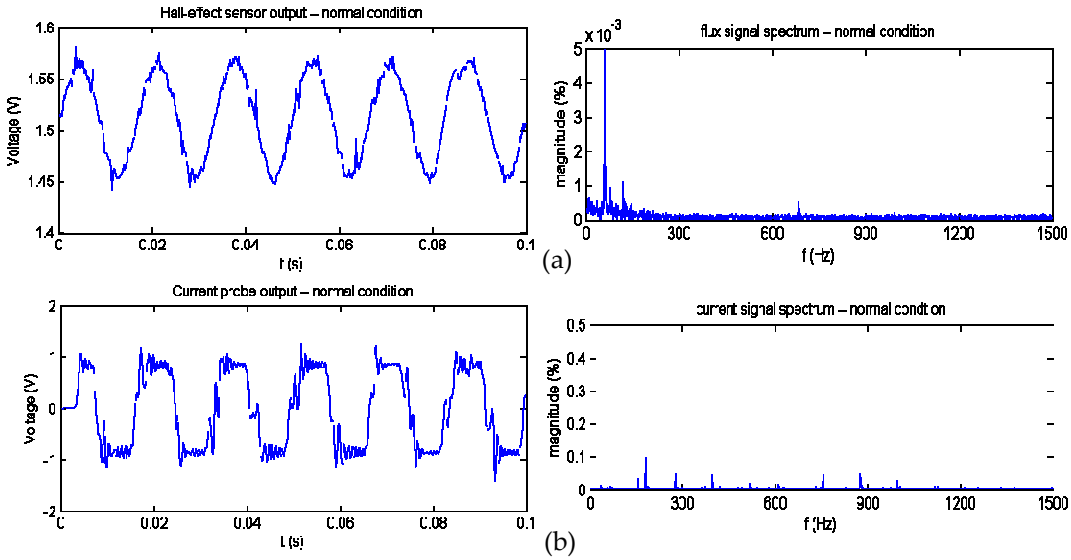

Fig. 5.10 Flux and current signals and their spectra (a) wireless flux data and its spectrum (b) wired current signal and its spectrum (load condition: 333 W)

Figure 5.11 shows the sound data collected from the wired and the wireless microphones. The sound data collected from the wired microphone shows a wider frequency response range. The wireless sound waveform has less high frequency noise. Both of the spectra show the primary frequency peak at the power supply frequency.

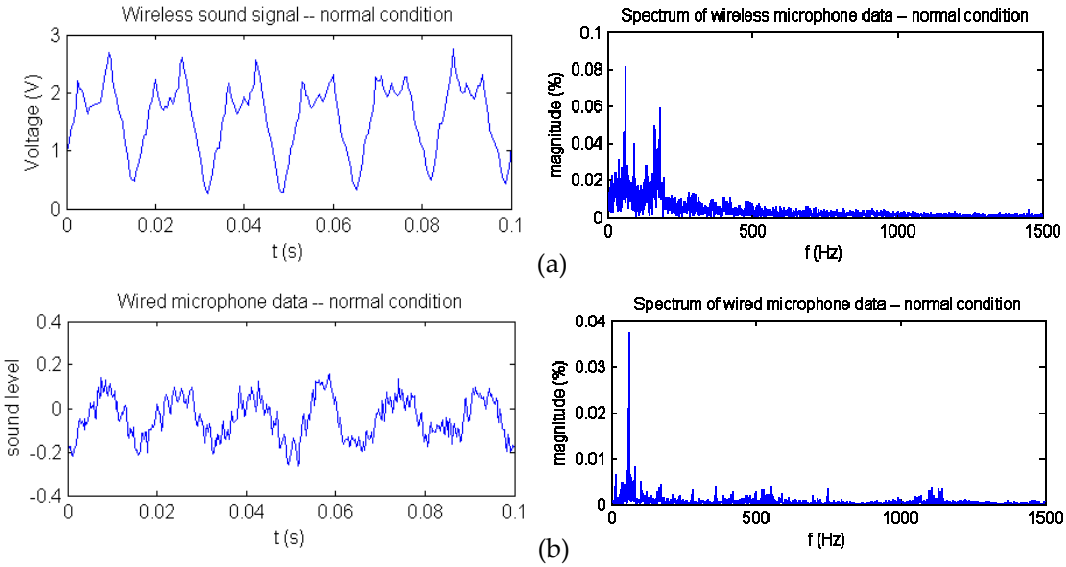

Fig. 5.11 Sound signals and spectra (a) wireless sound data and its spectrum (b) wired sound signal and its spectrum (load condition: 333 W)

5.4.3 Classification Results

Table 5.3 shows the 5-category classifier results using all the features listed in Table 5.2. All three classifiers achieve the correct classification rate above 90%. The highest performance is 97.6% correct classification rate using the ANN classifier. The performance is an average of 10 cross validation testing results since the training data sets are randomly selected from each condition of the initial training and testing data sets. Figure 5.12 shows one simulation test results of the 1st stage 5-category classification in a confusion matrix using the ANN classifier.

Table 5.5 5-category classification results

Classifier	NB	KNN	ANN
Correct Classification Rate (%)	91.7	94.4	**97.6**

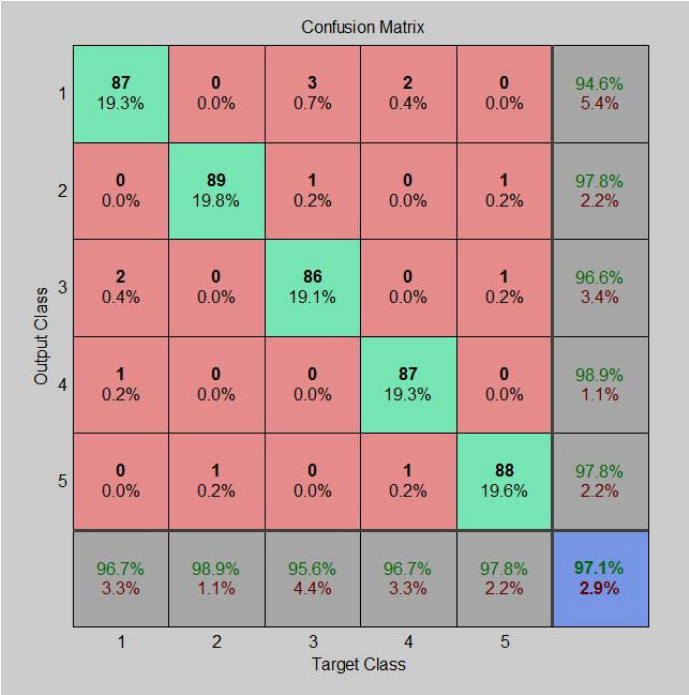

Fig. 5.12 Confusion matrix of ANN 5-category classification results

This confusion matrix contains information about targeted and predicted classifications done by the ANN classifier. Each class has 90 testing trials. Class 1 to 5 represents two-fault condition, unbalanced stator winding resistance, air-gap eccentricity, damaged bearings and normal condition respectively. To read it vertically, for example, there are 87 trials are correctly classified as class 1, 2 trials of class 1 are wrongly classified as class 3 and one trial of class 1 is wrongly classified as class 4. To read it horizontally, 3 trials of class 3 are wrongly

classified as class 1. 2 trials of class 4 are wrongly classified as class 1. The last row shows the correct classification rate of each category in the 1st stage. The total of 450 testing trials in the 1st stage classification has the final performance of 97.1% correct classification rate.

In the 2nd stage, all the training trials are used again in the subclass classifier. Only the correct classified testing trials are evaluated in the subclass classifiers because it has no chance to be correctly classified if the category of this testing trial has already be mislabeled. Table 5.4 lists the results of the test finished for both the 1st and 2nd stage classification. The classifiers used in the 2nd stage subclass classifications are NB classifiers. Most of the 2nd stage classification performance of this test has 100% correct classification rate. The final performance is about the same as the 1st stage performance.

Table 5.6. Final performance of all conditions using wireless sensors

	two-fault condition			unbalanced stator winding resistance			air-gap eccentricity			damaged bearing			normal
1st stage CRC	96.7			98.9			95.6			96.7			97.8
2nd stage CRC	96.7	100	100	100	100	100	93.3	100	100	100	96.7	100	
final perfor-mance	93.5	96.7	96.7	98.9	98.9	98.9	89.2	95.6	95.6	96.7	93.5	96.7	97.8

*CRC: Correct Classification Rate

5.4.4 Validation Tests

In the wireless sensor system, the experiments are conducted in the noisy environment of DC generator and the fan cooler for the power resistors due to the load setup. Thus the validation tests are conducted in (1) quiet lab environment; (2) load music playing environment. No additional machine noise is included. Two conditions, which were not used for training, are randomly chosen from the various possible conditions and two sets of data are collected for each condition to validate the classification system.

The experiments conducted for validation are (a) unbalanced resistance in phase C, (b) damaged bearing and unbalanced stator winding resistance. In the experiments for training and testing above, the resistance of phase C winding is 10% larger than the original resistance but in validation test condition (a) the resistance of phase C winding is 8% larger than the original resistance; The resistance of phase A winding is 10% larger than the original resistance in the two-fault condition of damaged bearing and unbalanced stator winding resistance but in validation test condition (b) the phase C winding is 10% larger than the original resistance instead of the phase A. The data are collected using the same wireless sensor nodes and base station for each set. All the data are

used as testing samples, no training involved. 20 frames are gathered to perform the testing using the classifier trained above.

The validation test results are shown in table 5.5. The first stage classifier is ANN classifier and the second stage is still NB classifier. Table 5.5 lists the testing results in lab quiet environment and load music playing environment. Only 1 trial is failed to be correctly classified in the first stage for both conditions in lab quiet environment. The total performance is 95% correct classification rate. The performance of the first stage classification in music playing environment is reduced by more than 10%. The second stage classification of unbalanced resistance condition is perfect probably because the significant features are not the sound features. The final performances of all validation tests are above 70% correct classification rate.

Table 5.7 Validation test performance (wireless sensor system)

Condition	**unbalanced stator winding resistance**		**damaged bearing and unbalanced stator winding resistance**	
Environment	**Lab quiet**	**Music**	**Lab quiet**	**Music**
First stage classification	**95%(19/20)**	**90.0%(18/20)**	**95%(19/20)**	**80%(16/20)**
Second stage classification	**100%(19/19)**	**100%(18/18)**	**94.7%(18/19)**	**93.8%(14/16)**
Final testing performance	**95%**	**90.0%**	**90.0%**	**70%**

5.5 Summary

This chapter described a wireless motor health monitoring and fault classification system. A two stage hierarchical classification system is designed for the fault diagnosis. The first stage contains five categories and the second stage contains 3 subclasses for each faulty category. Based on the results of wired sensor experiments, the HHT features of vibration sensor and the FFT features of flux and sound sensors are used for classification.

The same set of experiments is conducted for initial training and testing as the wireless experimental studies. Three branches of single fault conditions are studied 1) unbalanced stator winding resistance 2) air-gap eccentricity 3) damaged bearing. Three two-fault conditions are studied 1) damaged bearing and unbalanced winding resistance 2) damaged bearing and air-gap eccentricity 3) air-gap eccentricity and unbalanced winding resistance. Two validation conditions using separate experiment data prove the effectiveness of the system even in a noisy environment.

CHAPTER 6

CONCLUSIONS AND FUTURE DIRECTIONS

This chapter presents conclusions and possible future directions in developing wireless condition monitoring systems.

6.1 Summary and Conclusions

In this dissertation, a complete methodology of applying wireless sensor networks technology into health monitoring and fault classification of induction motors is proposed.

Chapter 1 has introduced the background information of condition monitoring, condition monitoring for motors and the sensor technology for induction machines.

Chapter 2 has introduced the basic construction of an induction motor and the principle of its operation. Previous studies of different motor failures and their diagnosis are briefly reviewed in with emphasis on the fault characteristic frequencies in current, vibration, sound and flux waveforms. These fault characteristic frequencies are of great concern to be used as features for fault detection and classification.

To facilitate the development of wireless sensor systems, a wired monitoring system is designed and implemented for feature selection purposes. Chapter 3 introduced the signal processing procedures and feature selection based on the experimental results of wired sensor system using multiple wired sensors. The experiments are conducted under no-fault, single fault and multiple faults condition. The results demonstrate the effectiveness of using intrinsic mode functions in Hilbert-Huang transform to construct vibration sensor features for classification. However, no single sensor was able to achieve a high enough classification accuracy. Multiple sensors were required to enable reliable classification.

Due to the large number of classes, a two stage classification system is designed to solve the problem. Both HHT features of vibration sensor and FFT features of current and microphone sensors are selected as final features for classification. The first stage contains five categories and the second stage contains 3 subclasses for each faulty category. High classification accuracy is achieved by using multiple sensors and both HHT and FFT features. Two validation conditions using separate experiment data prove the effectiveness of the system even in a noisy environment. These features thus will be used in the study of fault diagnosis using wireless sensors.

In order to identify the reliability of wireless sensors for induction motor monitoring, chapter 4 addresses a feasibility study of wireless sensors in small and large induction motors. Experimental studies on the packet delivery performance and data fidelity of wireless sensors used inside a 1 hp AC motor as well as a 200hp AC motor are presented. Vibration data from the wireless sensor shows a promising accuracy of frequency spectrum comparable to the more reliable wired sensors.

Wireless sensor monitoring system is then constructed based on the experimental results of the wired sensor system. Chapter 5 describes a low-cost wireless sensor network designed for motor health monitoring and fault classification. The wireless sensor nodes with an accelerometer sensor, a microphone, and a hall-effect sensor are developed and implemented in the wireless health monitoring system for induction motors. The same set of experiments is conducted for initial training and testing. The validation results demonstrate the effectiveness and generalizability of the wireless system for motor health monitoring and fault classification.

6.2 Future Directions

This system can be easily extended by including additional category or sub-classes. In this study, only three combinations of two-fault conditions are

trained in the system. More combinations can be studied and the three-fault condition can be included as an additional category in the future. The limitation of this system is the requirement of numerous experiments for each fault type. Furthermore, the experiments were conducted in discrete steps. For example, three discrete types of air-gap eccentricity are simulated and validated. Motor faults usually occur gradually and thus, further experiments that can simulate continuous development of faults such as air-gap eccentricity are needed to verify the generalizability of the algorithms to intermediate stages of fault development. This system is based on the experimental results of one induction motor. It is in an initial stage of research. More motors should be tested which can make the system more generalizable.

The wireless sensor system only minimally exploits the local processing and storage capabilities of the wireless sensor nodes. More sophisticated signal and data processing algorithms can be employed on the sensor nodes. In addition, local communication networks can be set up within the motor to enable collaboration among the sensor nodes. Collaboration can also be set up between several motors in a large facility. Multi-hop mesh networking protocol may be needed to achieve more sophisticated sensor fusion algorithms.

REFERENCES

[1] R. Kothamasu and S. H. Huang, "Adaptive Mamdani fuzzy model for condition-based maintenance," *Fuzzy Sets and Systems,* vol. 158, pp. 2715-2733, 2007.

[2] G. Abdulnour, R. A. Dudek, and M. L. Smith, "Effect of maintenance policies on the just-in-time production system," in *International Journal of Production Research*. vol. 33: Taylor & Francis Ltd, 1995, p. 565.

[3] R. Kothamasu, S. H. Huang, and W. H. VerDuin, "System health monitoring and prognostics: a review of current paradigms and practices," in *International Journal of Advanced Manufacturing Technology*. vol. 28: Springer Science & Business Media B.V., 2006, pp. 1012-1024.

[4] E. M&DC, "Condition-Directed Maintenance," in *Compressed Air Magazine*, 1990, pp. 34-39.

[5] P. Tavner, L. Ran, J. Penman, and H. Sedding, *Condition Monitoring of Rotating Electrical Machines*: Institution of Engineering & Technology (IET), 2008.

[6] B. Rao, *Handbook of condition monitoring*: Elsevier Science, 1996.

[7] L. Bin, T. G. Habetler, and R. G. Harley, "A survey of efficiency-estimation methods for in-service induction motors," *Industry Applications, IEEE Transactions on,* vol. 42, p. 924, 2006.

[8] "SKF condition monitoring technology averts plant failure at major UK paper mill," SKF, U.K., 2009.

[9] S. Leske and D. Kitaljevich, "Managing Gearbox failures, Condition Monitoring and Measurement," in *DEWEK wind energy conference*, Bremen, Germany, 2006.

[10] J. R. Rasmussen, R. F. Bauer, D. Lemieux, C. Schram, and U. Ahmann, "Wind Turbine/Generator Divetrain Condition based monitoring," in *EWEA*, London, U.K., 2004.

[11] M. Morjaria, V. Jammu, and J. Hemmelmann, "Effective Operations and Maintenance of Wind Turbines Through Use of Advance Services Technologies," in *EWEA,*, Brussels, Belgium, 2006.

[12] K. Worden and J. Dulieu-Barton, "An overview of intelligent fault detection in systems and structures," *Structural Health Monitoring*, vol. 3, p. 85, 2004.

[13] W. Frawley, G. Piatetsky-Shapiro, and C. Matheus, "Knowledge discovery in databases: An overview," in *AI Magazine*. vol. 13, 1992, pp. 57-70.

[14] B. Lu, L. Wu, T. G. Habetler, R. G. Harley, and J. A. Gutierrez, "On the application of wireless sensor networks in condition monitoring and energy usage evaluation for electric machines," in *Industrial Electronics Society, 2005. IECON 2005. 31st Annual Conference of IEEE*, 2005, p. 6 pp.

[15] A. Tiwari, P. Ballal, and F. L. Lewis, "Energy-efficient wireless sensor network design and implementation for condition-based maintenance," *ACM Trans. Sen. Netw.*, vol. 3, p. 1, 2007.

[16] J. Webster, *The measurement, instrumentation and sensors handbook*: Springer, 1999.

[17] R. Valentine, *Motor control electronics handbook*: McGraw-Hill Professional, 1998.

[18] J. Irwin, *The industrial electronics handbook*: CRC Press, 1997.

[19] Z. Wei, T. G. Habetler, and R. G. Harley, "Bearing Condition Monitoring Methods for Electric Machines: A General Review," in *Diagnostics for Electric Machines, Power Electronics and Drives, 2007. SDEMPED 2007. IEEE International Symposium on*, 2007, p. 3.

[20] W. D. Li and C. K. Mechefske, "Detection of induction motor faults: A comparison of stator current, vibration and acoustic methods," *Journal Of Vibration And Control,* vol. 12, pp. 165-188, Feb 2006.

[21] B. Beihoff, "A survey of torque transduction methodologies for industrial applications," in *Pulp and Paper Industry Technical Conference, 1996., Conference Record of 1996 Annual*, 1996, pp. 220-229.

[22] G. Gao, M. Steinhauser, R. Kavanaugh, and W. Chen, "Using fiber-optic sensors to measure strain in motor stator end windings during operation," in *Electrical Insulation Conference and Electrical Manufacturing & Coil Winding Conference, 1999. Proceedings*, 1999, pp. 645-648.

[23] R. Popovic, "Hall-effect devices," *Sens. Actuators,* vol. 17, pp. 39-53, 1989.

[24] T. J. Harvey, R. J. K. Wood, and H. E. G. Powrie, "Electrostatic wear monitoring of rolling element bearings," *Wear,* vol. 263, pp. 1492-1501, 2007.

[25] A. Fitzgerald, C. Kingsley, and S. Umans, *Electric machinery*: McGraw-Hill Science Engineering, 2002.

[26] X. Xue, V. Sundararajan, and L. Gonzalez-Argueta, "Sensor fusion for machine condition monitoring," in *Sensors and Smart Structures Technologies for Civil, Mechanical, and Aerospace Systems 2008*, San Diego, California, USA, 2008, pp. 69321D-9.

[27] M. Haji and H. A. Toliyat, "Pattern recognition-a technique for induction machines rotor broken bar detection," *Energy Conversion, IEEE Transaction on*, vol. 16, p. 312, 2001.

[28] G. B. Kliman, R. A. Koegl, J. Stein, R. D. A. E. R. D. Endicott, and M. W. A. M. M. W. Madden, "Noninvasive detection of broken rotor bars in operating induction motors," *Energy Conversion, IEEE Transaction on,* vol. 3, p. 873, 1988.

[29] S. Nandi and H. A. Toliyat, "Condition monitoring and fault diagnosis of electrical machines-a review," in *Industry Applications Conference, 1999. Thirty-Fourth IAS Annual Meeting. Conference Record of the 1999 IEEE*, 1999, p. 197.

[30] A. H. Bonnett and G. C. Soukup, "Analysis of rotor failures in squirrel-cage induction motors," *Industry Applications, IEEE Transactions on,* vol. 24, pp. 1124-1130, 1988.

[31] W. T. Thomson and M. Fenger, "Current signature analysis to detect induction motor faults," *Industry Applications Magazine, IEEE,* vol. 7, p. 26, 2001.

[32] W. T. Thomson and I. D. Stewart, "On-line current monitoring for fault diagnosis in inverter fed induction motors," in *IEE Third International Conference on Power Electronics and Drives,* London, 1988, pp. 432-435.

[33] F. Filippetti, G. Franceschini, C. Tassoni, and P. Vas, "AI techniques in induction machines diagnosis including the speed ripple effect," in *Industry Applications Conference, 1996. Thirty-First IAS Annual Meeting, IAS '96., Conference Record of the 1996 IEEE*, 1996, pp. 655-662 vol.1.

[34] N. M. Elkasabgy, A. R. Eastham, and G. E. Dawson, "Detection of broken bars in the cage rotor on an induction machine," *Industry Applications, IEEE Transactions on,* vol. 28, pp. 165-171, 1992.

[35] A. H. Bonnett and G. C. Soukup, "Cause and analysis of stator and rotor failures in three-phase squirrel-cage induction motors," *Industry Applications, IEEE Transactions on,* vol. 28, pp. 921-937, 1992.

[36] J. Faiz, B. Ebrahimi, and M. Sharifian, "Different Faults and Their Diagnosis Techniques in Three-Phase Squirrel-Cage Induction Motors - A Review," *Electromagnetics,* vol. 26, pp. 543-569, 2006.

[37] A. Siddique, G. S. Yadava, and B. Singh, "A Review of Stator Fault Monitoring Techniques of Induction Motors," *IEEE Transactions on Energy Conversion,* vol. 20, pp. 106-114, 2005.

[38] G. Stone, E. Boulter, I. Culbert, and H. Dhirani, *Electrical insulation for rotating machines: design, evaluation, aging, testing, and repair*: Wiley-IEEE Press, 2004.

[39] S. Fruchtenicht, E. Pittius, and H. O. Seinsch, "A diagnostic system for three-phase asynchronous machines," in *Electrical Machines and Drives*, IEE Savoy Place, London, 1989, pp. 163-171.

[40] J. Penman, H. G. Sedding, B. A. Lloyd, and W. T. Fink, "Detection and location of interturn short circuits in the stator windings of operating motors," *Energy Conversion, IEEE Transactions on,* vol. 9, pp. 652-658, 1994.

[41] W. T. Thomson, "On-line MCSA to diagnose shorted turns in low voltage stator windings of 3-phase induction motors prior to failure," in *Electric Machines and Drives Conference, 2001. IEMDC 2001. IEEE International*, 2001, pp. 891-898.

[42] T. Kikuchi and T. Kenjo, "In-depth learning of cogging/detenting torque through experiments and simulations," *Education, IEEE Transactions on,* vol. 41, pp. 352-352, 1998.

[43] W. T. Thomson, D. Rankin, and D. G. Dorrell, "On-line current monitoring to diagnose airgap eccentricity-an industrial case history of a large high-voltage three-phase induction motor," in *Electric Machines and Drives Conference Record, 1997. IEEE International*, 1997, p. MA2/4.1.

[44] S. Nandi, R. M. Bharadwaj, and H. A. Toliyat, "Performance analysis of a three-phase induction motor under mixed eccentricity condition," *Energy Conversion, IEEE Transaction on,* vol. 17, p. 392, 2002.

[45] S. Nandi, S. Ahmed, and H. A. Toliyat, "Detection of rotor slot and other eccentricity related harmonics in a three phase induction motor with different rotor cages," *Energy Conversion, IEEE Transactions on,* vol. 16, pp. 253-260, 2001.

[46] H. A. Toliyat and N. A. Al-Nuaim, "Simulation and detection of dynamic air-gap eccentricity in salient-pole synchronous machines," *Industry Applications, IEEE Transactions on,* vol. 35, p. 86, 1999.

[47] Austin Bonnett and C. Young, "Explaining motor failure," in *EC&M*, 2004, pp. 22-24.

[48] N. Tandon and A. Choudhury, "A review of vibration and acoustic measurement methods for the detection of defects in rolling element bearings," *Tribology International,* vol. 32, p. 469, 1999.

[49] "Reliability case studies," Noria Corporation, USA, 2005.

[50] G. Wang, Z. Luo, X. Qin, Y. Leng, and T. Wang, "Fault identification and classification of rolling element bearing based on time-varying autoregressive spectrum," *Mechanical Systems and Signal Processing,* vol. 22, p. 934, 2008.

[51] Z. Jia-Fan and H. Zhi-Chu, "Kernel Fisher discriminant analysis for bearing fault diagnosis," in *Machine Learning and Cybernetics, 2005. Proceedings of 2005 International Conference on*, 2005, p. 3216.

[52] B. Samanta, K. R. Al-Balushi, and S. A. Al-Araimi, "Artificial neural networks and support vector machines with genetic algorithm for bearing fault detection," *Engineering Applications of Artificial Intelligence,* vol. 16, p. 657, 2003.

[53] R. R. Schoen, T. G. Habetler, F. Kamran, and R. G. A. B. R. G. Bartfield, "Motor bearing damage detection using stator current monitoring," *Industry Applications, IEEE Transactions on,* vol. 31, p. 1274, 1995.

[54] Z. K. Peng, P. W. Tse, and F. L. Chu, "A comparison study of improved Hilbert-Huang transform and wavelet transform: Application to fault diagnosis for rolling bearing," *Mechanical Systems and Signal Processing,* vol. 19, pp. 974-988, 2005.

[55] W. G. Zanardelli, E. G. Strangas, and S. Aviyente, "Identification of Intermittent Electrical and Mechanical Faults in Permanent-Magnet AC Drives Based on Time-Frequency Analysis," *Industry Applications, IEEE Transactions on,* vol. 43, p. 971, 2007.

[56] W. G. Zanardelli, E. G. Strangas, H. K. Khalil, and J. M. Miller, "Wavelet-based methods for the prognosis of mechanical and electrical failures in electric motors," *Mechanical Systems and Signal Processing,* vol. 19, p. 411, 2005.

[57] V. K. Rai and A. R. Mohanty, "Bearing fault diagnosis using FFT of intrinsic mode functions in Hilbert-Huang transform," *Mechanical Systems and Signal Processing,* vol. 21, pp. 2607-2615, 2007.

[58] B. Liu, S. Riemenschneider, and Y. Xu, "Gearbox fault diagnosis using empirical mode decomposition and Hilbert spectrum," *Mechanical Systems and Signal Processing,* vol. 20, pp. 718-734, 2006.

[59] L. Hui and Z. Haiqi, "Bearing Fault Detection Using Envelope Spectrum Based on EMD and TKEO," in *Fuzzy Systems and Knowledge Discovery, 2008. FSKD '08. Fifth International Conference on*, 2008, pp. 142-146.

[60] N. E. Huang, Z. Shen, S. R. Long, M. L. C. Wu, H. H. Shih, Q. N. Zheng, N. C. Yen, C. C. Tung, and H. H. Liu, "The empirical mode decomposition and the Hilbert spectrum for nonlinear and non-stationary time series analysis," *Proceedings of the Royal Society of London Series a-Mathematical Physical and Engineering Sciences,* vol. 454, pp. 903-995, Mar 1998.

[61] N. Huang, M. Wu, S. Long, S. Shen, W. Qu, P. Gloersen, and K. Fan, "A confidence limit for the empirical mode decomposition and Hilbert spectral analysis," *Royal Society of London Proceedings Series A,* vol. 459, pp. 2317-2345, 2003.

[62] S. Hahn, *Hilbert transforms in signal processing*: Artech House Publishers, 1996.

[63] S. G. Mallat, "A theory for multiresolution signal decomposition: the wavelet representation," *Pattern Analysis and Machine Intelligence, IEEE Transactions on,* vol. 11, pp. 674-693, 1989.

[64] I. Rish, "An empirical study of the naive Bayes classifier," in *IJCAI 2001 Workshop on Empirical Methods in Artificial Intelligence*, 2001.

[65] R. O. Duda, P. E. Hart, and D. G. Stork, *Pattern classification (2nd Edition)*. New York: John Wiley & Sons, Inc., 2001.

[66] J. Zurada, *Introduction to artificial neural systems*: West Publishing Co. St. Paul, MN, USA, 1992.

[67] M. Rashid, *Power Electronics Handbook: Devices, Circuits, And Applications*: Academic Press, 2006.

[68] S. Prabhakar, A. R. Mohanty, and A. S. Sekhar, "Application of discrete wavelet transform for detection of ball bearing race faults," *Tribology International,* vol. 35, pp. 793-800, 2002.

[69] L. Bin, T. G. Habetler, and R. G. Harley, "A survey of efficiency-estimation methods for in-service induction motors," *Industry Applications, IEEE Transactions on,* vol. 42, pp. 924-933, 2006.

[70] J. Zhao and R. Govindan, "Understanding packet delivery performance in dense wireless sensor networks," in *Proceedings of the 1st international conference on Embedded networked sensor systems* Los Angeles, California, USA: ACM, 2003.

[71] M. Kohvakka, M. Hannikainen, and T. D. Hamalainen, "Wireless sensor network implementation for industrial linear position metering," in *Digital System Design, 2005. Proceedings. 8th Euromicro Conference on*, 2005, pp. 267-273.

[72] D. Ganesan, B. Krishnamachari, A. Woo, D. Culler, D. Estrin, and S. Wicker, "Complex behavior at scale: An experimental study of low-power

wireless sensor networks," *CENS, UCLA and IRL, UCB, Tech. Rep,* pp. 02-0013, 2002.

[73] T. Hsin-Mu, W. Viriyasitavat, O. K. Tonguz, C. Saraydar, T. Talty, and A. Macdonald, "Feasibility of In-car Wireless Sensor Networks: A Statistical Evaluation," in *Sensor, Mesh and Ad Hoc Communications and Networks, 2007. SECON '07. 4th Annual IEEE Communications Society Conference on*, 2007, pp. 101-111.

[74] M. Paselli, F. Petre, O. Rousseaux, G. Meynants, M. Engels, L. Benini, and B. Gyselinckx, "A High-Performance Wireless Sensor Node for Industrial Control Applications," in *Systems, 2008. ICONS 08. Third International Conference on*, 2008, pp. 235-240.

[75] M. Rahimi, H. Shah, G. S. Sukhatme, J. Heideman, and D. Estrin, "Studying the feasibility of energy harvesting in a mobile sensor network," in *Robotics and Automation, 2003. Proceedings. ICRA '03. IEEE International Conference on*, 2003, pp. 19-24 vol.1.

[76] K. Jemielniak, "Commercial Tool Condition Monitoring Systems," *The International Journal of Advanced Manufacturing Technology,* vol. 15, pp. 711-721, 1999.

[77] "Intellegize Your Process," ARTIS company presentation, Germany, 2007.

[78] "Process Control During Grinding and Dressing," brochure of NORDMANN Company, Germany, 2004.

[79] "PROMOS for grinding and dressing," brochure of PROMETEC Company, Germany, 2004.

[80] F. Discenzo, D. Chung, and K. Loparo, "Pump Condition Monitoring Using Self-Powered Wireless Sensors," *Sound and Vibration,* vol. 40, pp. 12-15, 2006.

[81] S. Xingfa, W. Zhi, and S. Youxian, "Wireless sensor networks for industrial applications," in *Intelligent Control and Automation, 2004. WCICA 2004. Fifth World Congress on*, 2004, pp. 3636-3640 Vol.4.

[82] A. Bonivento, L. P. Carloni, and A. Sangiovanni-Vincentelli, "Platform-based design of wireless sensor networks for industrial applications," in *Proceedings of the conference on Design, automation and test in Europe: Proceedings* Munich, Germany: European Design and Automation Association, 2006.

[83] X. Xue, L. Gonzalez-Argueta, and V. Sundararajan, "Energy Scavenging For Wireless Sensor Networks," in *Proceedings: 2007 IDETC, ASME/IEEE International Conference on Mechatronics and Embedded Systems and Applicaitons*, Las Vegas, Nevada, USA, 2007.

[84] A. Wood, *Magnetic venture: the story of Oxford Instruments*: Oxford University Press, USA, 2001.

[85] D. Gay, P. Levis, R. v. Behren, M. Welsh, E. Brewer, and D. Culler, "The nesC language: A holistic approach to networked embedded systems," *SIGPLAN Not.*, vol. 38, pp. 1-11, 2003.

[86] J. Polastre, J. Hill, and D. Culler, "Versatile low power media access for wireless sensor networks," in *Proceedings of the 2nd international conference on Embedded networked sensor systems* Baltimore, MD, USA: ACM, 2004.

[87] J. Yick, B. Mukherjee, and D. Ghosal, "Wireless sensor network survey," *Computer Networks*, vol. 52, pp. 2292-2330, 2008.

[88] W. Stallings, "Wireless Communications and Networks," Prentice Hall, 2001.

[89] J. A. Gutierrez, M. Naeve, E. Callaway, M. Bourgeois, V. Mitter, and B. Heile, "IEEE 802.15.4: a developing standard for low-power low-cost wireless personal area networks," *Network, IEEE*, vol. 15, pp. 12-19, 2001.

[90] X. Xin, V. Sundararajan, and W. P. Brithinee, "The application of wireless sensor networks for condition monitoring in three-phase induction motors," in *Electrical Insulation Conference and Electrical Manufacturing Expo, 2007*, 2007, pp. 445-448.

[91] L. Nachman, "Intel Corporation Research Santa Clara. CA. New tinyos platforms panel: iMote2," *The Second International TinyOS Technology Exchange*, 2005.